ISSN:2538-516X

Journal of

Civil Engineering Researchers

Volume: 7; Number: 3; September 2025

J-Researchers

J-Researchers

JOURNAL OF
CIVIL
ENGINEERING
RESEARCHERS

Volume 7, Number 3, September 2025

Contents

J-Researchers

Journal of Civil Engineering Researchers

Journal homepage: www.journals-researchers.com

Simplified Unified Model for Flexural Capacity of Ductile HPC Beams with A Low Reinforcement Ratio

Wisam Hamad,[a] Mehdi Dehestani,[a,*]

[a] Faculty of Civil Engineering, Babol Noshirvani University of Technology, Babol, Postal Box: 484, Postal Code: 47148-71167. Iran

ABSTRACT

There is no specific model to predict the flexural capacity of high-performance concrete (HPC) beams with a low reinforcement ratio. Accordingly, a comprehensive experimental database containing 162 datasets was gathered from literature to propose an explicit analytical model containing various critical features, including fiber volume fraction, fiber aspect ratio, fiber strength, water-to-binder (w/b) ratio of mixture, and reinforcement ratio. Additionally, a supplementary experimental study involving a large-scale ductile HPC beam with a very low reinforcement ratio (almost negligible) was conducted to verify the model's performance. The findings revealed that the proposed bending model achieved an integral of absolute error (IAE) of 10.8% and a coefficient of variation (COV) of 1.04, indicating its high accuracy in comparison to a comprehensive experimental dataset comprising 162 large-scale beam tests. Furthermore, the comparison between the experimental results of the tested beam and the proposed model showed a deviation of 4.5%, which supports the effectiveness of the flexural capacity formulation. A parametric statistical analysis was conducted using Minitab software to evaluate the influence of key parameters affecting the roles of fiber and matrix.

ARTICLE INFO

Received: June 10, 2025
Accepted: August 02, 2025

Keywords:
Beam
HPC
Flexural Capacity
Low Reinforcement Ratio
Fiber Role

DOI: 10.66224/JCER.7.3.1
DOR: 20.1001.1.2538516.2025.7.3.1.1

1. Introduction

How reliable is using a high-performance concrete (HPC) beam containing a high-volume fraction of fibers as an independent RC member using a low reinforcement ratio, almost negligible? Researchers have raised this question since the first day the HPC and UHPC concrete generation was introduced, but it has not been thoroughly investigated due to concerns about the ductility of these beams. Although many experimental works concentrated on this context, there is almost no reliable model to predict the flexural capacity of such economic beams using UHPC and a minimal reinforcement ratio.

Investigations into the flexural characteristics of HPC (high-performance concrete), ultra-high performance concrete (UHPC), and engineered cementitious composites (ECC) beams with low reinforcement ratios have made significant progress over the last decade, uncovering crucial insights into their structural behavior and mechanisms for controlling cracking. In this context, Yang et al. [1] demonstrated that large-scale steel fiber-reinforced UHPC beams (L=2.9m) with reinforcement

* Corresponding author. Tel.: +989113136113; e-mail: dehestani@nit.ac.ir.

ratios ranging from 0 to 0.02 exhibit enhanced ductility, with ductility indices between 1.60 and 3.75, and that the method of placing UHPC influences fiber orientation and flexural performance. They used 2.0% volume fraction straight steel fibers within UHPC mixture with a water-to-binder (w/b) of 0.2 and a compressive strength range of 190.9-193.4 MPa. Meda et al. [2] explored fiber-reinforced concrete beams under flexure and noted that while fibers generally enhance post-cracking stiffness and toughness, in some cases, especially with low strain-hardening steel reinforcement and high toughness fibers, the overall rotation capacity and ductility may be reduced due to strain localization at cracks. They considered L=4.0m large-scale fiber-reinforced concrete beams with reinforcement ratio ranging from 0.0075 to 0.012 and compressive strengths of 43.2-49.7 MPa. They used various volume fractions of hook-ended steel fibers ranging from 0 to 0.76% within concrete with w/b=0.48. Kamal et al. [3] concentrated on ultra-high-strength concrete beams (L=1.0 m) containing various fiber types (polypropylene fibers and steel) with a volume fraction of 0-0.5% within the concrete mixture with w/b=0.3. They found that fibers increase the number of cracks and stiffness, reduce the crack width, and improve the ultimate load, underscoring the superior performance of steel fibers over polypropylene fibers in flexural strength enhancement. They selected a range of 0.012-0.017 for the reinforcement ratio of beams with compressive strength of around 130 MPa. Abbas et al. [4] investigated how the length and amount of steel fibers affect the mechanical properties of UHPC, highlighting that shorter steel fibers enhance flexural performance and that a higher dosage of fibers boosts both strength and resistance to chloride penetration. Accompanying these findings, Yoo et al. [5] combined experimental and numerical analyses of UHPFRC beams (L=3.5 m) with low reinforcement ratios (0 to 0.0171), confirming that increasing reinforcement ratio enhances post-cracking stiffness and load capacity, while crack patterns remain consistent, and emphasizing the importance of tension-softening behavior for accurate structural predictions. They used 2.0% straight steel fibers within concrete with w/b=0.2 and compressive strength of 196.7 MPa. They reported ductility indices ranging from 3.65 to 5.12 for their large-scale beams containing a very low reinforcement ratio. Yoo and Moon [6] assessed the flexural behavior of standard RC beams with L=3.0 m, very low reinforcement ratios of 0.178%–0.406 %, and incorporated hooked-end steel fibers (0.25%–1.0 % by volume). Although the addition of fibers enhanced post-cracking stiffness and cracking performance, it led to a decrease in ductility indices (from 8.3 to 2.2) and did not recover ultimate load losses caused by diminished rebar ratios. The research concluded that steel fibers at or below 1% cannot substitute for longitudinal rebars in providing ductility or strength margins. The study conducted by Cardoso et al. [7] examined the flexural performance of large-scale steel fiber-reinforced RC beams that had low reinforcing ratios, utilizing both experimental and analytical methods, with L=1.20 m and reinforcement ratios of 0.0028-0.007%. The concrete mixtures included hooked-end steel fibers with volume fractions ranging from 0.5% to 2.0%. Their compressive strength of the high-strength concrete matrices varied between 76.3 MPa and 95.2 MPa. Although their results demonstrated that RC beams with high volume fraction displayed notable capacity improvements (21–109%) when compared to plain RC beams, along with narrower crack widths at equivalent rebar stresses, employing fibers resulted in crack localization and diminished ductility, especially in beams with lower reinforcing ratios. Parvin et al. [8] conducted an experimental study on the flexural performance of UHPFRC beams reinforced with reinforcement ratio ranging from 0.64% to 1.45%, alongside a 2.0% volume fraction of hooked-end steel fibers. The UHPFRC attained a compressive strength of 130 MPa. The findings revealed that GFRP-reinforced beams had a greater load capacity (up to a 65% increase at lower reinforcement ratios) compared to their steel-reinforced equivalents, yet the fibers had a limited impact on reducing the brittle failure in GFRP samples. An increase in reinforcement ratios led to a change in failure modes from flexural to shear in GFRP beams, while steel-reinforced beams exhibited a ductile response.

While extensive experimental investigations have focused on large-scale fiber-reinforced concrete beams featuring low reinforcement ratios, there remains a notable absence of specific studies that reliably predict the flexural strength of such beams. To address this gap, the present study aims to compile a thorough database of experimental results encompassing a range of advanced concrete types, including HPC, UHPC, ECC, and various fiber-reinforced beams with a high-volume fraction of fibers. A total of 162 datasets were collected from the literature. In conjunction with this database, a rigorous supplementary experimental program was undertaken to validate the accuracy and reliability of the proposed unified flexural model. Furthermore, a detailed parametric study was incorporated to explore the pivotal role that fibers play in enhancing the bending moment capacity of these beams, effectively compensating for the limitations posed by lower reinforcement ratios. The main research hypothesis and novelty are proposing a new model for the flexural capacity of ductile HPC using separate equations for Msteel, Mfiber, and Mmatrix. Almost no specific study has distinguished the main role of fibers and matrix in the total bending moment capacity of HPC. As fiber and matrix play important roles in the case of a low (almost negligible) reinforcement ratio, their role should be precisely recognized. Accordingly, the main novelty of the present study is to achieve a new reliable model to determine how much percentage of total bending moment that can be tolerated only through using fiber and matrix within HPC to compensate for the role of longitudinal reinforcement.

Table 1.
Details of the experimental database were collected from the literature to achieve the model

Reference	w/b	Powder	Fiber type	V_f (%)	f_c' (MPa)	ρ_s (-)	L (mm)	$b \times h$ (mm)	n
Yang et al. [1]	0.20	SF	straight steel	2.0	~ 194	0-0.0196	2900	180×270	13
Meda et al. [2]	0.48	-	hook-ended steel	0-0.76	~ 46.8	0.0075-0.015	4000	200×300	7
Kamal et al. [3]	0.30	SF	PP and steel	0-0.5	~ 130	0.012-0.017	1000	100×150	6
Yoo and Yoon [10]	0.13-0.14	SF+silica flour	smooth and twisted steel	0-2.0	~212.8	0.0094-0.015	2500	150×220	10
Yoo et al. [5]	0.20	SF	straight steel	2.0	~ 196.7	0-0.0171	2900	200×270	4
Singh et al. [11]	0.14	SF	hook-ended steel	2.25	~ 140	0.0175-0.0231	3500	250×250 150×150	3
Yoo and Moon [6]	0.37	-	hook-ended steel	0-1.0	~43.2	0.0018-0.0041	3000	320×300	40
Hasgul et al. [12]	0.18	SF+ GGBFS	straight micro-steel	0-1.5	~149.8	0.009-0.043	2500	150×250	8
Gümüş and Arslan [13]	0.17	SF	chopped carbon fiber and hooked-end steel	0-0.99	~116.4	0.0017-0.005	1300	150×200	18
Liu et al. [14]	0.32	FA	PVA fiber	0-2.0	~56	0.0128-0.0168	1700	120×200	8
Turker et al. [15]	0.18	SF+ GGBFS	short-straight and long hooked steel	0-1.5	~155.7	0.009-0.043	2500	150×200	12
Cardoso et al. [7]	0.26	SF+FA	hooked-end fibers	0-2	~81.5	0.0028-0.007	1200	150×150	9
Conforti et al. [16]	-	-	hooked-end steel and crimped glass, and embossed polymer	0-1.05	~48	0.005-0.012	900	150×150	14
Chen et al. [17]	0.20	SF+SFP	PP and steel	0-1.0	~136.1	0.0106	1500	150×200	2
Jin et al. [18]	-	-	PP	0-2.0	~29.43	0-0.0165	1100	100×120	5
Parvin et al. [8]	0.15	-	hooked-end steel	2.0	~130	0.0064-0.0145	1650	250×300	3

* w/b= water-to-binder ratio; n=number of database for each reference; V_f=volume fraction (%); ρ_s=reinforcement ratio; L=total length of large-scale beams; SF=silica fume powder; GGBFS=Ground granulated blast-furnace slag powder; FA=fly ash powder; "~" denotes the average compressive strength for each reference; PP=Polypropylene fibers; PVA= Polyvinyl alcohol fibers; "-" denotes unmentioned values in the references.

Table 2.
Details of the input variables for achieving the proposed model

Input	Count	Mean	Std. Dev.	Min	Max
V_f	162	0.89	0.77	0	2.25
f_c'	162	101.54	60.77	29.04	232.1
ρ_s	162	0.0096	0.0088	0	0.043
b	162	196.54	76.43	100	320
h	162	235.35	58.29	120	300
d	162	191.06	68.080	25	260
L	162	2255.66	892.96	900	4000
f_y rebar	162	507.66	41.32	386.3	602.8
fiber strength	162	1359.59	945.05	0	3800

2. Proposed Analytical Model

To develop and validate the proposed flexural strength model, an extensive database comprising 162 large-scale experimental beam specimens was compiled from the literature, which is comprehensively described in Table 1. The database includes RC beams constructed with HPC, UHPC, and ECC, all featuring low or very low longitudinal reinforcement ratios and varying fiber contents. The key parameters extracted and analyzed include fiber properties (volume fraction (V_f), aspect ratio, and strength), concrete compressive strength (f_c'), reinforcement ratio (ρ_s), and beam geometrical and mechanical properties. The V_f Ranged from 0% to 2.25%, with an average of 0.89%, capturing both non-fibered and highly fibered specimens. The concrete compressive strength spanned a wide range, from 29.04 MPa to 232.1 MPa, with a high mean of 101.54 MPa, confirming the inclusion of both HPC and UHPC specimens. The reinforcement ratio varied between 0% and 4.3%, with an average of just 0.96%, reflecting the primary focus of this study on lightly reinforced members. In terms of geometry, beam widths ranged from 100 mm to 320 mm (mean: 196.5 mm), and heights from 120 mm to 300 mm (mean: 235.35 mm), encompassing both moderate and large cross-sections typical of structural-scale elements. This wide variation in mechanical properties, fiber contents, and cross-sectional dimensions ensures that the proposed model is robust, generalizable, and applicable across a broad spectrum of ductile HPC design scenarios, particularly those where minimizing steel reinforcement is desired while maintaining structural performance. The main similar properties of studies mentioned in Table 1 are the high volume fraction of fibers, low and very low (almost negligible) content of longitudinal reinforcement, and high quantity of powders used in concrete compositions. Also, the authors selected only studies containing large-scale beams under a four-point bending test, so that constant and similar boundary and load conditions were considered in the gathered database. Additionally, the experimental beams in the gathered database experienced only flexural failure, meaning that the shear failure was prevented using sufficient shear reinforcement (stirrups). The main question which needs to be addressed by this gathered experimental database is how much does fibers can be play the main role of reinforcement. For checking the range of low reinforcement ratio, various concrete design codes were used in the present study including (a) ACI 318-19 with $\rho_{min} = max\{(0.25\sqrt{f_c'}/f_y)\ and\ (1.4/f_y)\}$; (b) Eurocode 2 with $\rho_{min} = max\{(0.26 f_{ctm}/f_y)\ and\ 0.0013\}$; (c) CSA A23.3 with $\rho_{min} = 0.2 f_c'/f_y$; (d) IS 456 with $\rho_{min} = 0.85 f_c'/f_y$; and (e) fib Model Code 2010 with $\rho_{min} = max\{(k_c f_{ct.cff}/f_{yd})\ and\ 0.0013\}$ where $k_c \approx 0.6-0.8$ and $f_{yd} = f_y/\gamma_s$. The analysis depicted that all (100%) the gathered database have reinforcement ratio lower than the minimum value recommended by Eurocode 2, CSA A23.3, IS 456, and fib Model Code 2010. However, ACI 318-19 recommends a more unconservative model than other deign codes. The details of input variables are summarized in Table 2. In the proposed flexural strength model tailored for ductile HPC beams with low or very low reinforcement ratios and approximately 2.0% steel fiber content, the total bending capacity is conceptualized as the sum of three distinct contributions: Msteel, Mfiber, and Mmatrix.

This decomposition is not only physically intuitive but also reflects the complex, multi-scale load-bearing behavior of ductile HPC. First, Msteel accounts for the conventional tensile reinforcement provided by steel bars, which remains essential but is purposefully minimized in this category of structural elements. The inclusion of Mfiber represents the tensile contribution of dispersed steel fibers within the matrix, introduced specifically to compensate for the reduced volume of rebar and to enhance crack-bridging capacity and post-cracking ductility. This is particularly critical in ductile HPC, where fibers are not supplementary but rather serve as a strategic reinforcement component. The third component, Mmatrix, captures the residual tensile resistance provided by the ductile HPC matrix itself, which, unlike ordinary concrete, exhibits significant tensile capacity due to its extremely low water-to-binder ratio (typically 0.17–0.19), high binder content, dense microstructure, and improved bond characteristics. This intrinsic matrix strength can contribute meaningfully to flexural behavior before cracking and in the early stages of crack development. Including Mmatrix is therefore critical for accurately capturing the contribution of the ductile HPC matrix, especially in mixes where the synergy between fine powders, silica fume, and low porosity leads to a measurable tensile stress capacity. Together, these three components provide a comprehensive and realistic representation of the load-resisting mechanism in ductile HPC beams with minimal reinforcement, supporting both predictive accuracy and physical interpretation. As shown in Eq. (1), this model was developed to predict the flexural capacity of reinforced concrete (RC) beams made with ductile HPC or UHPC, particularly in configurations where steel reinforcement is limited (i.e., low or very low reinforcement ratio). The model decomposes the total bending moment capacity into three distinct contributions:

$$M_n = M_{steel} + M_{fiber} + M_{matrix} \tag{1}$$

where M_{steel}, M_{fiber}, and M_{matrix} Represent the portion of reinforcement ratio, fiber, and matrix in the flexural capacity of ductile HPC beams with low or very low reinforcement ratio $(\rho_s \sim 0)$. In the first step, the portion of reinforcement for calculating flexural capacity can be measured by Eq. (2), as follows:

$$M_{steel} = A_s f_y \left(d - \frac{a}{2}\right) \tag{2}$$

where $A_s = \rho_s bd$ Is the area of tensile steel reinforcement (mm^2), b is the beam width (mm), d is the effective depth of the beam (mm), f_y is the yield strength of reinforcement (MPa), a is equivalent stress block depth (mm). In the second step, the fiber portion of the flexural capacity calculation needs to be measured using Eq. (3). In traditional reinforced concrete beams, the tensile capacity is primarily provided by steel reinforcement bars. However, when the reinforcement ratio is low or very low, reinforcement alone cannot provide sufficient tensile strength to resist bending stresses effectively. This is where a high-volume fraction of fibers comes into play. The parameter M_{fiber} Quantifies the flexural capacity contribution due to dispersed steel fibers embedded throughout the concrete matrix. These fibers act as micro-reinforcement, bridging cracks, arresting crack propagation, and providing residual tensile strength even after initial cracking. Accordingly, the fiber contribution is expressed as:

$$M_{fiber} = (k_t V_f \sqrt{f_c'} + k_{fiber} f_{y.fiber}) b(h - a)\left(d - \frac{a}{2}\right) \tag{3}$$

where k_t is an empirically optimized coefficient representing fiber efficiency, V_f is the fiber volume fraction, h is the beam height, k_{fiber} is the fiber yield strength factor, and $f_{y.fiber}$ is the strength of fibers' material. The value of k_t= 0.0824 was obtained as the optimized tensile factor from the experimental database. The value of k_{fiber}=1.0×10^{-8} was found for the fiber yield strength contribution. The next step corresponds to the portion of the matrix in the flexural capacity measurement, which is provided by Eq. (4). In conventional reinforced concrete design, the tensile strength of the concrete matrix is often neglected due to its inherently brittle nature and low tensile capacity. However, in ductile HPC, this assumption is no longer valid. These advanced materials, due to their very low w/b ratios (typically 0.17–0.19) and dense binder-rich matrices, exhibit significantly improved tensile strength and post-cracking behavior, even before the addition of fibers. This contribution is especially important when the beam has low or very low reinforcement ratios, and the remaining tensile resistance must be shared among the matrix and fibers. As the ductile HPC mix contains high volumes of silica fume, fly ash, or other pozzolanic materials, which enhance the bond strength and toughness of the matrix, considering this parameter is essential for the calculation of M_n.

$$M_{matrix} = k_{ct} f_c' b(h - a)\left(d - \frac{a}{2}\right) \tag{4}$$

where k_{ct} is the optimized concrete matrix tension factor, which was found to be k_{ct}= 0.0109 according to the experimental database. As shown in Eqs. (3) and (4), the tensile strength of fiber and matrix can be described by Eqs. (5) and (6), respectively:

$$f_{t.f} = k_t V_f \sqrt{f_c'} \tag{5}$$

$$f_{ct} = k_{ct} f_c' \tag{6}$$

At the fourth step, the model uses a modified force equilibrium approach suited for low-reinforcement conditions. The stress block depth (a) is determined as:

$$a = \frac{A_s f_y}{\alpha_c f_c' b + \gamma(f_{t.f} + f_{ct}) b} \tag{5}$$

$$\alpha_c = \begin{cases} 0.85 & f_c' \leq 60 \\ 0.85 - 0.002(f_c' - 60) & 60 < f_c' \leq 200 \\ \min 0.65 & \end{cases} \tag{6}$$

$$\beta_1 = \begin{cases} 0.85 & f_c' \leq 28 \\ 0.85 - 0.05\dfrac{(f_c' - 28)}{7} & 28 < f_c' < 100 \\ 0.60 & f_c' \geq 100 \end{cases} \tag{7}$$

where γ The weighting factor for fiber and matrix contribution, gamma=0.40, was found for the collected database. The parameters α_c and β_1 are stress block factors are used to approximate the compressive force distribution in concrete, particularly in the concrete compression zone. The parameter α_c as the stress block intensity factor, which represents the average stress in the concrete's compression zone. It scales the compressive strength to account for the nonlinear nature of the concrete stress-strain curve. This means that as concrete strength increases, α_c decreases to reflect the more brittle behavior of high-strength concrete. The parameter of β_1 as stress block depth factor defines the depth of the equivalent rectangular stress block as a fraction of the neutral axis depth. These two factors make it possible to simplify complex nonlinear concrete behavior into a tractable and conservative analytical model. The schematic illustration of the proposed model is presented in Figure 1. It is worth mentioning that $\mathrm{k_{fiber}}$ and k_{matrix} were proposed as a function of $(d - a/2)$ to be consistent with the M_{steel}. The k_1 and k_2 were derived from adjustments with experimental results. Identifying the impact location of the F_{fiber} and F_{matrix} forces are quite challenging and hinges on numerous factors; thus, adjustments based on empirical data were employed in this study. It is also important to note that the present study precisely separated the roles of fiber and matrix, which have not been exactly studied by previous investigations in ductile HPC beams. It is worth mentioning that normally, residual flexural tensile strength (f_R) is used in predicting the flexural capacity of HPC beams. However, this parameter was not measured in some databases mentioned in Table 1, accordingly, considering this parameter could provide some inaccuracy in the proposed model.

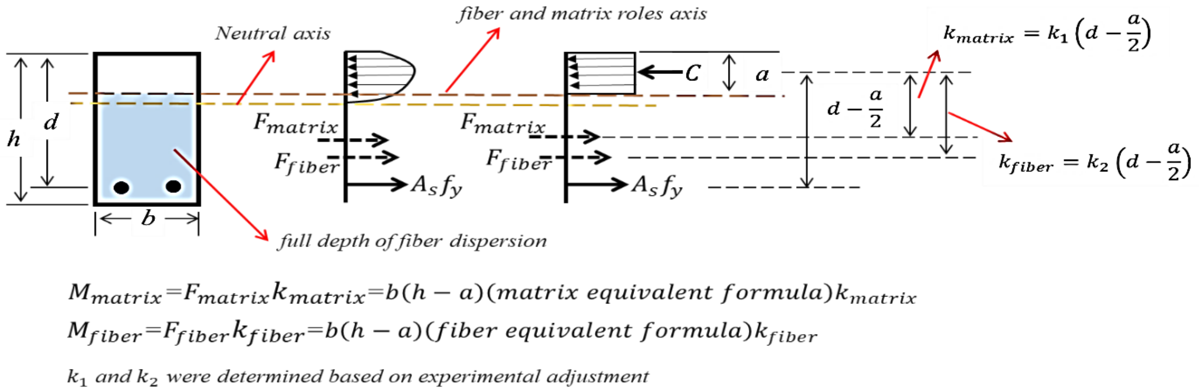

Figure 1: Schematic illustration of the proposed model for the ductile HPC beam.

Table 3.
Composition of ductile HPC mixture (kg/m^3)

Cement	SF	GGBFS	Silica Sand	w/b ratio	Micro steel fiber (volume fraction)
580	131	588	652	0.18	2.0%

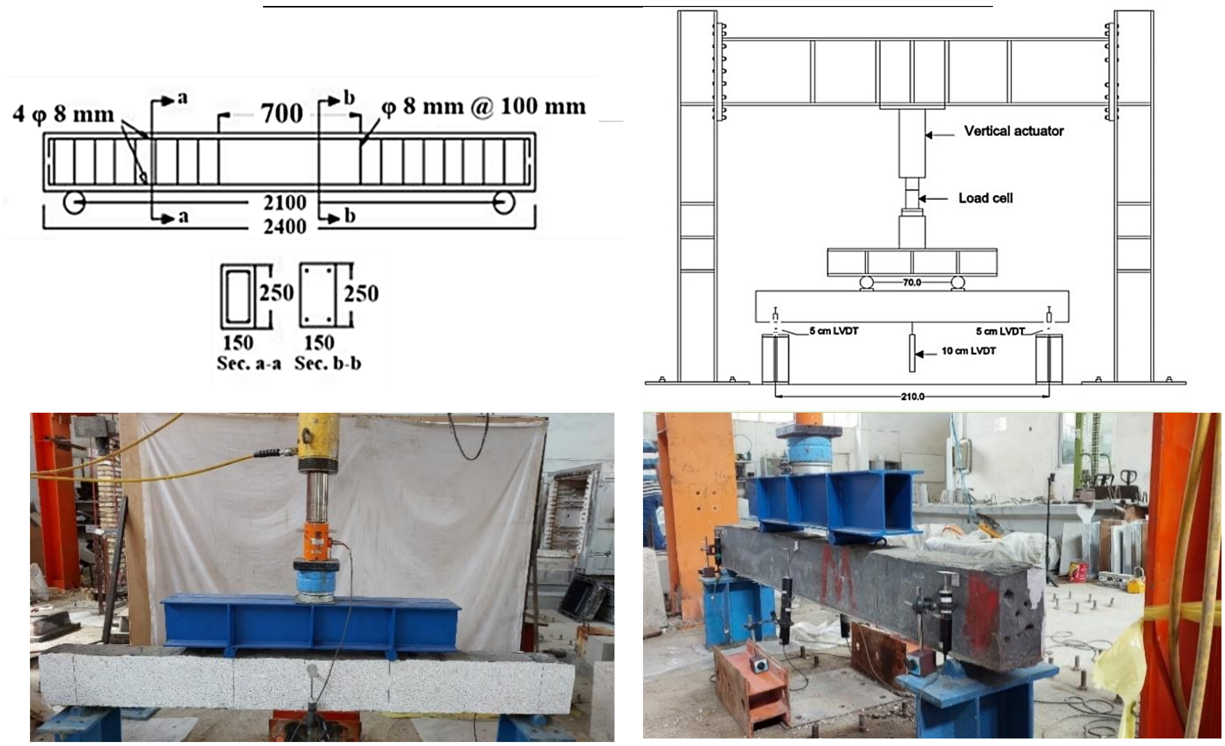

Figure 2: Details of the supplementary experimental program.

3. Experimental program

Ordinary Portland cement, ground granulated blast-furnace slag (GGBFS), and silica fume (SF) were utilized as binders for the ductile HPC mixture. As outlined in Table 3, the ductile HPC mixture features a w/b ratio of 0.18, a sand-to-binder (s/b) ratio of 0.50, and includes 2.0% micro steel fibers. The straight steel fibers employed had a length of 16 mm, an aspect ratio of 64, a tensile strength of 2720 MPa, and a modulus of elasticity of 210 GPa.

The addition of these fibers was intended to improve the mixture's tensile performance; nonetheless, this incorporation led to a decrease in the workability of the mixture. A polycarboxylate superplasticizer (SP) was methodically included in all formulations to mitigate this problem. As illustrated in Figure 2, a large-scale ductile HPC beam with a very low reinforcement ratio (ρs=0.32%) was designed to prevent shear failure, adhering to the recommendations set forth by the Japan Society of Civil Engineers (JSCE) [9], to evaluate their flexural capacity. For the shear reinforcement, 8 mm stirrups were employed with a spacing of 100 mm, and to maintain the vertical position of the shear reinforcements (stirrups) within the shear zone, a minimal longitudinal reinforcement ratio of ρs=0.32%was considered, consisting of four 8 mm diameter reinforcing bars. The overall length of 2400 mm and section of 150×250 mm2 were considered for the ductile HPC beam, which had a height-to-width ratio of around 1.67. Regarding the large-scale flexural test, the rate of the universal machine was around 0.4 mm/min.

4. Results & Discussion

A comprehensive experimental database gathered in Table 1 was used in the present study to check the performance of the proposed model. This experimental database contains various groups of large-scale beams to cover the lower and upper bound of the proposed model containing bending moments, including (a) some samples with no reinforcement ratio ($M_{steel} = 0$) but different type and volume fractions of fiber; (b) some samples with no low reinforcement ratio but no fibers ($M_{fiber} = 0$). The existence of these groups within the experimental database can help prove that more accurate coefficients exist within the model, especially. k_1 and k_2. Integral absolute error (IAE) and the coefficient of variation (COV) are two metrics used to assess the accuracy of current models. The COV is defined as the ratio of predicted to experimental values, while the expression for IAE is described in Eq. (8). IAE exhibits greater sensitivity compared to COV. These criteria have been used by many studies in this field to check the accuracy of the predictive analytical models [19-20]. A dependable model should have a lower IAE value and COV factors nearly equal to one to be effective and precise in predicting flexural capacity.

$$IAE = \sum \frac{\sqrt{(Experimental - Predicted)^2}}{\sum Experimental} \qquad (8)$$

The performance of the proposed model, as depicted in Figure 3, demonstrates its capability to accurately predict the flexural capacity of samples characterized by low reinforcement ratios and high fiber volume fractions. The model's accuracy is quantified using the IAE and COV.

The IAE, calculated using Eq. (8), is approximately 10.8%, with a COV of 1.04. This outcome reflects the robust performance of the proposed model, which is based on a dataset comprising 162 experimental samples from 16 distinct studies. Additionally, the individual contributions of steel, fibers, and the matrix were assessed through the proposed model to evaluate how alternative materials might replace the role of steel in large-scale beams with low reinforcement ratios. Consequently, the ratio of M_{steel}/M_n, M_{fiber}/M_n, and M_{matrix}/M_n were calculated and illustrated in Figure 4, which is called "bending moment contribution ratio (-)". This analysis demonstrates that reducing the reinforcement ratios increases the roles of fiber and matrix for handling the flexural capacity of ductile HPC beams. The difference between the roles of fiber and matrix separately in compensating for the reinforcement ratio role is clearly shown in Figure 4.

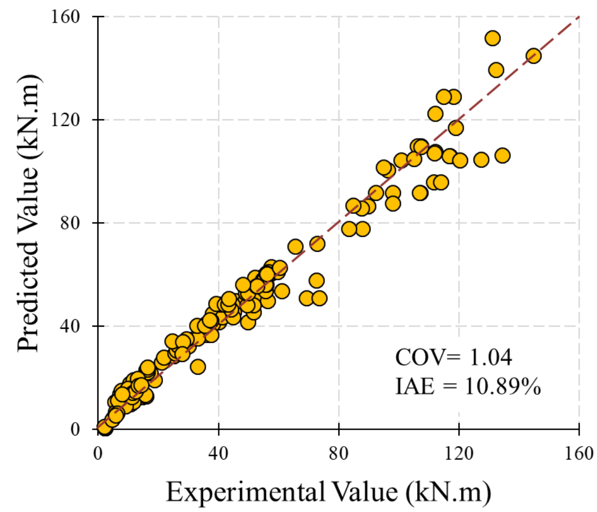

Figure 3: Performance of the proposed model for predicting the flexural capacity of ductile HPC beams with a low reinforcement ratio.

As mentioned, a supplementary experimental test was conducted to validate the proposed model. As shown in Figure 5(a), the tested large-scale ductile HPC beam had a bending moment capacity of 27.96 kN·m with clear ductile failure without unexpected failure due to the low reinforcement ratio. The tested beam had compressive strength of 100 MPa, direct tensile strength of 10 MPa, and splitting tensile strength of 12 MPa. High volume fraction of fibers within this ductile HPC beam (2.0%). The ductility index was calculated using the ratio of δ_u/δ_y, where δ_u and δ_y correspond to the initial and final displacement linked to 85% of the maximum force $0.85F_{max}$. As shown in Figure 5(a), the ductility ratio of 7.0 was measured for the tested beam. To check the performance of ductile HPC beam tested in the present study, various flexural capacity models proposed by standards, including ACI 544.4R, JSCE-SF4, RILEM TC 162-TDF, and Fib Model Code 2010. Failure and crack propagation illustration of the tested beam is also shown in Figure 5(a). The performance of the proposed model in predicting the flexural capacity of the test beam is shown in Figure 5(b). The results showed that the proposed model precisely predicted the flexural capacity of the tested beam with 4.5% deviation. The analysis showed that reinforcement, fiber, and matrix have 8.1%, 10.4%, and 5.4% of the total bending moment, showing that fibers along with matrix compensate for the lack of adequate reinforcement within the ductile HPC beam, which can be a unique advantage of such concrete type. Moreover, the analysis showed that the fiber role is higher than reinforcement and matrix for the tested beam. Accordingly, the results show that the proposed model is a pioneer model to precisely separate the role of reinforcement (steel and fiber) within the ductile HPC beam on tolerating bending moment.

As mentioned in Table 4, a parametric study was also conducted in the present study using statistical analysis through Minitab software to discuss the sensitivity analysis of the input features in this flexural model. The ratio of M_{fiber}/M_n and $M_{matrix}/M_n$was used as “fiber and matrix roles, respectively” in this statistical analysis. Main effect plots of roles are shown in Figure 6. The provided analysis presents a comparison of how various input parameters affect the roles of fibers and matrices. As the volume fraction of fiber increases, the fiber role enhances, demonstrating that a higher proportion of fibers in the composite directly boosts their reinforcing capacity. In contrast, a rise in the w/b ratio leads to a slight reduction in the fiber role, suggesting that an increased water content may compromise the fiber-matrix interface, thereby diminishing the effectiveness of the fibers. The reinforcement ratio (ρ_s) has a significant negative impact on the fiber role, indicating that using an adequate reinforcement ratio within the beam section can be dominant in tolerating bending moment, thereby reducing both the roles of fiber and matrix. Furthermore, a size effect coefficient was also used as an input feature of the sensitivity analysis, which was calculated as $1/\sqrt{d}$, where d is the effective depth of the beam section. The size effect coefficient shows a moderate negative influence, meaning that an increase in the size coefficient slightly reduces the effectiveness of fibers in mechanical performance, likely due to limitations in stress transfer or distribution. Likewise, a rise in the fiber aspect ratio leads to a slight decline in fiber efficiency, implying the existence of an optimal aspect ratio, beyond which fibers may become less effective due to potential aggregation or poor stress transfer. On the other hand, the fiber yield strength positively affects the fiber role, signifying that fibers with greater strength enhance the reinforcing efficiency directly. Regarding the matrix role, the pattern differs: an increase in fiber volume fraction significantly diminishes the matrix role, indicating that as fiber content increases, the load-bearing function shifts from the matrix to the fibers. The w/b ratio also markedly reduces the matrix's contribution, likely due to matrix weakening associated with higher porosity and decreased strength at elevated w/b ratios.

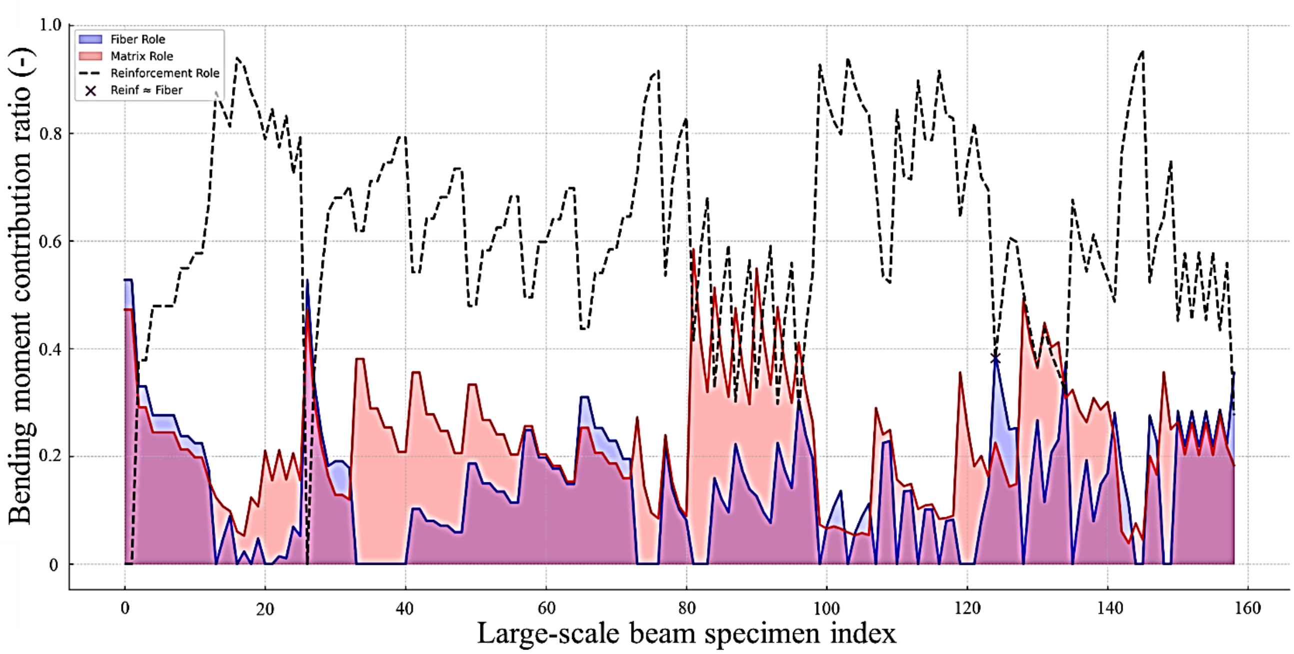

Figure 4: Portions of variables in predicting the flexural capacity of ductile HPC beams with low reinforcement ratios.

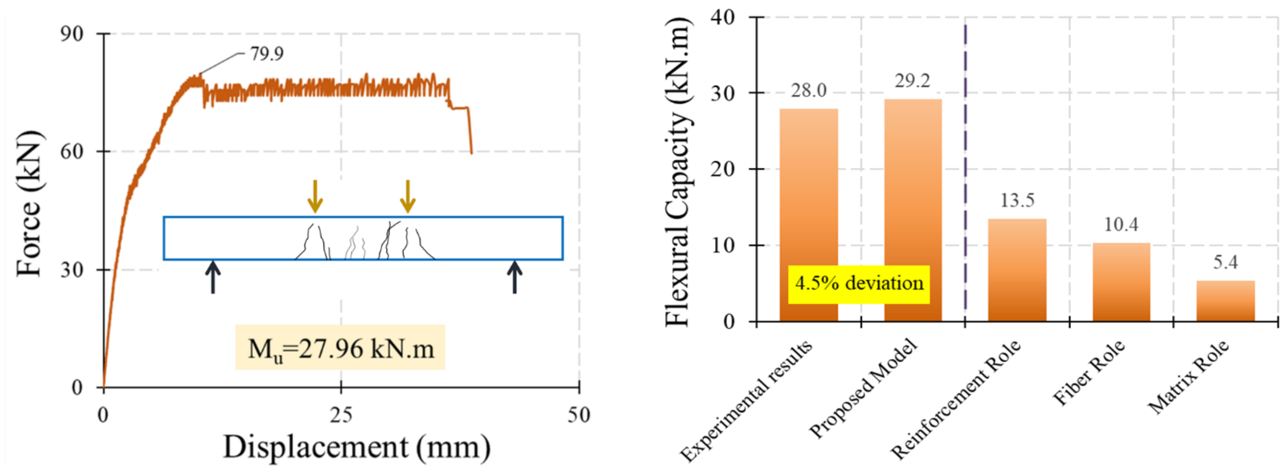

(a)

(b)

Figure 5: Performance of the proposed model with supplementary experimental results: (a) experimental load-displacement curve; (b) compared with the proposed model.

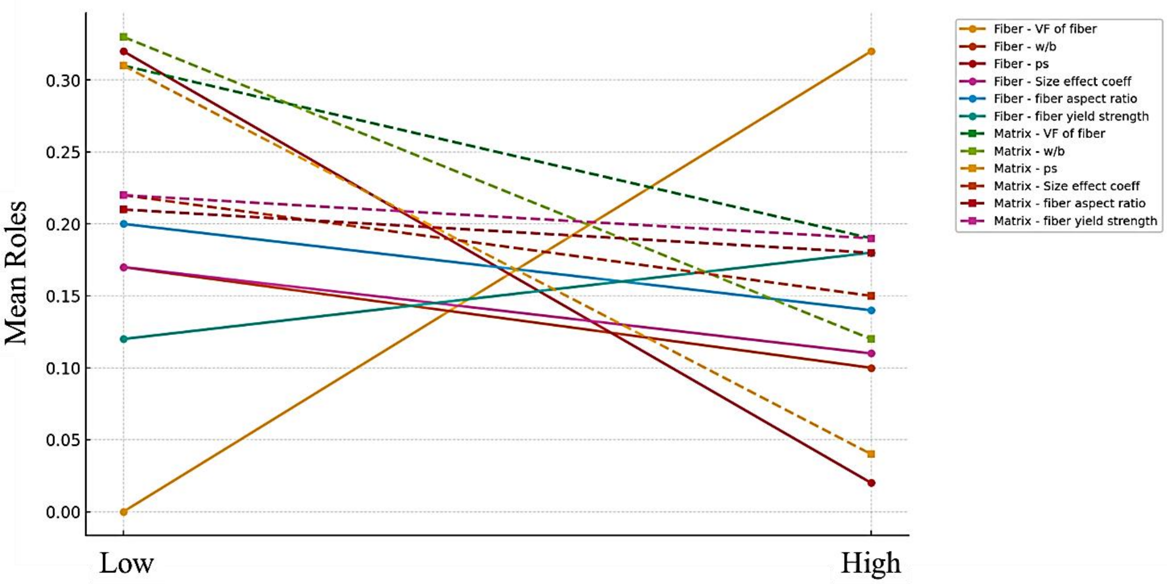

Figure 6: Main effect plots for fiber and matrix roles.

Table 4.

Statistical ANOVA analysis of the fiber and matrix role.

	Terms	DF	Adj SS	Adj MS	F-value	P-value	VIF
Fiber Role	V_f	1	0.74	0.74	234.46	0.000	1.59
	ρ_s	1	0.313	0.314	99.84	0.000	1.22
	Size effect	1	0.0093	0.0093	2.96	0.088	1.24
	Fiber strength	1	0.0061	0.0061	1.95	0.165	2.66
	Fiber aspect ratio	1	0.0051	0.0051	1.61	0.206	2.00
	w/b	1	0.0086	0.0086	2.74	0.100	1.71
Matrix Role	V_f	1	0.138	0.138	39.77	0.000	1.59
	ρ_s	1	0.819	0.819	235.76	0.000	1.22
	Size effect	1	0.017	0.017	4.83	0.030	1.24
	Fiber strength	1	0.002	0.002	0.69	0.407	2.66
	Fiber aspect ratio	1	0.000	0.000	0.05	0.828	2.00
	w/b	1	0.481	0.481	138.40	0.000	1.71

Similarly, a rise in reinforcement ratio (ρ_s) greatly lowers the matrix contribution. An increase in the size effect coefficient slightly diminishes matrix effectiveness, suggesting limitations in the matrix's capacity to accommodate stress due to larger structural influences. Additionally, the fiber aspect ratio presents only minor negative effects, indicating that the matrix role is not heavily influenced by fiber geometry. Finally, the fiber yield strength has a negligible impact on the matrix role, suggesting that the strength characteristics of fibers mainly affect fiber efficiency without significantly altering the core load-bearing properties of the matrix. It is worth mentioning that the high volume of powders 9typically cement, SF, FA, and GGBFS) play a major role in matrix contribution, which is totally different from the fiber role's constitution.

The Pareto charts obtained from the statistical analysis of fiber and matrix roles are shown in Figure 7. A Pareto chart is a statistical analysis that combines a bar and line graph to display the relative importance of different factors in a dataset, where the bars represent individual values in descending order and the line shows the cumulative total. In statistical analysis, particularly in quality control and experimental design, it helps identify the "vital few" factors that contribute most significantly to an outcome. Based on Pareto charts (Figure 7), for fiber role, the most statistically significant effects—those exceeding the reference line—include AB (the interaction between volume fraction of fiber and ρ_s), BB (the quadratic effect of ρ_s), and CC (the quadratic effect of size effect coefficient), indicating that these terms have a dominant influence on the fiber role in total bending moment. The strong presence of AB suggests that the combined effect of the volume fraction of fiber and ρ_s is more impactful than their contributions, while BB and CC highlight nonlinear relationships, meaning that extreme values of ρ_s and size effect coefficient may disproportionately affect fiber performance. Additionally, AC (interaction between volume fraction of fiber and size effect coefficient) and AD (interaction between fiber volume fraction and fiber yield strength) also appear notable, though slightly less pronounced. For Matrix Role, the dominant effects are BB (the quadratic effect of ρ_s), showing that the reinforcement ratio of section controls the efficiency of matrix role in the proposed flexural strength model. The appearance of CC (the quadratic effect of the size effect coefficient), and FF (the quadratic effect of w/b ratio) imply that fiber volume fraction and fiber yield strength may also play a role in matrix behavior, hinting at cross-dependent mechanisms between fiber and matrix phases. The absence of certain main effects (e.g., A, B, C alone) in the most significant terms suggests that interactions and quadratic effects are more critical than individual linear factors in your system.

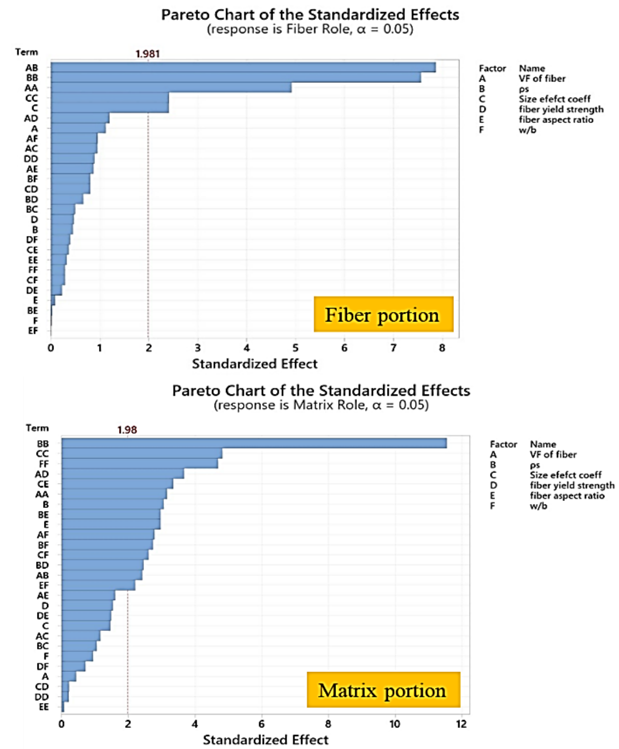

Figure 7: Pareto charts of fiber and matrix roles.

Response surface analysis from "Design of Experiments (DOE)" for fiber and matrix roles is illustrated in Figure 8. Regarding the fiber role, the contour plot demonstrates that the volume fraction of fibers plays the most dominant parameter when the $\rho_s < 0.01$, where a very low reinforcement ratio is considered in ductile HPC beams. Moreover, the analysis depicts that the existence of high-volume fraction fiber with low number aspect ratio has no promising influence on the fiber role, while fiber aspect ratio ranging from 400 to 800 guarantees a high effect of fiber volume fraction. Similarly, fiber strength is also critical so that a high-volume fraction of fibers cannot be efficient for fibers with a strength lower than 2000 MPa. Based on the response surface contour, the highest impact of fiber volume fraction in the fiber role formula is also obtained for the size effect factor higher than 0.090. However, the analyses depict that the variation of the w/b the ratio has the lowest influence on the fiber role predicting formula. Regarding matrix role, the variation of fiber volume fraction also has a minor influence on the matrix role, while using the lowest content of reinforcement ($\rho_s < 0.02$) has a considerable impact. Also, using a fiber aspect ratio lower than 300 provides a situation that. $M_{matrix} > M_{fiber}$. Similarly, for a case where the matrix role is dominant over the fiber role, the fiber strength should be lower than 1500 MPa, as illustrated in Figure 8. In the case of the size effect value lower than 0.07, along with $w/b \leq 0.20$, the matrix role is dominant as compared to the fiber role for ductile HPC beams containing a low reinforcement ratio.

The overlaid contour plots from DOE for fiber and matrix roles are depicted in Figure 9. The domain of 0.20-0.52 for fiber role was selected for this optimization analysis. The analysis showed that a reinforcement ratio lower than 0.015 and a fiber volume fraction of 2.0% can result in the maximum performance of fibers in achieving the highest M_{fiber}. Regarding the size effect parameter and fiber strength, no clear trend was observed, while the current observation confirmed that a size effect parameter higher than 0.09 and fiber strength higher than 2500 MPa can generate the highest fiber role in the total bending moment predicting model. Regarding the w/b ratio, the analysis clearly showed that the addition of fibers in $w/b > 0.40$ almost has no impact on the bending moment. Similarly, as shown in Figure 9, a fiber aspect ratio higher than 400 causes the minor influence of fibers within the bending moment calculation. A similar range of 0.2-0.58 was selected for optimization analysis of the matrix role. The analysis showed that fiber yield strength higher than 2000 MPa and reinforcement ratio higher than 0.01 increase the non-feasible region, meaning that the M_{matrix} can be ignored in the calculation of total bending moment. Furthermore, the analysis showed that for $w/b < 0.3$ and $100 < fiber\ aspect\ ratio < 300$, the value of M_{matrix} should be considered in the total bending moment calculation.

The main question is whether, by variation of input features, the fiber or the matrix is dominant in compensating reinforcement within ductile HPC beams. To answer this question, the boxplots are illustrated in Figure 10. Regarding fiber content, dominantly higher fiber volume fractions correlate strongly with cases where the fiber role exceeds the matrix role. The analysis of the reinforcement ratio (ρ_s) showed that slightly lower

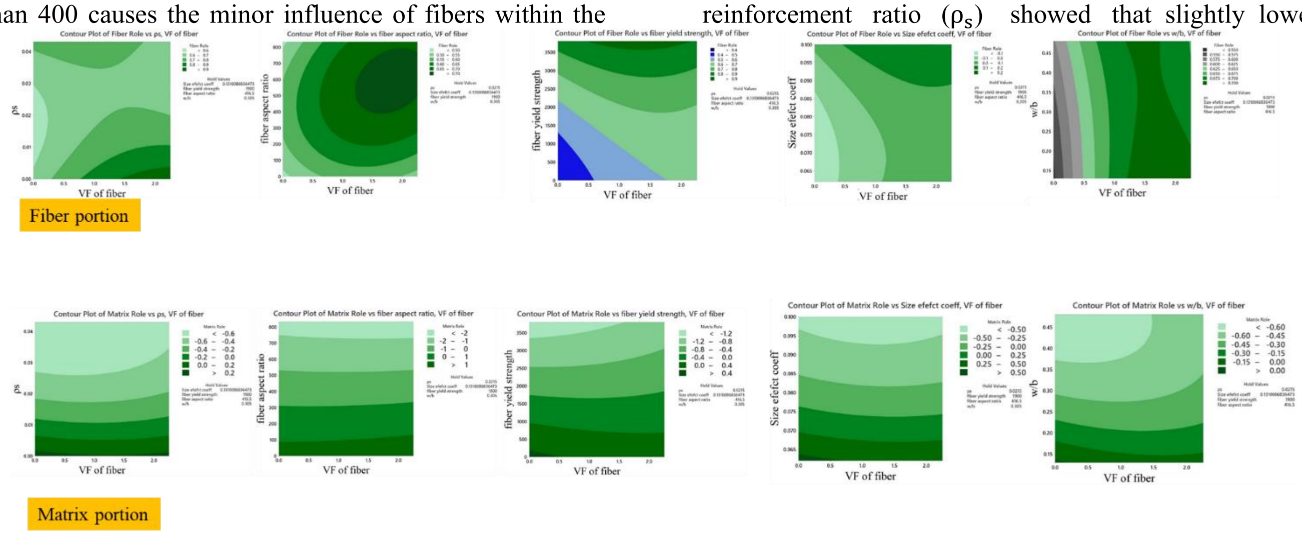

Figure 8: Response surface analysis from DOE for fiber and matrix roles.

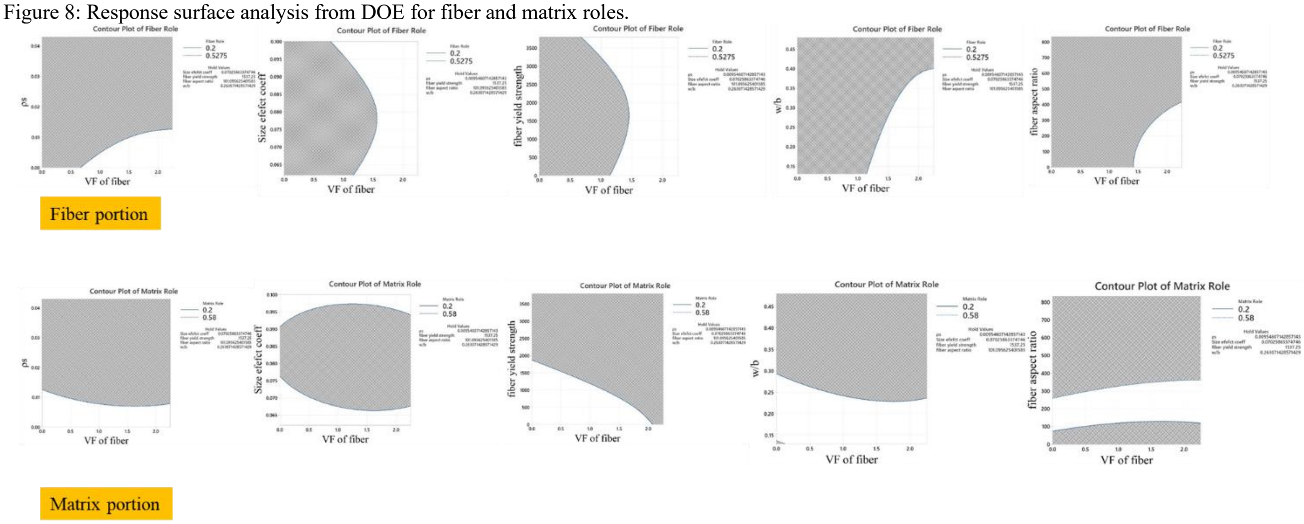

Figure 9: Overlaid contour plot from DOE for fiber and matrix roles.

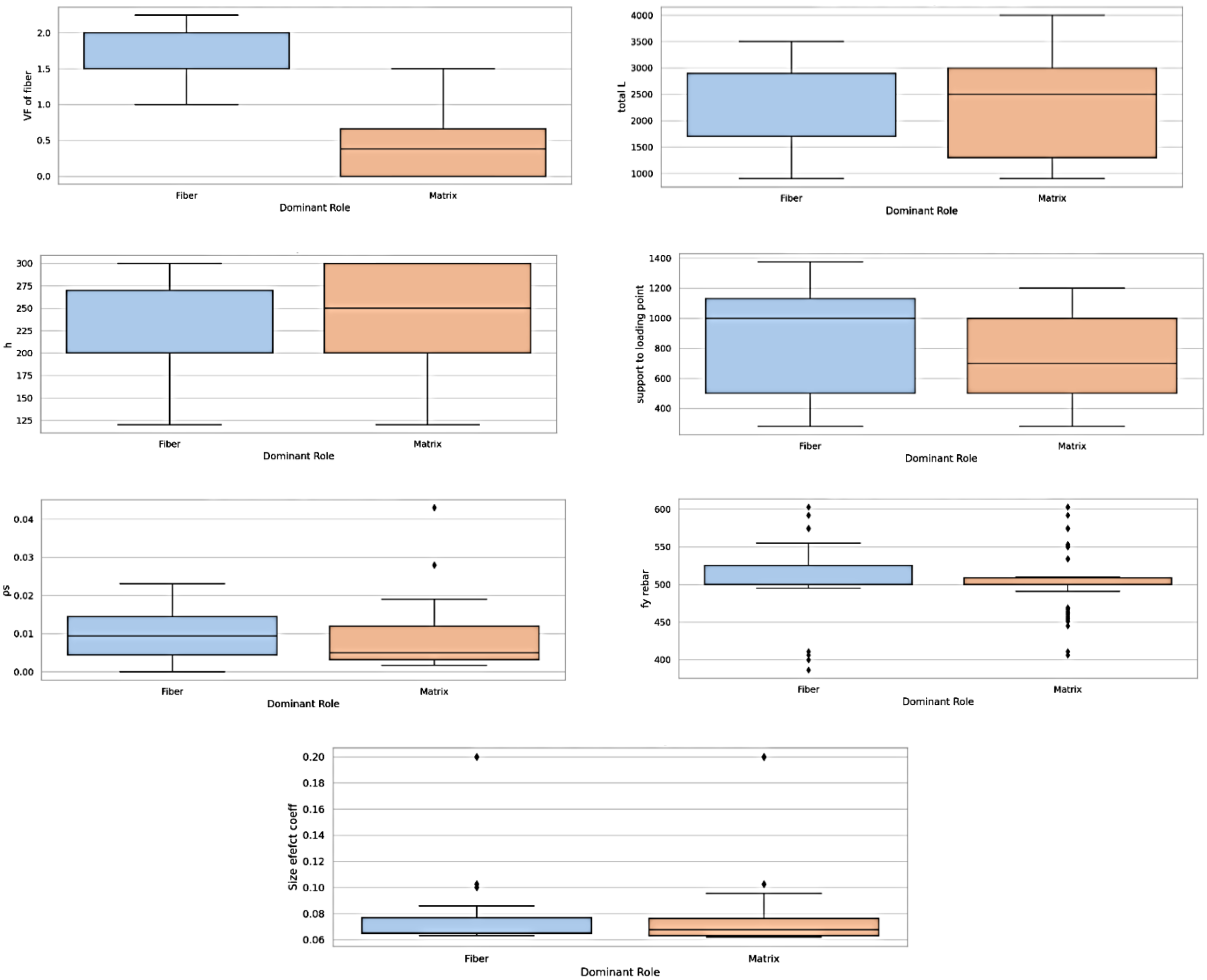

Figure 10: Results of box plots illustrating the distribution of input parameters for the Fiber and Matrix roles.

reinforcement ratios tend to favor fiber dominance. Also, the analysis depicted that slightly shorter specimen lengths tend to favor fiber dominance. Moreover, lower size effect coefficients slightly favor the fiber role, indicating fibers are more effective at smaller scales. Generally, the analysis confirmed that the strongest factor differentiating fiber and matrix dominance is the fiber volume fraction.

A comparison between predicting models suggested by various concrete design codes and the proposed model of the presented study is conducted and shown in Table 5. The bending moment of the ductile HPC beam tested in the present study was selected as the criterion for comparing the efficiency of the models. Based on the deviation analysis, the current design codes significantly underestimate the flexural capacity of ductile HPC beams, with deviation ranging from -20.0% to -43.57%, while the proposed model precisely predicts the bending moment with +4.25% deviation. Among the proposed models, the analysis depicts that JSCE-SF4 (2002) showed the lowest deviation from the experimental results, while ACI 544.4R has the highest deviation. The high accuracy of the proposed model in the present study is a promising finding for use in the design codes in predicting the flexural capacity of HPC beams.

Table 5.
Performance of predicting equations compared to the experimental beam

Models		Predicted (kN.m)	Deviation from experiment (%)
Design Codes	ACI 544.4R	15.8	-43.57
	JSCE-SF4 (2002)	22.4	-20.0
	RILEM TC 162-TDF	18.9	-32.5
	Fib Model Code (2010)	20.2	-27.86
	Proposed model	29.2	+4.28

5. Conclusions

A novel analytical approach was followed by the present study to propose a unique predicting flexural capacity model for large-scale ductile HPC (or other fiber-reinforced concrete types) beams containing almost negligible reinforcement content. A comprehensive experimental database containing 162 datasets was gathered from the literature to determine the performance of the proposed model. Moreover, a supplementary experimental program containing one large-scale ductile HPC beam was produced to check the accuracy of the model. The results showed that the proposed bending model has IAE=10.8% and COV=1.04, which clearly shows the high accuracy of the proposed model compared to the experimental database (162 experimental large-scale beam tests). Furthermore, comparing the experimental result of the tested beam and the proposed model showed a 4.5% deviation, which confirms the performance of the flexural capacity formulation. A parametric statistical analysis using Minitab software was also conducted to check the influence of critical parameters affecting the fiber and matrix role. Different input features were considered in this statistical sensitivity analysis. Generally, the parametric study emphasized that the volume fraction of fiber, w/b ratio of concrete mixture, reinforcement ratio of beam, fiber strength (or type), and fiber aspect ratio have a considerable impact on the role of fiber and matrix in compensating the flexural capacity required due to the inadequate reinforcement ratio. Also, the size effect parameter was found to be important in the proposed model. More experimental studies are required for future research to validate the efficiency of the proposed model, especially for different types of HPC mixtures. Moreover, only monotonic loading was considered for the proposed flexural capacity model, while more analytical work should be performed by future studies to extend the proposed model for cyclic conditions.

Notations

A_s	area of reinforcement in the beam section
b	beam width
d	Effective depth of the beam section
f_c'	concrete compressive strength
f_{ct}	matrix tensile strength
f_{ctm}	cracking control limit strength
f_R	Residual flexural tensile strength
f_y	yield strength of reinforcement
$f_{y.fiber}$	strength of fibers' materials
$f_{t.f}$	fiber residual tensile strength
h	beam height
k_t	optimized fiber tensile strength factor
k_{ct}	optimized concrete matrix tension strength factor
k_{fiber}	fiber yield strength factor
M_n	flexural capacity of the beam
M_{steel}	portion of reinforcement in flexural capacity
M_{fiber}	portion of reinforcement in flexural capacity
M_{matrix}	portion of the matrix in flexural capacity
V_f	fiber volume fraction (%)
α_c	stress block intensity factor
β_1	stress block depth factor
a	neutral axis depth
γ	weighting factor for fiber & matrix contribution to neutral axis
ρ_s	reinforcement ratio of the beam section

References

[1] Yang, In Hwan, Changbin Joh, and Byung-Suk Kim. "Structural behavior of ultra-high performance concrete beams subjected to bending." Engineering Structures 32.11 (2010): 3478-3487. https://doi.org/10.1016/j.engstruct.2010.07.017

[2] Meda, A., F. Minelli, and G.A. Plizzari. "Flexural behaviour of RC beams in fibre reinforced concrete." Composites Part B: Engineering 43.8 (2012): 2930-2937. https://doi.org/10.1016/j.compositesb.2012.06.003.

[3] Kamal, M., M. Safan, Z. Etman, and R. Salama. "Behavior and strength of beams cast with ultra high strength concrete containing different types of fibers." HBRC Journal 10.1 (2014): 55-63. https://doi.org/10.1016/j.hbrcj.2013.09.008.

[4] Abbas, S., A.M. Soliman, and M.L. Nehdi. "Exploring mechanical and durability properties of ultra-high performance concrete incorporating various steel fiber lengths and dosages." Construction and Building Materials 75 (2015): 429-441. https://doi.org/10.1016/j.conbuildmat.2014.11.017.

[5] Yoo, Doo-Yeol, Nemkumar Banthia, and Young-Soo Yoon. "Experimental and numerical study on flexural behavior of UHPFRC beams with low reinforcement ratios." (2016). http://hdl.handle.net/1807/75095.

[6] Yoo, Doo-Yeol and Doo-Yong Moon. "Effect of steel fibers on the flexural behavior of RC beams with very low reinforcement ratios." Construction and Building Materials 188 (2018): 237-254. https://doi.org/10.1016/j.conbuildmat.2018.08.099.

[7] Cardoso, D.C., R.C. Silva, J.P.C. Rodrigues, and A.T. Marques. "Influence of steel fibers on the flexural behavior of RC beams with low reinforcing ratios: Analytical and experimental investigation." Composite Structures 222 (2019): 110926. https://doi.org/10.1016/j.compstruct.2019.110926.

[8] Abbasi Parvin, Younes, Mohammad Ali Hadianfard, Amirhossein Gholamrezaei, and Sajad Bagheryan. "Flexural behavior of UHPC beams reinforced with macro-steel fibers and different ratios of steel and GFRP bars." Journal of Rehabilitation in Civil Engineering 12.2 (2024): 41-57. https://doi.org/10.22075/jrce.2023.28070.1695.

[9] JSCE. "Standard Specifications for concrete structures." Japanese Society for Civil Engineering (JSCE) (2010). https://www.jsce-int.org/system/files/JGC15_Standard_Specifications_Design_1.0.pdf.

[10] Yoo, Doo-Yeol and Young-Soo Yoon. "Structural performance of ultra-high-performance concrete beams with different steel fibers." Engineering Structures 102 (2015): 409-423. https://doi.org/10.1016/j.engstruct.2015.08.029.

[11] Singh, M., I. Sheikh, M. Ali, M. Shariq, and A. Baqi. "Experimental and numerical study of the flexural behaviour of ultra-high performance fibre reinforced concrete beams." Construction and Building Materials 138 (2017): 12-25. https://doi.org/10.1016/j.conbuildmat.2017.02.002.

[12] Hasgul, U., K. Turker, A. Birol, and A. Yavas. "Flexural behavior of ultra-high-performance fiber reinforced concrete beams with low and high reinforcement ratios." Structural Concrete 19.6 (2018): 1577-1590. https://doi.org/10.1016/j.conbuildmat.2017.02.002.

[13] Gümüş, M. and A. Arslan. "Effect of fiber type and content on the flexural behavior of high-strength concrete beams with low reinforcement ratios." Structures (2019). https://doi.org/10.1016/j.istruc.2019.02.018.

[14] Liu, S., W. Wang, L. Mao, and Z. Li. "Flexural load-deflection performance of polyvinyl alcohol fiber reinforced cementitious composite beams." Construction and Building Materials 223 (2019): 1135-1144. https://doi.org/10.1016/j.conbuildmat.2019.07.215.

[15] Turker, K., U. Hasgul, A. Birol, and A. Yavas. "Hybrid fiber use on flexural behavior of ultra high performance fiber reinforced concrete beams." Composite Structures 229 (2019): 111400. https://doi.org/10.1016/j.compstruct.2019.111400.

[16] Conforti, A., R. Zerbino, and G. Plizzari. "Assessing the influence of fibers on the flexural behavior of reinforced concrete beams with different longitudinal reinforcement ratios." Structural Concrete 22.1 (2021): 347-360. https://doi.org/10.1002/suco.201900575.

[17] Chen, H.-J., W.-C. Huang, C.-C. Huang, and Y.-W. Chan. "Flexural behavior of ultra-high-performance fiber-reinforced concrete beams after exposure to high temperatures." Materials 14.18 (2021): 5400. https://doi.org/10.3390/ma14185400.

[18] Jin, H., F. Li, and D. Hu. "Research on the flexural performance of reinforced engineered cementitious composite beams." Structural Concrete 23.4 (2022): 2198-2220. https://doi.org/10.1002/suco.202100012.

[19] Mousavi, S., M. Dehestani, and S. Mousavi. "Bond strength and development length of glass fiber-reinforced polymer bar in unconfined self-consolidating concrete." Journal of Reinforced Plastics and Composites 35.11 (2016): 924-941. https://doi.org/10.1177/0731684416632930.

[20] Wu, Y. F. and X. M. Zhao. "Unified bond stress–slip model for reinforced concrete." Journal of Structural Engineering 139.11 (2013): 1951-1962. https://doi.org/10.1061/(ASCE)ST.1943-541X.0000747.

Journal of Civil Engineering Researchers

Journal homepage: www.journals-researchers.com

Retaining Structures in Slope Stabilization: A Comparative Analysis on Safety and Cost Effectiveness

Selman Kahraman,[a,*] İnan Keskin,[a] Taner Gürbüz[a]

[a] Faculty of Engineering, Karabuk University, Karabuk, Turkey.

ABSTRACT

This study aims to investigate the safety and cost-effectiveness of different retaining structures, namely gravity stone walls, reinforced concrete cantilever walls, and pile shoring systems, in the stabilization of slopes with varying excavation depths. A parametric model was developed and analyzed using PLAXIS 2D (based on the finite element method) and İstCAD software (based on limit equilibrium principles in accordance with the Turkish Seismic Code, TBDY-2018). The results revealed that gravity stone walls are the most economical solution for excavation depths up to 5 meters. For intermediate depths (5–9 meters), cantilever retaining walls offer a more feasible and structurally efficient alternative. ıt shows that beyond 9 meters, traditional retaining systems become insufficient in terms of both stability and displacement limits, necessitating the use of pile shoring systems. The study provides a comparative assessment of these solutions, considering safety factors, lateral displacements, construction costs, and field applicability. These findings offer practical guidance for engineers in selecting optimal stabilization strategies under varying project constraints.

ARTICLE INFO

Received: May 05, 2025
Accepted: August 10, 2025

Keywords:
Slope Stabilization
Retaining Structures
Cost-Effectiveness Analysis
PLAXIS 2D
Natural Disaster

DOI: 10.66224/JCER.7.3.15
DOR: 20.1001.1.2538516.2025.7.3.2.2

1. Introduction

Rapid urbanization driven by global population growth has led to a significant increase in the demand for residential and infrastructural development, particularly in geologically challenging terrains such as slopes. In many countries characterized by rugged topography, this demand has resulted in the expansion of settlements onto unstable slopes, thereby escalating the risk of geotechnical hazards such as landslides. Consequently, various construction activities, including residential buildings, industrial facilities, dams, and transportation infrastructure, have increasingly encroached upon geotechnically sensitive areas. As a result of the increase in construction on the slopes, an increase in the danger and risk of landslides has also been observed. Several human-induced factors contribute to slope instability in such areas, including excavations, steepened slopes, accumulation of excavation waste, construction of tall buildings, increased pore water pressure due to inadequate drainage, and damage to natural

* Corresponding author. Tel.: +903704184200; e-mail: inankeskin@karabuk.edu.tr.

vegetation. In addition, natural disasters such as earthquakes and volcanic activity serve as major triggers for landslide events in slope regions. Another problem of the issue is that landslide and/or landslide risk areas are given construction permits without sufficient research due to political and financial situations or public insistence. The increase in landslides in Turkey and the world shows the importance of the issue and the necessity of increasing studies by benefiting from current approaches in slope stabilization methods [1]. Landslide events that occur every year in Turkey cause serious loss of life and property, and this situation requires more research on the prevention and management of landslides [2].

Turkey's geographical and geological characteristics, including active fault lines, steep topography, and irregular rainfall patterns, render it particularly susceptible to landslides. When all these reasons come together, slope failures are inevitable and sometimes life and property security are under threat. When looking at the statistics of natural disasters in Turkey, losses caused by landslides are second after earthquakes [2], [3]. It is extremely important to conduct risk and priority analyses of landslides that occur due to these adverse morphological, topographic, geological and meteorological conditions and to establish permanent security in problematic slopes [4], [5], [6].

Various engineering techniques have been developed to mitigate slope instability, ranging from traditional retaining walls to advanced reinforcement systems [7], [8], [9], [10], [11]. In the context of slope stability analysis, both Limit Equilibrium Methods (LEM) and Finite Element Methods (FEM) are widely used to evaluate the effectiveness of various reinforcement techniques, including the use of anti-slip piles [12], [13], [14], [15]. The Limit Equilibrium Method remains a widely accepted approach due to its simplicity and ease of application. The method allows calculating the factor of safety against sliding by analyzing the surfaces of possible failures within the slope. However, LEMs have limitations, especially in their inability to account for complex interactions between the soil and structural elements such as piles, which can significantly affect stability [16]. Some studies in the literature highlight the advantages of integrating finite element analysis with limit equilibrium methods to increase the accuracy of slope stability assessments [16], [17]. Furthermore, recent studies emphasize that 3D finite element methods provide a more detailed understanding of the behavior of pile-reinforced slopes, as they can model the complex interactions between soil and reinforcement structures [9], [18].

Within the scope of this study, a model slope geometry was defined for conducting slope stability analyses. The soil profile and material model parameters were kept constant across all simulations to ensure consistency. Three types of retaining structures, gravity stone walls, reinforced concrete cantilever walls, and pile shoring systems, were designed for varying excavation heights and analyzed through multiple iterations. Numerical simulations were performed using PLAXIS, a finite element-based software commonly employed in geotechnical engineering. Following these analyses, structural stability checks, reinforced concrete design, and quantity estimations were carried out using İstCAD, in accordance with the Turkish Building Earthquake Code (TBDY-2018). Additionally, overall structural safety was assessed via equivalent static limit equilibrium analyses based on the slice method, also implemented in İstCAD. The resulting safety factors were then compared with those obtained from PLAXIS simulations to evaluate consistency and reliability between the two approaches.

2. Material Method

2.1. Model Slope and Engineering Properties

To evaluate the performance of gravity stone walls, reinforced concrete cantilever retaining walls, and pile shoring systems used in stabilizing problematic slopes, a representative model slope was created using PLAXIS software. Figure 1a presents the geometry and coordinates of the modeled slope, while Table 1 summarizes the associated soil properties and engineering parameters. Prior to excavation, slope stability analyses were conducted in PLAXIS. The factor of safety was calculated as 2.255 under static conditions (Figure 1b) and 1.479 under seismic loading using pseudo-static analysis (Figure 1c).

Table 1.
Soil material and engineering properties of the model slope.

Material Model	**Drainage Condition**	γ_{unsat} **kN/m³**	γ_{sat} **kN/m³**	**Effective Elasticity Modulus, E' (kPa)**	**Effective Poisson's Ratio, ν'**	**Effective Cohesion, c' (kPa)**	**Effective Internal Friction Angle, ϕ'**	**Dilatation Angle, Ψ**	**Horizontal/Vertical Permeability Coefficient, kx,ky (m/day)**
MC	Drained	16,50	18,50	20.000	0,35	7	31°	1°	0,0001

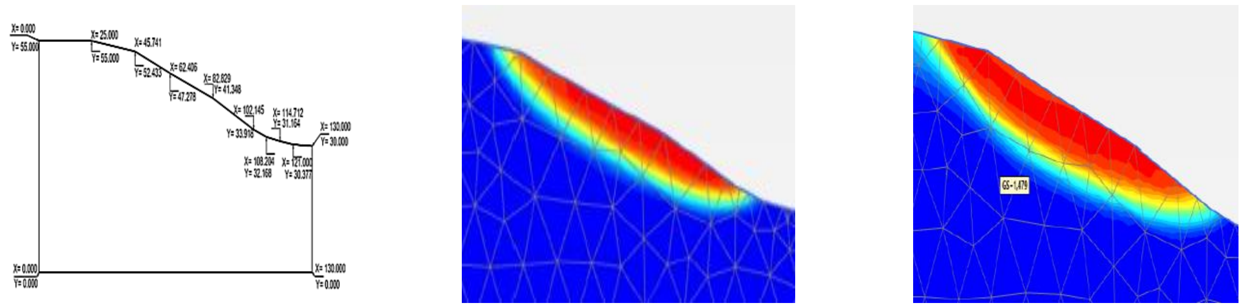

Figure 1. a. Model slope geometry and coordinates. b. Slope safety factor for static condition before excavation. c. Slope safety factor for seismic condition before excavation

In the model slope analyses, the soil profile and strength parameters were kept constant. An external load of 75 kN/m was entered for a length of 17 m starting from 5 m from the edge of the slope at the top. In order to obtain a flat area on a parcel with a sloping surface, different bearing structures were designed for the situations that occurred by advancing with 2 m gradual excavations from the two area of the model slope. The material from the excavation was used in the backfill.

3. The Research Findings and Discussion

3.1. Slope Stability Analyses and Engineering Interpretations

Slope stabilization represents a critical and complex challenge in contemporary geotechnical engineering. In particular, excavation activities in sloped terrains necessitate the use of reliable and sustainable structural systems to prevent slope failure and mitigate associated risks. Various stabilization techniques have been developed to address this issue, among which gravity retaining walls, reinforced concrete cantilever walls, and pile shoring systems are commonly employed [19], [20], [21], [22]. TBDY-2018 Stability of Slopes Under Earthquake Effects regulations 16.13.7 states that “Slope stability control under earthquake effect can be done by equivalent static limit balance analyses, finite element method or dynamic behavior analyses to be performed in the time domain”. In this study, slope analyses were performed using the pseudo-static analysis method in the Plaxis 2D software based on the finite element method.

In this study, a comprehensive slope stability analysis was conducted using a model slope subjected to six successive excavation stages. Each stage resulted in a reduction in overall stability, necessitating the implementation of appropriate retaining structures. Gravity retaining walls, reinforced concrete cantilever walls, and pile shoring systems were designed for different excavation depths, and their performance was comparatively assessed in terms of both structural stability and construction cost. In the simulations, stability was restored at each excavation depth using the aforementioned systems. These solutions were systematically evaluated to identify the most efficient method for each case. While literature provides a general guideline for pseudo-static slope stability analyses, it does not define a universally accepted value for the horizontal seismic coefficient. Based on a review of related studies [13], the horizontal coefficient (kh) is typically selected within the range of 0.10–0.20. In this study, a value of kh = 0.15g was adopted for seismic loading scenarios. Structural stability checks for gravity and cantilever walls were carried out using the İstCAD software, following the requirements of the Turkish Building Earthquake Code (TBDY-2018). These checks included sliding, overturning, and bearing capacity, along with reinforced concrete design and quantity estimations.

First of all, excavation was started by making a slope ratio of 1.65:4.10 on the model slope (Figure 2 a). It was seen that the slope safety number was 1.086 for the post-excavation situation (Figure 2b). In order to keep the slope safe, a stone wall with a base of 175 cm, a top of 100 cm wide and a height of 377 cm was modeled (Figure 2 a) and a slope analysis was performed by backfilling behind the wall (Figure 2 c). As a result of the analysis, the safety number of the slope was 1.769 for the static situation (Figure 3.7) and 1.281 for the earthquake situation (Figure 2 d). Analyses were made to ensure the stability of the slope with a reinforced concrete cantilever retaining wall for this excavation height, and it was revealed that stability could be achieved with a retaining wall with a foundation width of 200 cm, a body height of 327 cm, and a total wall height of 357 cm (Figure 3).

The model slope toe area was planned to open a flat area and continued from the same level with excavations up to 5.00 m, and its stability was disrupted due to the increasing excavation height, and the slope was made safe again by designing a stone wall and a cantilever retaining wall as a support structure that can safely hold the slope. The analyses show that the slope will be stable with a stone wall of 262 cm, a top of 125 cm wide, a height of 550 cm (Figure 4) and a reinforced concrete cantilever retaining wall with a foundation width of 350 cm, a body height of 500 cm, and a total wall height of 540 cm (Figure 5), and shoring was not needed for this height of excavation in terms of both stability and economy.

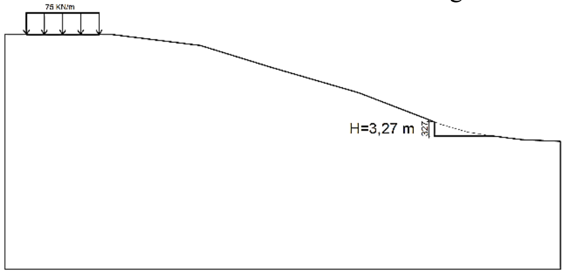

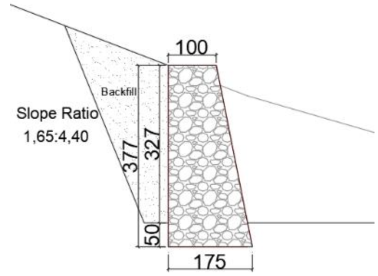

a. Section

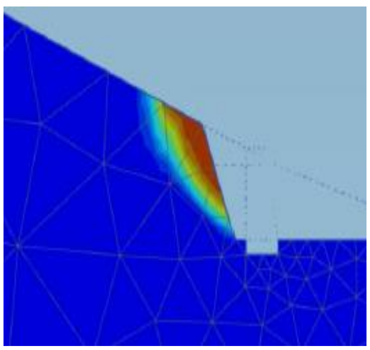

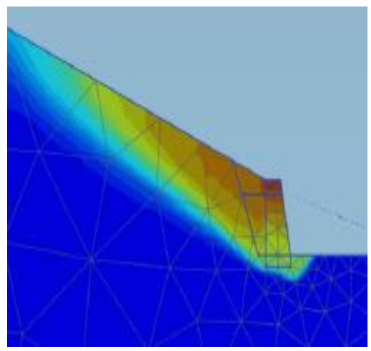

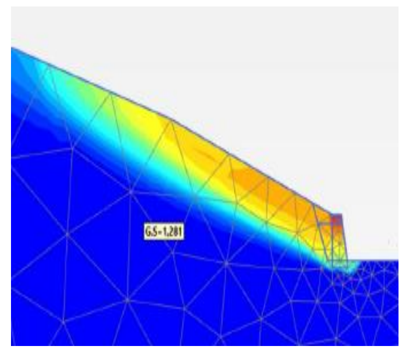

b. Slope analysis for post-excavation situation

c. H= 3.77 m Safety factor for the static case in the solution with the stone wall.

d. H= 3.77 m Safety factor for the seismic case in the solution with stone wall.

Figure 2. H= 3.77 m gravity stone wall dimensions and slope analysis results.

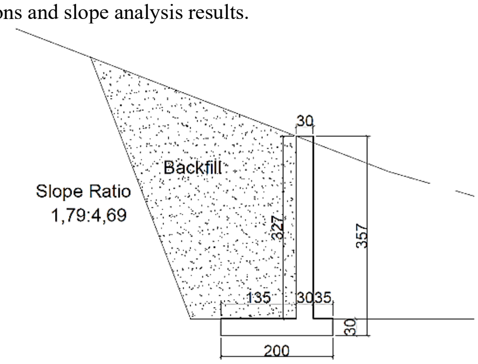

a. Section

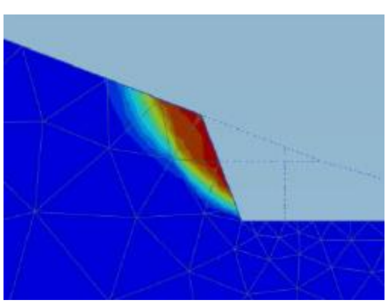

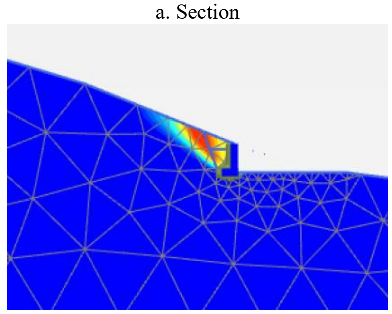

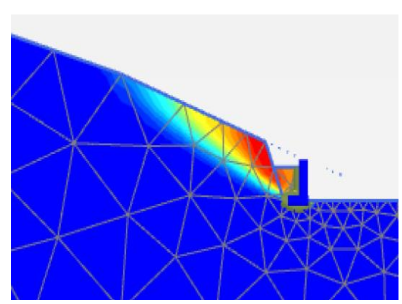

b. Slope analysis for post-excavation situation.

c. H= 3.57m Solution with cantilever retaining wall and full backfill.

d. H= 3.57m Solution with cantilever retaining wall and gradual backfill.

Figure 3. H= 3.57 m cantilever retaining wall dimensions and slope analysis results.

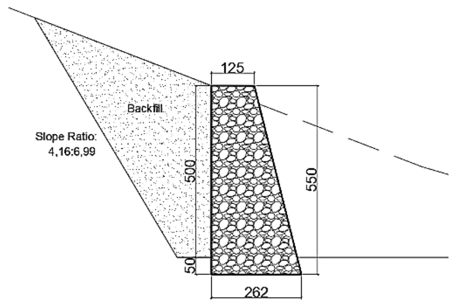

a. Section

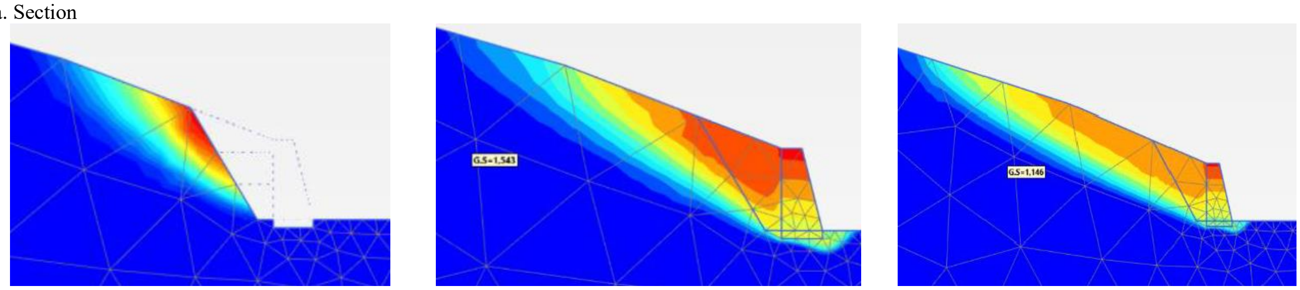

b. Slope analysis for post-excavation situation

c. Static case slope stability analysis in solution with H= 5.50 m stone wall.

d. Slope stability analysis for earthquake case in solution with H= 5.50 m stone wall.

Figure 4. H= 5.50 m gravity stone wall dimensions and slope analysis results.

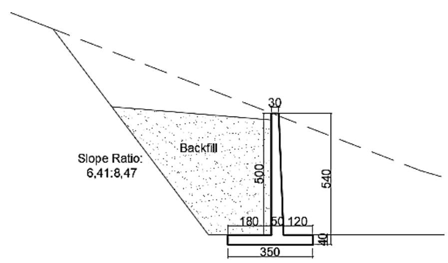

***a.** Section*

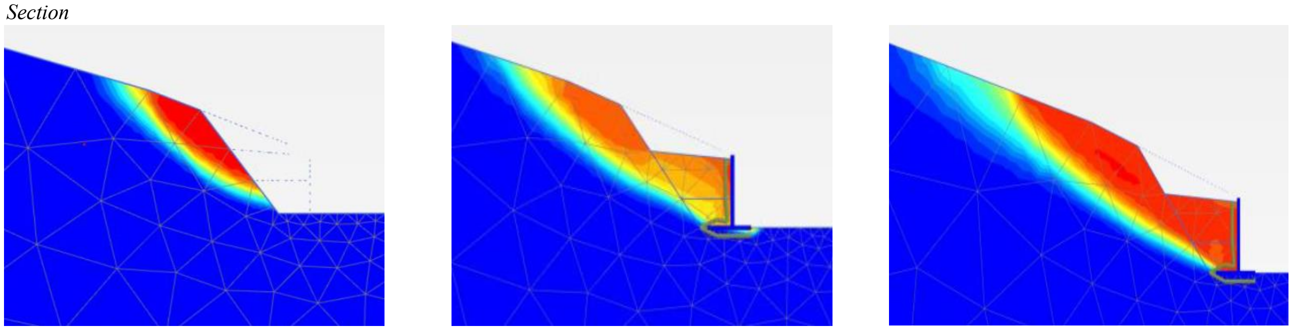

b. Slope analysis for post-excavation situation

c. Static state slope analysis in solution with H= 5.40m console wall.

d. Slope analysis of earthquake case in solution with H= 5.40 m console wall.

Figure 5. H= 5.40 m cantilever retaining wall dimensions and slope analysis results.

In order to open a flat area in the toe area of the slope, the stone wall and the console retaining wall were first examined as the support structure that could safely hold the 7.00 m vertical height with the excavations planned and continuing from the same level (Figure 6a, 7a). As seen in Figure 6a, 7a, the slope was graded with a 3.00:4.72 excavation, 2 m berm in between, and a 4.14:5.92 excavation. It was observed that the slope safety number for the post-excavation situation was 1.022 (Figure 6b, 7b). When the entire backfill was filled at the natural angle of the slope, sufficient safety could not be provided in the static and seismic situations. Sufficient stability was provided in the solution created by making a step in the backfill by adding the stability-enhancing effect of the slope stepping (Figure 6c, 6d, 7c, 7d).

In order to open a flat area in the toe area of the slope, primarily the stone wall, cantilever retaining wall and pile shoring system were examined for the problems encountered in the application with the increasing height, safety and cost comparisons as a retaining structure that can safely hold the 9.00 m vertical height with the excavations continuing from the same level (Figures 8a, 9a, 10a, 11a). It was observed that the slope safety number was 1.05 for the situation after the excavation (Figures 8b, 9b). As a result of the solutions made with the stone wall and cantilever retaining wall by grading the backfill, a sufficient safety situation was reached (8c, 8d, 9c, 9d). An evaluation was made with Ø80 cm diameter tangential pile shoring for the same height (Figure 10b), it exceeded the sufficient safety number (Figure 10c) but the maximum value of pile lateral displacement was exceeded (Figure 10d). For this reason, for the same excavation height, a solution was made again for the Ø100 cm diameter tangential pile shoring system (Figure 11a), and the lateral displacement and safety factor values in Figures 11 c and 11 d were found to be within the acceptable range.

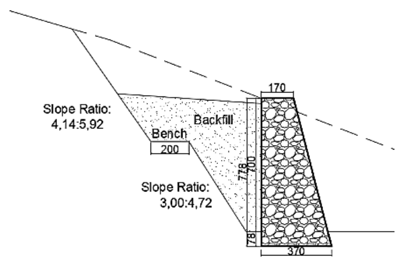

a. Section

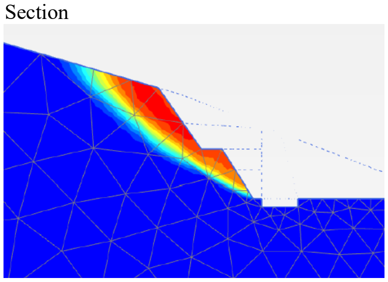

b. Slope analysis for post-excavation situation

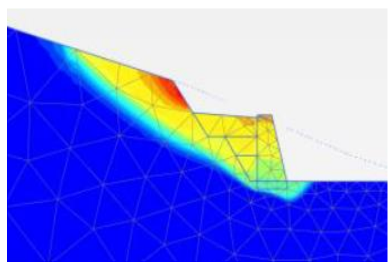

c. Static case slope stability analysis in solution with H= 7.78 m stone wall.

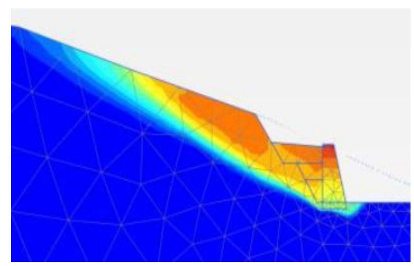

d. Slope stability analysis for earthquake case in solution with stone wall at H= 7.78 m.

Figure 6. H= 7.78 m gravity stone wall dimensions and slope analysis results.

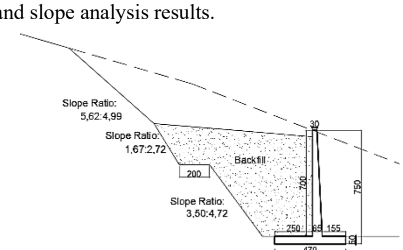

a. Section

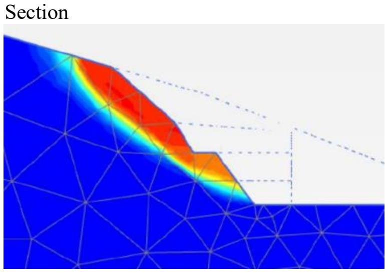

b. Slope analysis for post-excavation situation

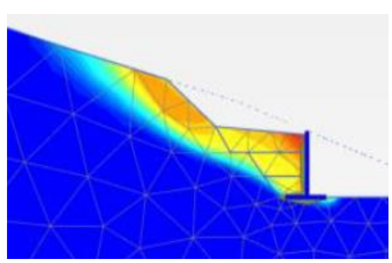

c. Static case slope analysis in solution with H= 7.50m console wall.

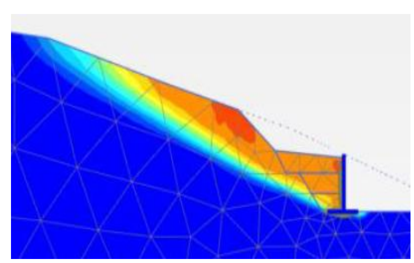

d. Seismic case slope analysis in solution with H=7,50m console wall

Figure 7. H= 7.50 m cantilever retaining wall dimensions and slope analysis results.

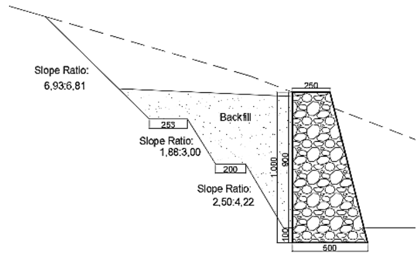

a. Section

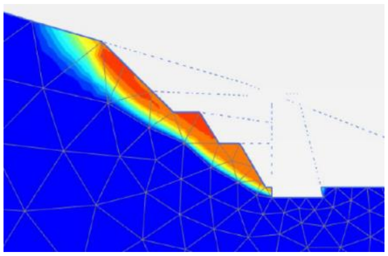

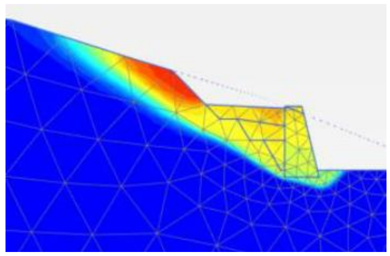

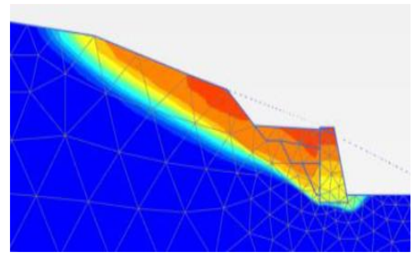

b. Slope analysis for post-excavation situation

c. Static case slope stability analysis in solution with H= 10.00 m stone wall.

d. Slope stability analysis in earthquake case with H= 10.00 m stone wall solution.

Figure 8. H= 10.00 m gravity stone wall dimensions and slope analysis results.

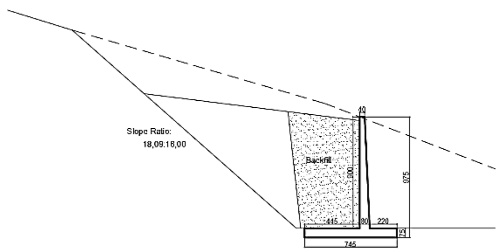

a. Section

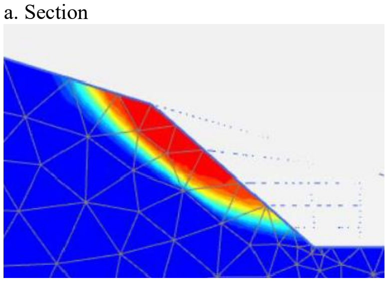

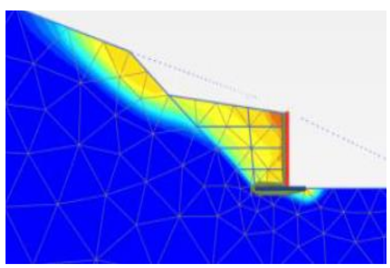

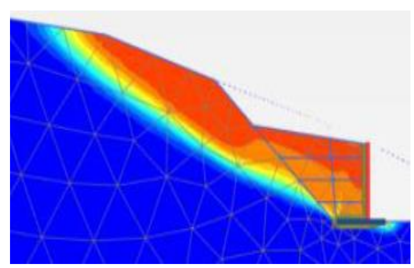

b. Slope analysis for post-excavation situation

c. Static case slope analysis in solution with H= 9.90 m console wall.

d. H= 9.90 m Seismic situation slope analysis in solution with console wall.

Figure 9. H = 9.90 m cantilever retaining wall dimensions and slope analysis results.

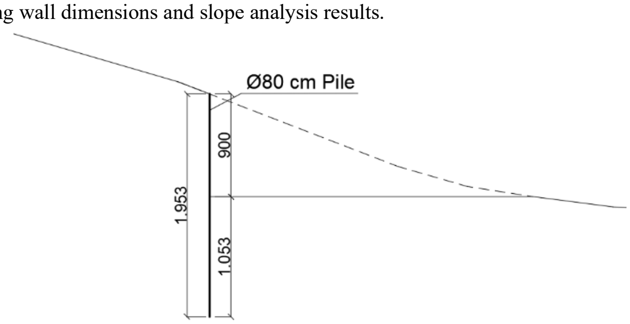

a. Section

Continued on the next page.

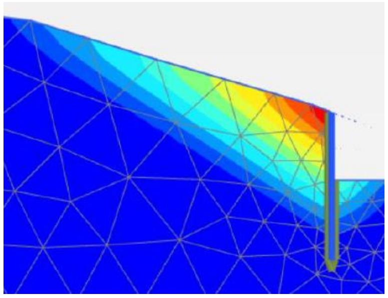

b. H= 19.50 m. Ø 80 cm tangent pile static condition slope analysis.

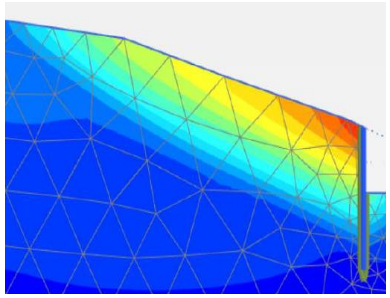

c. H= 19.50 m Ø 80 cm tangent pile earthquake case slope analysis.

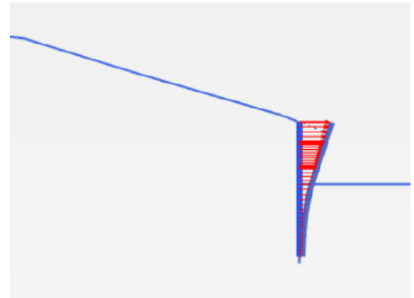

d. Lateral displacements in pile element in Plaxis software.

Figure 10. H=19.50 m Ø 80 cm tangent pile dimensions and slope analysis results.

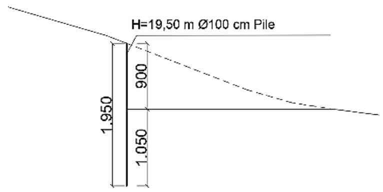

a. Section

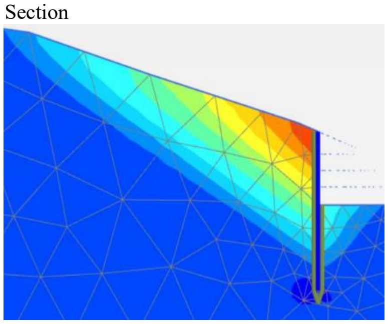

b. H= 19.50 m Ø100 cm tangent pile static condition slope analysis.

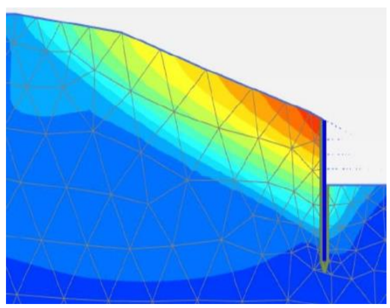

c. H= 19.50 m Ø100 cm tangent pile earthquake case slope analysis

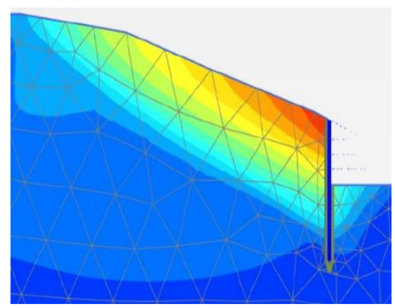

d. Figure 11. H=19.50 m Ø 100 cm tangent pile dimensions and slope analysis results.

Figure 11. H=19.50 m Ø 100 cm tangent pile dimensions and slope analysis results.

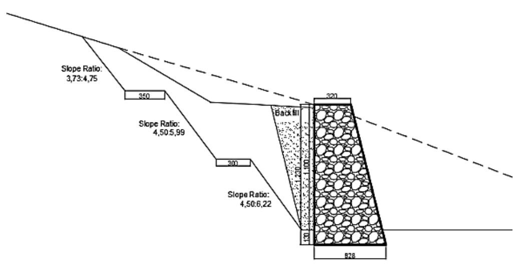

a. Section

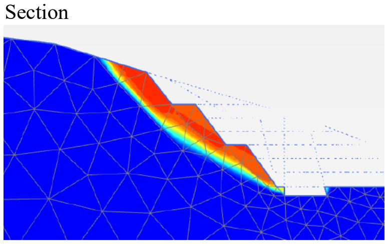

b. Slope analysis for post-excavation situation.

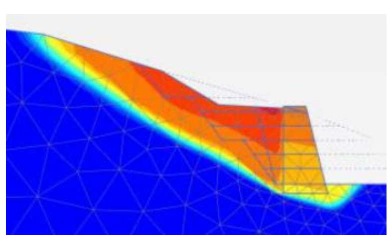

c. Static case slope stability analysis in solution with H= 12.30 m stone wall.

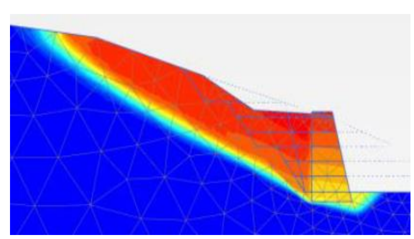

d. Slope stability analysis for earthquake case in solution with stone wall at H= 12.30 m.

Figure 12. H= 12.30 m gravity retaining wall dimensions and slope analysis results.

At the same level, the excavation depth was increased to 11 m and a solution was achieved with stone wall, console retaining wall and pile shoring system (Ø 100 cm tangential pile size) (Figures 12a, 13a, 14a, 15a). As a result of the analyses, sufficient stability could not be provided for the determined solution systems (12 b,c, 13c,d, 14 c,d). However, when the pile diameter was increased to Ø 120 cm (Figure 15b) for the same excavation height, the stability conditions were provided (Figures 15c, 15d).

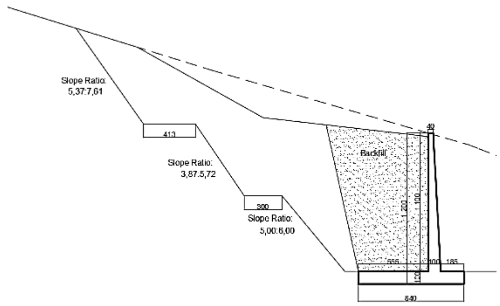

a. Section

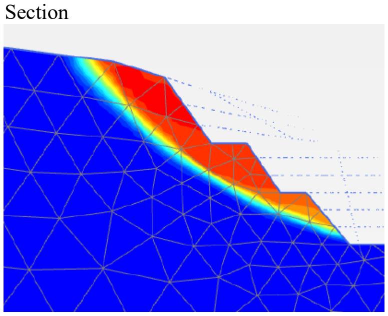

b. Slope analysis for post-excavation situation

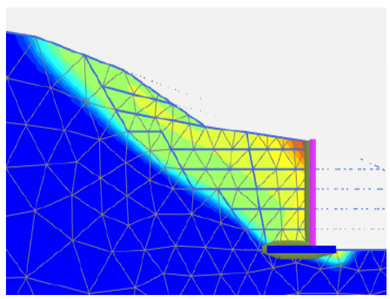

c. Static state slope analysis in solution with H= 12.00 m console wall.

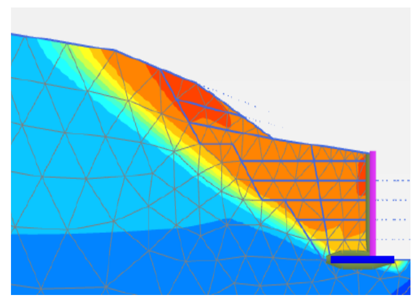

d. H= 12.00 m Seismic case slope analysis in solution with console wall.

Figure 13. H= 12.00 m cantilever retaining wall dimensions and slope analysis results.

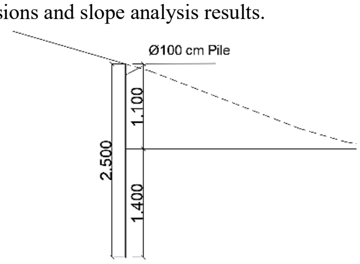

a. Section

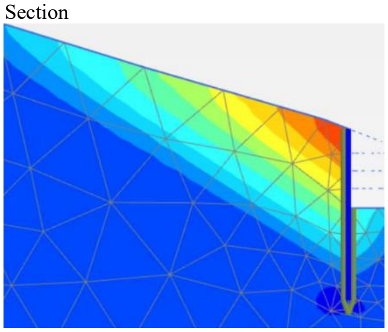

b. H= 25 m Ø100 cm Tangential pile plaxis static condition slope analysis.

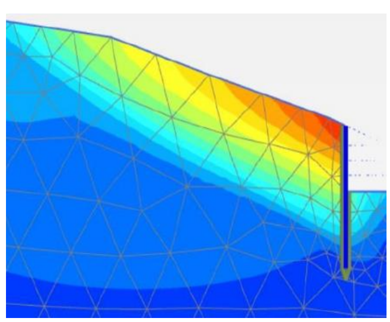

c. H= 25 m. Ø100 cm Tangential pile plaxis analysis earthquake condition slope analysis.

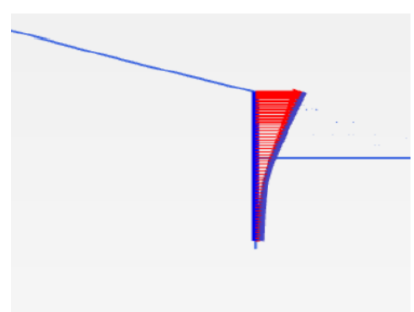

d. H= 25 m. Ø100 cm Tangential pile lateral displacements.

Figure 14. H=25.00 m Ø 100 cm tangent pile dimensions and slope analysis results.

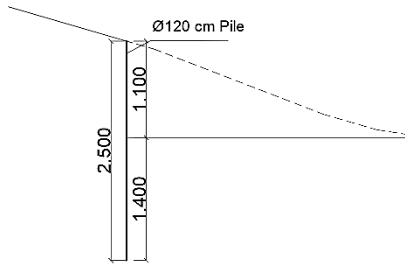

a. Section

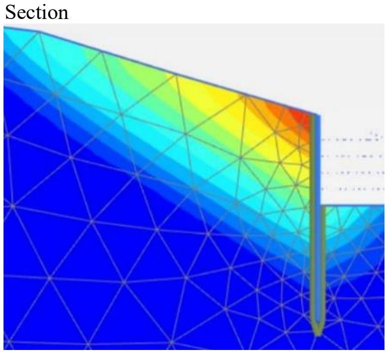

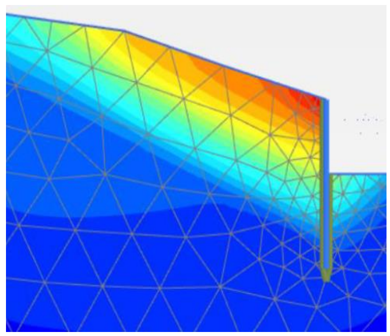

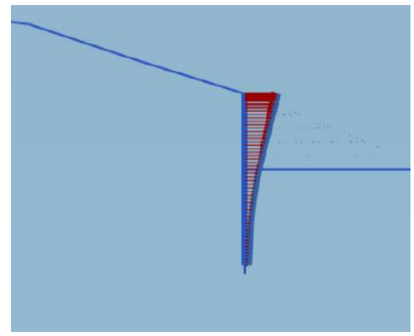

b. H= 25 m. Ø120 cm Tangential pile plaxis slope analysis for static condition.

c. H= 25 m. Ø120 cm Tangential pile plaxis slope analysis for earthquake condition.

d. H= 25 m Ø120 cm Tangential pile lateral displacements.

Figure 15. H=25.00 m Ø 120 cm tangent pile dimensions and slope analysis results.

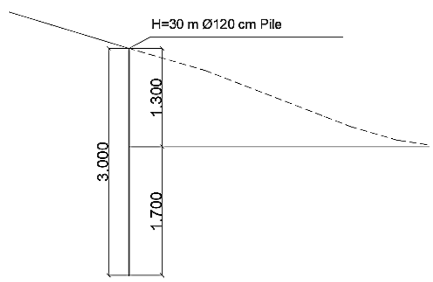

a. Section

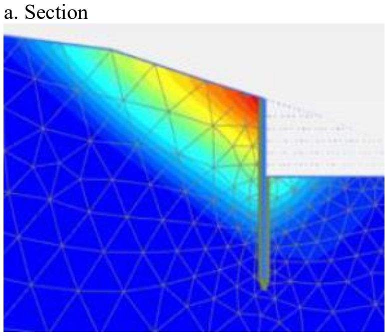

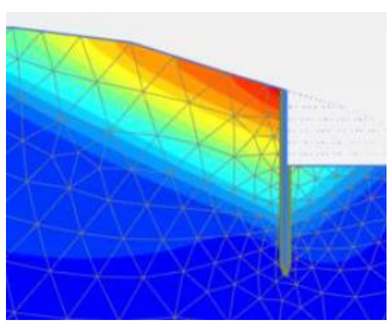

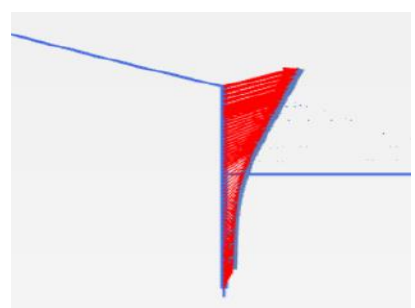

b. H= 30 m. Ø120 cm Tangential pile plaxis static condition slope analysis.

c. H= 30 m. Ø120 cm Tangential pile plaxis earthquake case slope analysis.

d. H= 30 m Ø120 cm Tangential pile lateral displacements.

Figure 16. H=30.00 m Ø 120 cm tangent pile dimensions and slope analysis results.

When the analysis was performed with the Ø120 cm diameter tangential pile shoring system (Figure 16a) as the support structure that can safely hold the vertical height of 13.00 m with the excavations continuing from the same level, the sufficient conditions could not be provided (16b, 16c, 16d). Therefore, it is necessary to examine the anchored bored pile or other prevention methods as the support structure for the excavation slope at this height.

The slope safety numbers and maximum lateral displacements of pile elements obtained from the analyses obtained from Plaxis 2D and istCAD software are given in Table 2. According to these results, it is seen that the static condition slope safety numbers are close to each other, and in the earthquake condition, the limit balance method slope safety numbers are slightly higher than the finite element method. In Project-10, while the limit balance analysis slope safety number for the Ø100 tangent pile is not sufficient for the static condition with 1.04, the safety number for the earthquake condition is a high value of 2.58. The inadequacy of the static safety number is due to the insufficient pile anchorage length in the calculation of the istCAD program. Here, the deformation calculations of the Plaxis software based on the finite element method are taken into account.

The comparison of the cost analyses of the projects is given in Table 2. When the stone and console retaining wall costs are compared; it is seen that stone walls up to 5 m in height are economical. Stone wall manufacturing is easy and fast with construction machinery. Due to their cost-effectiveness, ease of construction, and minimal technical requirements, gravity stone retaining walls are commonly preferred for slope stabilization projects involving excavation depths of up to 5 meters. Their widespread use in low-height slope applications is supported by various field investigations and numerical modeling studies, which demonstrate that such walls provide adequate stability against sliding and overturning while requiring relatively simple construction methods and materials. Furthermore, in comparison with reinforced concrete retaining structures, gravity stone walls offer faster installation, reduced labor demands, and lower material costs, particularly in rural or low-traffic areas where heavy equipment access and aesthetic integration with the environment are important considerations [23], [24]. Furthermore, even at a height of 9 meters, gravity stone walls have been found to be approximately 10% more cost-effective than cantilever retaining walls. However, despite their technical feasibility at this height, their use becomes less practical due to the significantly larger foundation footprint they require. This spatial demand often conflicts with boundary constraints in densely developed or restricted parcels, thereby limiting their application in such environments [25].

Cantilever retaining walls ranging from 5 to 9 meters in height are generally considered both cost-effective and structurally functional for moderate slope stabilization needs [26]. However, as wall height increases, construction becomes significantly more complex, leading to extended project durations and increased labor intensity [27]. Taller cantilever walls typically require dense reinforcement detailing, extensive scaffolding, and complex formwork systems to ensure structural integrity [28], [29]. Furthermore, these systems demand large-scale excavation for foundation construction, which can pose challenges in urban environments, such as permit restrictions along adjacent properties or road frontages. Excessive excavation may also compromise the stability of the slope during construction by reducing passive earth pressures and disturbing the equilibrium of the slope mass, thereby increasing the risk of localized failure. In contrast, pile-supported retaining systems do not necessitate extensive excavation, and the slope's factor of safety typically remains unaffected during installation, making them a more stable alternative for deeper cuts[29], [30].

The bored pile shoring system offers advantages such as accelerated construction timelines and ease of implementation within restricted property boundaries. However, the cost efficiency of such systems becomes a critical consideration. For instance, a Ø100 cm tangent pile with a length of 19.50 meters, designed for a 9-meter excavation depth, incurs approximately 32% higher costs compared to a 10-meter-high cantilever retaining wall. This underscores the importance of performing a cost-benefit analysis when selecting retaining systems for deep excavations [31]. At greater slope heights, specifically around 11 to 12 meters, conventional solutions such as gravity stone walls and cantilever reinforced concrete walls begin to exhibit limitations in terms of structural performance and stability. Merely increasing the wall dimensions or concrete strength is insufficient to achieve the required safety criteria. While slope stability analyses for Ø100 cm tangent piles at these depths indicate acceptable safety factors, the lateral displacement values surpass permissible thresholds [32], [33].

To address this issue, a Ø120 cm tangent pile configuration was employed. Although this system meets the required safety factor for slopes up to 13 meters, it still exhibits lateral displacements exceeding allowable limits. Even with modifications such as increased pile length and enhanced concrete quality, displacement control remains inadequate. Consequently, alternative solutions such as anchored bored pile systems or other advanced stabilization techniques should be considered for excavation slopes at this depth to ensure both structural integrity and serviceability.

4. RESULTS

According to the data obtained as a result of the two-dimensional analyses carried out within the scope of the study, the following conclusions were reached;

Slope gravity retaining walls up to 5 meters can be preferred due to their economy and easy construction. Since the manufacturing of weight retaining walls in the range of 5-9 m is difficult, cantilever retaining walls are considered more suitable in terms of cost and functionality. Using Ø100 cm tangent piles for 9 m excavation height brings 32% higher cost compared to 10 m cantilever retaining wall. While stability problems were observed in

Table 2.
Slope numbers of finite elements and limit equilibrium methods

Supporting Structure Information				Slope Safety Number				Maximum Lateral Displacement	Construction Cost (TL)	Difference Ratio (%)
Excavation Height (m)	Project No	Supporting Structure	Supporting Structure Height (m).	Finite Elements Analysis		Limit Balance Analysis -				
				Statik Situation	Pseudo Static	Statik Situation	Pseudo Static			
3,27	Project-1	Stone Wall	3,77	1,769	1,281	1,76	1,62	---	139.925,15	34,26%
	Project-2	Cantilever Retaining	3,57	1,615	1,188	1,84	1,66	---	187.869,47	
5	Project-3	Stone Wall	5,5	1,54	1,142	1,63	1,44	---	283.558,80	33,13%
	Project-4	Cantilever Retaining	5,4	1,541	1,107	1,65	1,48	---	377.499,55	
7	Project-5	Stone Wall	7,78	1,554	1,124	1,58	1,44	---	609.041,78	12,09%
	Project-6	Cantilever Retaining	7,5	1,513	1,107	1,55	1,36	---	682.656,33	
9	Project-7	Stone Wall	10	1,606	1,14	1,63	1,46	---	1.148.363,60	10,31%
	Project-8	Cantilever Retaining	9,9	1,512	1,1	1,67	1,46	---	1.266.705,57	
	Project-9	Ø80 Tangent Pile	19,5	1,507	1,173	2,77	2,32	94	---	
	Project-10	Ø100 Tangent Pile	19,5	1,515	1,183	1,04	2,58	76,68	1.677.304,59	
11	Project-11	Stone Wall	12,3	1,526	1,092	1,53	1,35	---		32,41%
	Project-12	Cantilever Retaining	12	1,379	1,01	1,59	1,37	---	---	
	Project-13	Ø100 Tangent Pile	25	1,536	1,195	---	---	132,6	---	
	Project-14	Ø120 Tangent Pile	25	1,536	1,192	3,03	2,49	10,51	2.288.559,50	
13	Project-15	Ø120 Tangent Pile	30	1,526	1,205	---	---	193,8	---	

stone and cantilever retaining walls with a height of 11-12 meters, the use of Ø100 cm tangent piles was insufficient in terms of lateral displacement and in this case, Ø120 cm diameter piles were applied as a solution. Even for 13 meters height, the lateral displacement of Ø120 cm cantilever piles remained above the limit values and it became necessary to evaluate alternative stability measures such as anchored bored piles at this height. In this context, it is of great importance to select the optimum bearing structure by considering stability, cost and construction difficulties for each slope height.

Within the scope of the excavation works, stone wall, cantilever retaining wall and pile retaining systems were analyzed for different excavation depths and slope slopes. While stone wall and cantilever retaining wall solutions provided sufficient stability in the first stages, pile retaining systems were needed in terms of slope safety with the increase in excavation depth. Stability was provided with stone wall for excavations up to 5.00 m, and for excavations up to 7.00 m, the excavation was graded and the safety factor was brought to acceptable levels with the combination of stone wall and cantilever retaining wall. As a result of the analyses made with stone wall and retaining wall for the excavation height of 9.00 m, it was seen that stability could be provided. However, in the analyses made at the excavation depth of 11 m, it was determined that the stone wall and retaining wall solutions were insufficient and the pile retaining system was switched to. In the solution made with Ø100 cm diameter piles, the lateral displacement limit values 32% were exceeded, therefore it was determined that the stability conditions were provided with Ø120 cm diameter piles. However, it was observed that sufficient stability conditions could not be provided in the analyses made with the Ø120 cm diameter tangential pile shoring system as a support structure that could safely hold the 13.00 m vertical height with the excavations continuing from the same level. Therefore, it was revealed that anchored bored pile systems or other prevention methods should be examined for the excavation slope at this height. As a result, it was determined that stone wall and retaining wall solutions were sufficient for certain excavation depths, but in case of exceeding certain limits, it was necessary to switch to pile shoring system and to anchored pile systems at greater depths, and the most suitable engineering solution was presented by taking into account safety and economic factors.

References

[1] Anaç, İ. and A. Şirin. "Landslide Identification and Data Generation Guide." Ankara (2015).

[2] Seçkin, F. and G. Tolga. "Distribution characteristics of fatal landslides in Türkiye and determination of priority areas at national scale." Turkish Geography Journal 74 (2020): 123–134. https://doi.org/10.17211/tcd.731596

[3] Şahan, C. "A research on natural disasters in Turkey." Ordu University Social Sciences Institute Social Sciences Research Journal 14.2 (2024): 414–428. https://doi.org/10.48146/ODUSOBIAD.1176360

[4] Matpay, B. and S. Mutlu. "Determining the Natural Disaster Diversity of Van Province by Fine Kinney Risk Assessment Method (FK-RAM)." Coruh University Natural Disasters Application and Research Center Natural Disasters and Environment Journal 9.2 (2023): 324–340. https://doi.org/10.21324/dacd.1295546

[5] Öz, T. and H. Günek. "Landslide Susceptibility and Settlement Risk Analysis of Solakli Basin (Trabzon)." International Journal of Geography and Geography Education 44 (2021): 396–412. https://doi.org/10.32003/igge.931516

[6] Şahin, Ş. "The Disaster Management in Turkey and Goals of 2023." Turkish Earthquake Research Journal 1.2 (2019): 180–196.

[7] Ausilio, E., E. Conte, and G. Dente. "Stability analysis of slopes reinforced with piles." Computers and Geotechnics (2001): 591–611.

[8] Li, X., S. He, and C. Wang. "Stability analysis of slopes reinforced with piles using limit analysis method." Proceedings of Geo-Shanghai International Conference (2006): 105–112. https://doi.org/10.1061/40863(195)8

[9] Ashour, M. and A. Hamed. "Analysis of pile stabilized slopes based on soil–pile interaction." Computers and Geotechnics 39 (2012): 85–97.

[10] Cai, F. and K. Ugai. "Numerical analysis of the stability of a slope reinforced with piles." Soils and Foundations 40 (2000): 73–84.

[11] Lei, H., X. Liu, Y. Song, and Y. Xu. "Stability analysis of slope reinforced by double-row stabilizing piles with different locations." Natural Hazards 106.1 (2021): 19–42. https://doi.org/10.1007/s11069-020-04446-2

[12] Griffiths, D. V. and R. M. Marquez. "Three-dimensional slope stability analysis by elasto-plastic finite elements." Geotechnique 57.6 (2007): 537–546. https://doi.org/10.1680/geot.2007.57.6.537

[13] Mujah, D., A. F. I. H. Hazarika, A. S. A. Rashid, N. H. M. Nor, and S. N. L. Taib. "The Design Method of Slope Stabilizing Piles: A Review." International Journal of Civil Engineering and Technology 3.2 (2013).

[14] Du, C., J. Chen, S. Chen, M. Peng, and Z. Shi. "Numerical analysis of a slope stabilized with piles and anchor cable frame beams." Environmental Earth Sciences 82.4 (2023): 100. https://doi.org/10.1007/s12665-023-10784-8

[15] Vaughan, P. R. "Three-dimensional slope stability analysis by elasto-plastic finite elements." Geotechnique 58.8 (2008): 683–685. https://doi.org/10.1680/geot.2008.D.010

[16] Cheng, X., Y. Zhang, Y. Zhang, Y. Zhao, and S. Wang. "Different aspects regarding slope stability improvement using piles." IOP Conference Series: Materials Science and Engineering 1304.1 (2024). https://doi.org/10.1088/1757-899x/1304/1/012009

[17] Wei, W. B. and C. Yung Ming. "Strength reduction analysis for slope reinforced with one row of piles." Computers and Geotechnics 36.7 (2009): 1176–1185.

[18] Jiang, J. H., X. L. Huang, X. R. Shu, X. Ning, Y. Qu, and W. L. Xiong. "Application of a damage constitutive model to pile–slope stability analysis." Frontiers in Materials 9 (2022). https://doi.org/10.3389/fmats.2022.1082292

[19] Yumrutaş, H. İ., İ. Keskin, and U. Aydın. "Comparative Analysis of Geosynthetic Reinforced Earth Wall and Reinforced Concrete Retaining Wall: Kastamonu-Karabuk Highway Case Study." Bilecik Şeyh Edebali Üniversitesi Fen Bilimleri Dergisi 9.1 (2022): 225–240.

[20] Yilmaz, I., T. Ekemen, M. Yildirim, I. Keskin, and G. Özdemir. "Failure and flow development of a collapse induced complex landslide: The 2005 Kuzulu (Koyulhisar, Turkey) landslide hazard." Environmental Geology 49.3 (2006): 467–476. https://doi.org/10.1007/s00254-005-0113-0

[21] Keskin, İ., F. Karataş, and S. Kahraman. "Investigation of The Effects of Earthquake Characteristics on Slope Stability Using Model Slope." Uludağ Üniversitesi Mühendislik Fakültesi Dergisi 27.2 (2022): 785–802. https://doi.org/10.17482/uumfd.1098502

[22] Öztürk, E. H. and Türkeli. "Optimum design of RC Retaining walls with key section using jaya algorithm." Journal Of Polytechnic-Politeknik Dergisi (2019). https://doi.org/10.2339/politeknik.432031

[23] Varga, R., B. Žlender, and P. Jelušič. "Multiparametric analysis of a gravity retaining wall." Applied Sciences (Switzerland) 11.13 (2021). https://doi.org/10.3390/app11136233

[24] Shah, D. J. "Stability Analysis of Gravity Retaining Wall by DEM Simulation." ESP International Journal of Advancements in Science & Technology (ESP-IJAST) 2.4 (2024): 1–5. https://doi.org/10.56472/25839233/ijast-v2i4p101

[25] Varga, R., B. Žlender, and P. Jelušič. "Optimization of Embedded Retaining Walls Under the Effects of Groundwater Seepage Using a Reliability-Based and Partial Factor Design Approach." Applied Sciences 14.23 (2024): 11135. https://doi.org/10.3390/app142311135

[26] Bari, F., J. A. Repadi, Andriani, F. A. Ismail, and A. Hakam. "Optimal Cost of Slope Stabilization With Retaining Wall." Geomate Journal 22.93 (2022): 83–90. https://doi.org/10.21660/2022.93.3129

[27] Ma, X., Y. Liu, Z. Hao, X. Wang, and Y. Yang. "Study on stress and deformation characteristics of existing-new two-stage cantilever retaining wall." PLoS One 19.2 (2024): e0296330. https://doi.org/10.1371/journal.pone.0296330

[28] Tierney, L. and M. Safiuddin. "Insights into Concrete Forming, Reinforcing, and Pouring in Building Construction." Buildings 12.9 (2022): 1303. https://doi.org/10.3390/buildings12091303

[29] Mohammad, F. A. and H. G. Ahmed. "Optimum Design of Reinforced Concrete Cantilever Retaining Walls according Eurocode 2 (EC2)." Athens Journal of Technology and Engineering 5 (2018): 253–277. https://doi.org/10.30958/ajte.5-3-4

[30] Tornborg, J., M. Karlsson, and M. Karstunen. "Permanent Sheet Pile Wall in Soft Sensitive Clay." Journal of Geotechnical and Geoenvironmental Engineering 149.6 (2023). https://doi.org/10.1061/jggefk.gteng-10955

[31] Yost, K. M., A. Yerro, R. A. Green, E. Martin, and J. Cooper. "MPM Modeling of Cone Penetrometer Testing for Multiple Thin-Layer Effects in Complex Soil Stratigraphy." Journal of Geotechnical and Geoenvironmental Engineering 148.2 (2021): 04021189. https://doi.org/10.1061/(asce)gt.1943-5606.0002730
[32] Pham, T., A. Palma, T. Nguyen, and T. Vu. "Investigating Lateral Displacement of Pile Groups under Construction Loads and Excavation—A Case Study." (2022): 1–14. https://doi.org/10.1061/9780784484029.001
[33] Zhang, C., L. Su, W. Chen, and G. Jiang. "Full-scale performance testing of bored piles with retaining walls in high cutting slope." Transportation Geotechnics 29 (2021). https://doi.org/10.1016/j.trgeo.2021.100563

J-Researchers

Journal of Civil Engineering Researchers

Journal homepage: www.journals-researchers.com

The Effect of Employing a Thermal Insulation Layer in the Building Façade on Energy Consumption (A case study of a residential building in Tehran)

Amir Sina Darabi,[a,*] Mehdi Ravanshadnia[a]

[a] *Department of Civil Engineering, Science and Research Branch، Islamic Azad university، Tehran, Iran*

ABSTRACT

Although currently, a large part of the existing buildings are considered inefficient in terms of energy, the ability to save energy consumption up to 80% has been proven in residential and commercial buildings. This study aims to calculate energy consumption during the operational phase caused by various scenarios of thermal insulation combinations in a building's exterior shell. The simulation was conducted using Design Builder software, with a five-story residential building in Tehran as the case study. Initially, the building was modeled in Design Builder, and keeping all other characteristics constant, ten scenarios were defined: nine using different types of thermal insulation and one without insulation. The software outputs for each scenario were analyzed. Results showed that the best thermal insulation layer is polyurethane foam, which saves 1070.15 kilowatt-hours of energy during one year of the building's operation. This article can help designers and construction engineers optimize the energy consumption of buildings by deciding the right materials.

ARTICLE INFO

Received: April 10, 2025
Accepted: August 20, 2025

Keywords:
Energy Consumption
Design Builder Software
Façade
Thermal Insulation
Residential Building

DOI: 10.66224/JCER.7.3.29
DOR: 20.1001.1.2538516.2025.7.3.3.3

1. Introduction

According to the "Our World in Data" website, more than 73% of global greenhouse gas emissions stem from energy consumption, with 19% originating from the construction and building sector. This significant level of energy usage in buildings plays a crucial role in global warming. However, the silver lining is the considerable potential within this industry to reduce carbon emissions. The collaboration and optimal performance of engineers and architects in reducing energy consumption throughout the entire lifecycle of a building hold national and international importance in achieving sustainable and low-carbon buildings (www.ourworldindata.org).

In the coming decades, energy costs for heating, cooling, and lighting in homes and organizations, as well as driving industrial production processes, are expected to rise significantly. In the competitive global landscape of energy efficiency and production, countries that succeed in researching and implementing energy-saving solutions will

[*] Corresponding author. Tel.: + 989122264618; e-mail: amirsina.darabi@srbiau.ac.ir.

come out ahead. One key approach to tackling this challenge is reducing energy consumption.

Today, one of the most impactful environmental concerns is the construction of buildings. Processes such as manufacturing building materials, transporting, and installing them use significant energy resources and emit large quantities of greenhouse gases. Additionally, during the operational phase of a building, these materials contribute to varying degrees of energy loss. The increasing global energy consumption raises concerns about future energy supply. Furthermore, reducing energy use leads to lower greenhouse gas emissions, such as carbon dioxide. According to the 2020 World Energy Outlook Report, approximately 55% of energy consumption occurs in buildings. Therefore, any measures to reduce this consumption can have substantial impacts.

The depletion of fossil fuel resources, global warming, industrialization, and population growth pose challenges for the energy sector [1]. Moreover, rising energy consumption contributed to 30% of annual greenhouse gas emissions worldwide in 2013 [2]. In Iran, with a population of around 85 million, energy consumption is comparable to that of a country with a billion inhabitants. The building sector accounts for the highest energy loss, making Iran one of the world's top energy consumers. Statistics reveal that energy consumption in the building sector alone is reported to be two to four times higher than global standards. Given these circumstances, if energy consumption patterns in the residential and commercial sectors are not modified, energy use in these areas is projected to surpass 1,400 million barrels of crude oil by 2031. This not only hinders the achievement of the 20-year vision goals, but also negatively impacts Iran's oil export position and puts pressure on the economy and environment. Continuing this trend could result in serious economic crises alongside environmental consequences [3].

2. Significance of the study

Global energy consumption, although showing temporary declines in certain years, has generally trended upwards and reached 172,119 trillion watt-hours in 2023. In Iran, energy consumption in 2023 was recorded at 3,531 trillion watt-hours. This trend is depicted in Figure 1. When this level of energy consumption is divided by the population, Iran's critical situation becomes clearer.

The average global energy consumption per person is 21,394 kilowatt-hours, whereas in Asia, this figure reduces to 19,239 kilowatt-hours. However, the average energy consumption per person in Iran is 39,599 kilowatt-hours, as illustrated in Figure 2.

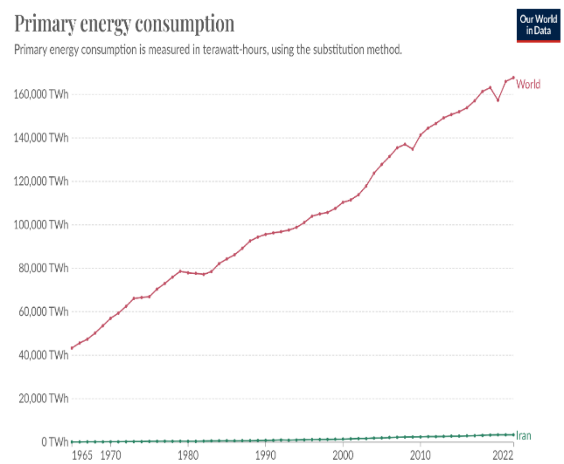

Fig. 1. the energy consumption trends in Iran and the world.

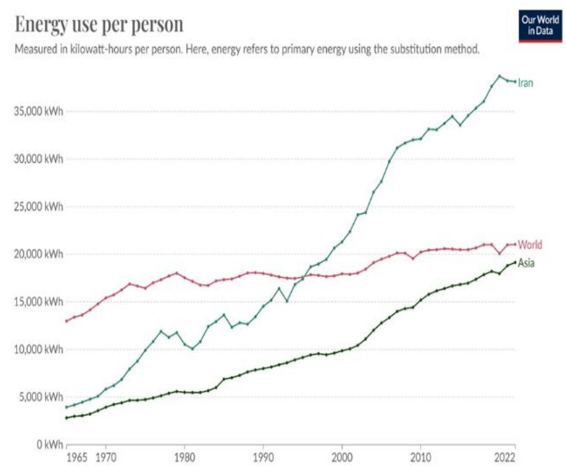

Fig. 2. the energy consumption per capita in Iran, Asia and the world.

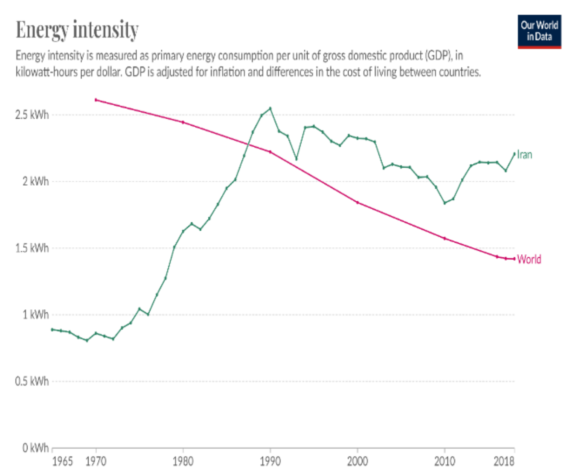

Fig. 3. the energy intensity in Iran and the world

Energy intensity is measured as primary energy consumption per unit of Gross Domestic Product (GDP) in kilowatt-hours per dollar. GDP is adjusted for inflation and differences in living costs between countries. In 2022, the global average energy intensity was 1.3 kilowatt-hours, while in Iran it was 2.21 kilowatt-hours. This is demonstrated in Figure 3.

3. Literature Review

In 2024, Soltani and Atashi conducted a study titled "The Impact of a Second Skin Facade on the Life Cycle Energy Consumption of Office Buildings: A Comparative Study." They examined the use of a second facade as a mechanism to reduce energy consumption in an office building. Their research involved modeling, simulation, and analyzing an optimized second facade's impact on both operational energy consumption and the building's life cycle energy. They found that the second skin facade reduces both operational and life cycle energy consumption. However, life cycle energy temporarily increased in the building's initial years but decreased by 30% by the 30th year compared to the baseline scenario [4].

Feehan et al. (2021) explored the optimization of facades and fenestration in their study titled "Adopting an Integrated Building Energy Simulation and Life Cycle Assessment Framework for Optimizing Facades and Fenestration in Building Envelopes." They used an integrated framework to select sustainable facade systems and windows for nearly zero-energy buildings. Results indicated that enhanced glazing reduced operational energy demand by 8.3%, though embodied energy increased by 10%, with a payback period of approximately 6–7 months. The optimal window-to-wall ratio for heating and cooling performance was 0.2, achieving an overall energy reduction of 2%. Insulated cavity walls exhibited the lowest embodied energy, while lightweight steel walls with brick facades had the highest [5].

Ousta Oghlu et al. (2021) conducted research titled "Investigation of Environmentally Friendly New Building Materials with Enhanced Energy Performance in Different Climatic Zones: Cost-Effective, Low-Energy, and Low-Carbon Emission." They used various additives such as pumice, expanded vermiculite, fly ash, and sludge to produce fired clay bricks and lightweight foamed concrete. For instance, instead of commercially available insulation materials, they utilized lightweight concrete containing expanded vermiculite, and instead of conventional bricks, they employed a new type of fired clay brick. Finally, they calculated the annual energy savings and annual cost savings for different thicknesses of bricks and lightweight concrete and computed the greenhouse gas emissions from various fuels (coal, electricity, fuel oil, liquefied petroleum gas, and natural gas). The results indicated that using these new building materials resulted in energy savings of 11 kWh/m² in an insulated building and 31.2 kWh/m² in an uninsulated building. The annual energy savings rate reached 21.7%. The highest energy savings were observed in buildings using electricity for heating. The highest carbon emissions occurred with coal. Natural gas was the cleanest heating method. Electricity generated the highest carbon emissions after coal in the studied region. A reduction in carbon emissions for coal reached 18.7 kg/year. Using these new materials, the maximum reduction in carbon emissions reached 22% [6].

Pedroso et al. (2020) conducted a study titled "Characteristics of a Multilayer External Wall Thermal Insulation System for Mediterranean Climates." This research compares the performance of a multilayer thermal insulation system with a super-insulator under Mediterranean climatic conditions. A series of mechanical, physical, and microstructural tests were performed on the insulators. The results show improved mechanical performance and water resistance when protective layers are applied in a multilayer system. When compared to other multilayer products currently on the market, this new solution offers competitive results, demonstrating improved performance under real operating conditions [7].

Mahmoud et al. (2020) conducted a study titled "Comparative Energy Performance Simulation for Passive and Conventional Designs." Their case study was an office building in Cairo, Egypt. They performed simulations using Design Builder software and weather data generated by the Meteonorm site. Their proposed passive design features included a courtyard, double-skin façade walls, overhangs, and a cross-ventilation system. Their results showed that the passive design resulted in an 11% reduction in annual energy consumption compared to the baseline conventional design [8].

Navayi et al. (1402) conducted a study titled "The Effect of Using Air Gaps in Walls on Reducing Energy Consumption in a Residential Building." To investigate the impact of air gaps in walls on energy reduction, they analysed three different air gap thicknesses (1, 2.5, and 5 cm). The energy simulation results for these three walls compared to the baseline wall show that using an air gap reduced overall energy consumption and heating and cooling loads in different months of the year. Specifically, the monthly cooling load in the hottest month decreased by 10.3%, 12.8%, and 14%, respectively, while the monthly heating load in the coldest month decreased by 32.8%, 42.3%, and 48.2%, respectively. Annual heating energy consumption decreased by 25.7%, 30.9%, and 33.6%, respectively, and annual cooling energy consumption decreased by 8.3%, 10%, and 10.9%, respectively—a significant percentage considering the building's high annual cooling energy consumption [3].

Mirsaeidi and Mirrasheed (2020) in their research titled "Investigation of the Impact of Trombe Wall System on Thermal Comfort in a Moderate and Humid Climate (Case Study: Residential Building in Gonbad-e Kavus)" examined the effect of using a Trombe wall system on indoor air temperature in a residential building in Gonbad-e Kavus under both heating and cooling conditions using Design Builder software. The simulation results showed that the Trombe wall system can be beneficial for heating in the studied climate; however, it plays a less significant role in improving cooling conditions. Further studies are needed to investigate the role of this system in reducing energy consumption, considering economic and technical aspects [9].

Fathelian and Kargar (2020), in their research titled "Investigating the Impact of Various Energy Optimization Strategies on Building Energy Rating Using Design Builder Software (Case Study: Office Building),", examined the effect of different wall configurations in double-skin facades using Design Builder software. The results showed that changing the number of inner layers in the double-skin facade is more effective in reducing energy consumption, while changing the number of outer layers has no significant effect. Greater solar radiation on the south facade makes the use of a double-skin facade more effective on this side. The study also examined the effects of employing external horizontal shading and removing internal shading, replacing single-pane windows with low-emissivity double-pane windows, and installing a thermal insulation sheet on the exterior wall, resulting in energy consumption reductions of 2.15%, 4.18%, and 2.08% respectively, compared to the conventional case [10].

4. Theoretical foundations of the research

4.1. Governing equations

Heat transfer occurs through conduction, convection, air exchange, and radiation. Proper insulation is essential to reduce heat transfer. Adding insulation decreases the heat transfer value or increases thermal resistance. Proper placement of insulation also plays a crucial role.

4.2. Heat Insulation

A composite material or system that effectively reduces heat transfer from one environment to another. In some cases, in addition to reducing heat transfer, heat insulation can also have other abilities such as load bearing, soundproofing, etc. Under special weather conditions, it can also be considered heat insulation. Thermal insulation that can be used in the building refers to insulation that has a thermal conductivity coefficient less than or equal to 0.065 watts per meter degree Kelvin and a thermal resistance equal to or greater than 0.5 watts per meter degree Kelvin. The mentioned values are related to measurements in standard thermal conditions. Thermal insulation is done by a special material or materials or by a system with several functions. For example, a load-bearing wall can provide the role of thermal insulation at the same time. But in most cases, it is necessary to add a special layer to the wall as heat insulation.

The best practices for insulation include the following:

- Applying insulation to all exterior building components (roof, external walls, and floor).
- Installing firm and secure insulation layers on walls.
- Ensuring complete waterproofing of all cavities.

4.3. Equations Governing Building Envelopes

To assess thermal comfort in a space, we first need to calculate the indoor air temperature and surface temperatures. We write the energy balance equation for each surface. Let's denote the properties related to each surface with a subscript (i):

The radiative and convective heat transfer Shown in equation 1:

$$hiAi\,(Tair\ -\ Ti) +\ \varepsilon i\sigma Ai\,\{\sum_{k=1}^{n} Fi - k\,(Tk^{\,4}Ti^{\,4})\} = Qi \tag{1}$$

The first term on the left represents heat transfer by convection between the inner wall surface and room air.

The second term represents received heat transfer through radiation from other surfaces.

The equation for heat transfer from the surface is given by equation 2.

$$Qi\ =\ Qc(i)\ -\ Qr - in(i)\ -\ Qr - out(i) \tag{2}$$

Qi represents the heat generated within the system (e.g., in a building).

$Qc(i)$ represents heat generated by internal sources (e.g., heating, cooling).

$Qr - in(i)$ represents heat transferred from the system to the external environment (e.g., through windows or other surfaces).

(Qr-out(i)) represents heat transferred from the system to other building components (e.g., walls or roof).

$Qr{-}in(i)$ includes two terms of direct sunlight ($Qr{-}direct(i)$) and scattered sunlight ($Qr{-}diffuse(i)$), where Aw is the area of the window and $As(i)$ is the area of the sun shining on surface i AST is the total area of the sun irradiated on the inner surface、$FW{-}I$ is the shape factor of the window to surface I. $Q"direct$ is the radiant heat entering from the window caused by direct sunlight per unit area and $Q"diffuse$ is the radiant heat entering from the window caused by scattered sunlight per unit area. The sum of $Q"direct$ and $Q"diffuse$ represents the total radiant energy of the sun per unit area of the window and is displayed as below.

The total solar radiation entering through the window is given by equation 3.

$$Q"s = Q"diffuse + Q"direct \quad (3)$$

In the equations of radiation from the window, the direct radiation is assumed to be negligible; therefore, only scattered radiation enters the room. $Qr{-}out(i)$ is also the heat radiation of the sun on the outer surface of the outer wall and is obtained according to the following relationship: In the calculations for the internal levels of the building, ، $Qr{-}out(i)$ is considered equal to zero.

The equation for calculating the external surfaces of the building is Shown in equation 4.

$$Qr - out(i) = Q"s.Ai \quad (4)$$

In addition to the internal surfaces, an equation must be written for the air as well.

The calculation equation for the internal levels of the building is Shown in equation 5.

$$minf\ .Cp, air(Tair - Tinf) = \sum_{i=1}^{N} hiAi\ (Ti - Tair) \quad (5)$$

where $minf$ and $Tinf$ are the mass flow rate and the temperature of the air entering the building, respectively.

Convection and transfer of heat are shown in equation 6.

$$Q = h * A * \Delta T \quad (6)$$

(Q) heat transfer rate (Watts)
(h) heat convection coefficient (watts per meter degrees Kelvin or Celsius)
(A) Cross-sectional area (square meters)
(ΔT) temperature change (Kelvin or Celsius)

The equation of conduction mechanisms is shown in equation 7.

$$Q = k * A * (\Delta T / d) \quad (7)$$

(Q) heat transfer rate (watts)
(k) coefficient of thermal conductivity (watts per meter per degree Kelvin)
(A) Cross-sectional area (square meters)
(ΔT) temperature change (Kelvin or Celsius)
(d) Thickness of the object (meters)

The next step, after calculating the air temperature and the temperature of the interior surfaces of the room, is to calculate the average thermal sensation of the room's occupants. For this purpose, the Finger model has been used. In the Finger model, there are seven important and effective parameters for thermal comfort, which are:

1. Metabolic rate
2. Amount of clothes
3. The amount of activity
4. Dry temperature
5. Average radiation temperature
6. Air flow speed
7. Relative humidity

The first three parameters are related to human factors, and the other four parameters are environmental factors. Finger has presented a relation that expresses the mentioned seven parameters in the form of one parameter.

Metabolic rate equation given by equation 8.

$$PMV = (0.303e^{-0.036M} + 0.028)(M - W) - 3.05 \times \{10\}^{\{-3\}[5733 - 6.99(M - W) - Pa\,]} - 0.42[(M - W) - 58.15] - 1.7 \times\{10\}\text{^}\{-5\} \times M(5867 - Pa\,) - 0.0014M(34 - Ta\,) - 3.96 \times \{10\}\text{^}\{-8\} \times Fci\,[((tci + \{273\}\text{^}4) - \{Tmrt\}\text{^}4] - fcihc\,(tci - ta) \quad (8)$$

Which is the average radiation temperature in the Finger relationship ، $Tmrt$ and Tci is calculated as shown in equation 9 and 10.

$$Tmrt^{\,4} = T1^4\,FP - 1 + T2^4\,FP - 2 + Tn^4\,FP - N \quad (9)$$

and

$$Tci = 35.5 - 0.028(M - W) - 0.155\ Ici\ \{3.96 \times 10^{-8}\ fci\ [((tci + 273^4) - Tmrt^4\ ] + fcihc\,(Tci - Ta)\} \quad (10)$$

The terms $FP{-}1$ to $FP{-}N$ are the visibility coefficients of the human body with each side surface. These values can be calculated according to the situation of the people in the house and also their situation, whether they are sitting or standing. The value of PMV is between -3 and +3, and according to ASHRAE installation instructions, any integer between these two values somehow expresses the thermal feeling of the building occupants from the environmental conditions.

5. Research Methodology

Given the nature of the data, this research falls into the quantitative category. Since it measures the energy loss variables by varying the types of building envelope materials and thermal insulations used, it employs a correlational approach.

Considering that the goal of this study is to improve behaviors, methods, materials, and insulation used in construction, leading to the development of practical knowledge in the construction industry, it qualifies as applied research.

5.1. Software Used

For this research, Design Builder software version 6.1.0.006 was utilized.

Design Builder Software

Design Builder software facilitates building modeling from various aspects, including building physics (construction materials), architectural design, heating and cooling systems, lighting systems, and more. Apart from modeling heating and cooling loads, it dynamically simulates various energy usages in buildings, such as heating, cooling, lighting, appliances, and domestic hot water. Additionally, it can model day lighting and even CFD (Computational Fluid Dynamics). Other capabilities include natural and mechanical ventilation modeling, thermal comfort assessment in indoor spaces, and energy gains/losses from different building components. The results of these simulations can be extracted for the entire year, specific months, daily, and even hourly. Furthermore, the results can be obtained for the entire building, different floors, and individual spaces. A special feature of this software is the ability to present modeling results in the form of diagrams or tables, which can be useful for subsequent analyses.

5.2. Case Study Sample

The case study in this research involves a five-story residential building located in Tehran. The first floor serves as a parking area, while the other four floors are residential units. Each floor contains one apartment unit with an approximate area of 100 square meters. Each apartment includes two bedrooms, an open kitchen, a living room, a bathroom, a toilet, and a balcony. The floor plan zoning is depicted in Figure 4, with the building oriented to the south, where the living room and kitchen are on the north side and the bedrooms are on the south side. The land area is 250 square meters, with an occupancy area of 150 square meters. Exterior views of the building are shown in Figures 5A, 5B.

Building Components:

Roof (Top Layer) Defined with 5 layers:

1. First layer: Bituminous waterproofing (a protective polymer layer based on bitumen and synthetic fibers) with a thickness of 3 mm.
2. Second layer: Cement plaster with a thickness of 2 cm.
3. Third layer: Concrete foam with a thickness of 20 cm.
4. Fourth layer: Reinforced concrete with a thickness of 20 cm.
5. Fifth layer: Gypsum and clay with a thickness of 2 cm.

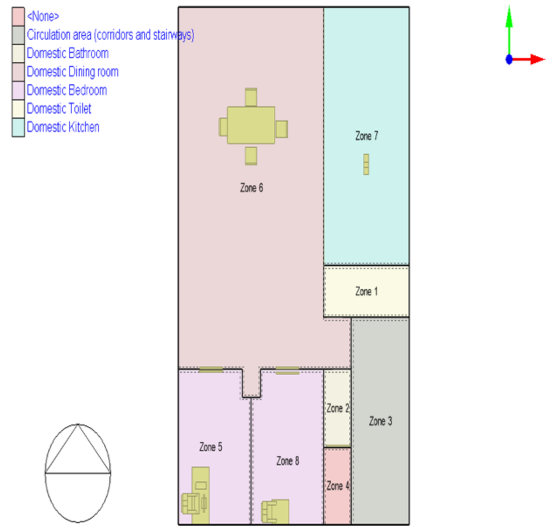

Fig. 4. Building Plan and Zoning

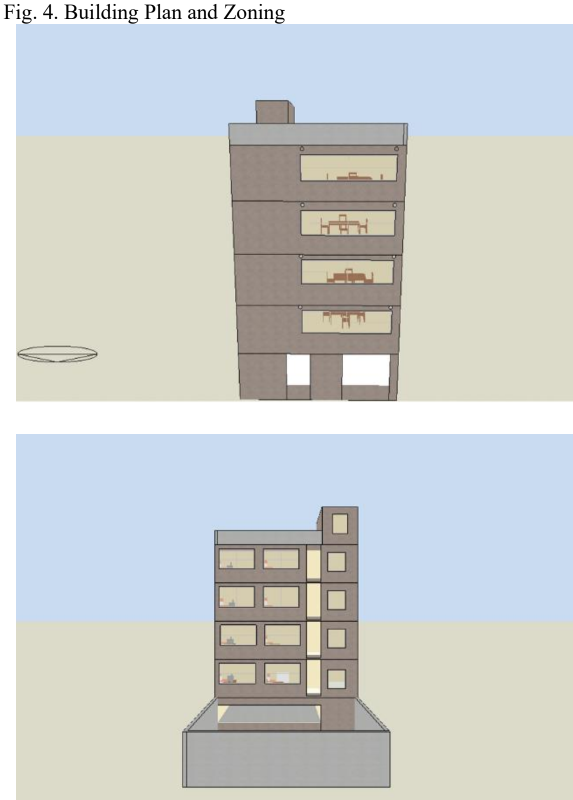

Fig. 5.a) Northern Facade of the Building. b) Southern Facade of the Building

Interior Walls (3 layers):

1. First layer: Gypsum and clay with a thickness of 2 cm.

2. Second layer: Lightweight aerated concrete blocks with a thickness of 10 cm.
3. Third layer: Gypsum and clay with a thickness of 2 cm.

Floor (Parking Level, 4 layers):

1. First layer: Granite stone with a thickness of 3 cm.
2. Second layer: Cement plaster with a thickness of 2 cm.
3. Third layer: Hand-compacted soil with a thickness of 20 cm.
4. Fourth layer: Reinforced concrete with a thickness of 1 meter.

Intermediate Floors and Ceilings (5 layers):

1. First layer: Ceramic tiles with a thickness of 1 cm.
2. Second layer: Cement plaster with a thickness of 2 cm.
3. Third layer: Concrete foam with a thickness of 10 cm.
4. Fourth layer: Reinforced concrete with a thickness of 20 cm.
5. Fifth layer: Gypsum and clay with a thickness of 2 cm.

Exterior Walls (Four Layers):

1. A 2 cm cement plaster layer.
2. A 15 cm AAC block.
3. The variable insulation layer (depending on the scenario).
4. A 2 cm gypsum finishing layer.

Windows (30% of wall area):

1. Double-glazed windows (2 layers of 3 mm clear glass with a 6 mm air gap).
2. UPVC frames without external shading, but with internal roller blinds made of aluminum.

Natural Ventilation:

1. Each unit has two non-mechanical ventilation openings with roller blinds, circular, and a diameter of 10 centimeters.

Lighting:

1. All lighting is LED, and external façade lights have sensors, operating for 12 hours.

Heating and Domestic Hot Water:

1. Gas-based heating and domestic hot water system (one unit per zone).
2. Cooling system: Water-cooled air conditioning with electricity consumption.

Unit Zoning:

Each unit is divided into the following zones:

1. Living room
2. Open kitchen
3. Two bedrooms
4. One toilet
5. One bathroom
6. One balcony connected to one of the bedrooms.

Occupancy:

Each unit accommodates 4 people.

Weather Data:

Weather data for the region was provided to the software via a file.

The geographical location of this building is at 68.35° latitude and 32.51° longitude. The building's elevation above sea level is 1191 meters. The prevailing wind direction is from west to east, with an average speed of 11.9 meters per second. Weather simulation data from Tehran's Mehrabad Airport has been used for the analysis.

The heating system in each unit consists of wall-mounted gas heaters and radiators. Each unit has five radiators installed. The hot water supply for each unit also comes from the same system, while the cooling system relies on electricity.

Regarding the structural elements, they are categorized based on their controlled or uncontrolled exposure and various types, as shown in Figure 6.a and 6.b.

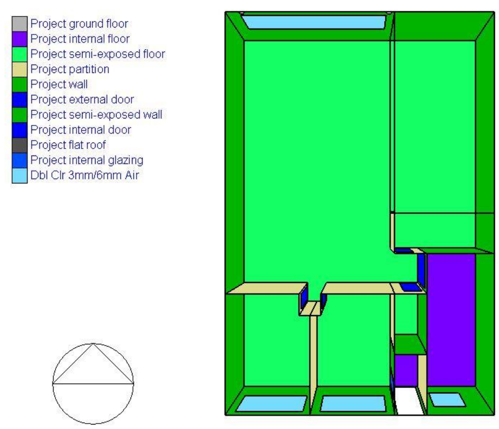

a)

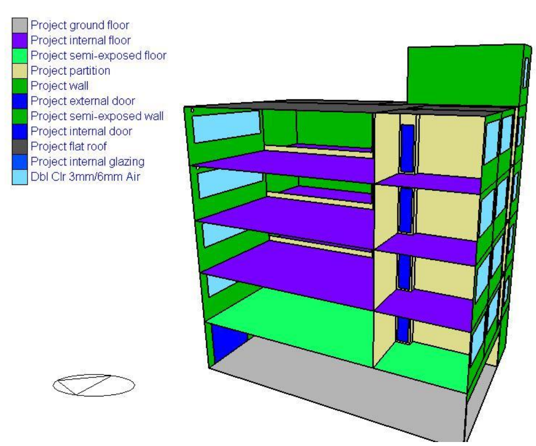

b)

Fig. 6.a) Building surfaces and openings. b) Building surfaces and openings

6. Research Steps

1. Data Collection:
Gather architectural, structural, electrical, and mechanical plans for the studied building.
2. Weather Data Preparation:
Compile relevant weather information.
3. Building Use Definition:
Specify the intended use of the building.
4. Building Model Creation:
Develop a model of the building.
Define zones within each unit.
5. Zone Definition:
Assign specific uses to each zone.
6. Material Definitions and Structural Elements:
Define building materials and structural components.
7. Opening Definitions:
Specify openings (doors, windows, etc.).
8. Lighting Definitions:
Define lighting systems and their intensity.
9. Heating and Cooling System Definition:
Describe the heating and cooling systems used in the units.
10. Model Simulation:
Simulate the building model.
11. Output Compilation:
Collect simulation results in a table.

7. Validation

Fathalian and Kargar Sharifabad (2019) in research titled Investigating the effect of different energy optimization strategies in building energy classification using design builder software and Zomorodian and Tehsil Doost (2019) in research titled Validation of energy simulation software in buildings: with an experimental and comparative approach. Validation of two energy simulation software programs, Eco Tech and Design Builder. Witt et al. (2001), Heninger et al. (2003), and Gatti (2003) have each investigated the validity of Energy Plus software in separate research. In all the above research, the validity and correctness of the results of these software programs have been confirmed. Also, by studying the results of the following tests, which are based on different standards, you can be sure of the accuracy of the results and outputs of the Design Builder and Energy Plus software.

- EnergyPlus Testing with ANSI/ASHRAE Standard 140-2001
- EnergyPlus Testing with HVAC BESTEST Part 1 - Tests E100 to E200
- DesignBuilder v6 Compliance With ANSI/ASHRAE/ACCA Standard 183-2007
- ANSI/ASHRAE Standard 140-2017 Building Thermal Envelope and Fabric Load Tests DesignBuilder v6.1 with EnergyPlus v8.9 27 Jan 2021
- ANSI/ASHRAE Standard 140-2017 Space-Cooling Equipment Performance Analytical Verification Tests AE101 to AE445 DesignBuilder v6.1 with EnergyPlus v8.9 27 Jan 2021
- ANSI/ASHRAE Standard 140-2017
- Space-Cooling Equipment Performance Analytical Verification Tests CE100 to CE200 DesignBuilder v6.1 with EnergyPlus v8.9 27 Jan 2021
- ANSI/ASHRAE Standard 140-2017 Space-Heating Equipment Performance Tests
- HE100 to HE230 DesignBuilder v6.1 with EnergyPlus v8.9 27 Jan 2021

8. Findings

This research investigates the impact of using insulation layers in external building walls and compares energy consumption in different scenarios. To better understand this, we will analyze the energy consumption of a building over a one-year operational period, using examples of software output. For instance, Table 1 shows energy consumption broken down by consumption sector, and Table 2 shows energy consumption broken down by energy type.

Table 1.
Energy Consumption Categorized by Usage

Fuel Breakdown (Run period: 1 Year)	
Room Electricity	9543.45 (kWh)
Lighting	10364.7 (kWh)
Heating	4346.79 (kWh)
Cooling (Electricity)	14196.07 (kWh)
DHW (Gas)	17658.32 (kWh)
Exterior lighting	384.85 (kWh)

Table 2.
Energy Consumption Categorized by Type of Energy

Fuel Totals (Run period: 1 Year)	
Electricity	34489.06 (kWh)
Gas	22005.12 (kWh)

The building materials used for the construction of 15-centimeter-thick external walls are autoclaved aerated concrete (AAC) blocks. The layering of the external wall is shown in Figure 4.

A total of 10 different scenarios are defined using 9 distinct insulation layers. These scenarios are identified using coding. In all scenarios, the interior wall finish is defined as a 2 cm plaster layer, marked with the letter G. The insulation layers placed on the internal side before plastering include cork (C), coconut pith (CP), fiberglass

Table. 3.
Energy Consumption by Scenario

Scenario	Heat Loss	Electricity Consumption (kWh)	Gas Consumption (kWh)	Total Energy Consumption (kWh)
G-0-AAC-C	-7700.10	34489.06	22005.12	56494.18
G-CP-AAC-C	-7312.93	34359.80	21575.89	55935.69
G-C-AAC-C	-7131.40	34297.39	21394.72	55692.11
G-GW-AAC-C	-7133.28	34293.54	21397.01	55690.55
G-PW-AAC-C	-7530.16	34440.87	21814.43	56255.30
G-PS-AAC-C	-7134.02	34301.79	21398.13	55699.92
G-PU-AAC-C	-6914.18	34241.50	21182.53	55424.03
G-R-AAC-C	-7248.67	34336.88	21510.66	55847.54
G-SW-AAC-C	-7134.04	34304.33	21398.91	55703.24
G-W-AAC-C	-7106.36	34292.33	21369.88	55662.21

Table. 4.
Sorted by Electricity Consumption

Scenario	Heat Loss	Electricity Consumption (kWh)	Gas Consumption (kWh)	Total Energy Consumption (kWh)
G-PU-AAC-C	-6914.18	34241.5	21182.53	55424.03
G-W-AAC-C	-7106.36	34292.33	21369.88	55662.21
G-GW-AAC-C	-7133.28	34293.54	21397.01	55690.55
G-C-AAC-C	-7131.4	34297.39	21394.72	55692.11
G-PS-AAC-C	-7134.02	34301.79	21398.13	55699.92
G-SW-AAC-C	-7134.04	34304.33	21398.91	55703.24
G-R-AAC-C	-7248.67	34336.88	21510.66	55847.54
G-CP-AAC-C	-7312.93	34359.8	21575.89	55935.69
G-PW-AAC-C	-7530.16	34440.87	21814.43	56255.3
G-0-AAC-C	-7700.1	34489.06	22005.12	56494.18

Table. 5
Sorted by Gas Consumption

Scenario	Heat Loss	Electricity Consumption (kWh)	Gas Consumption (kWh)	Total Energy Consumption (kWh)
G-PU-AAC-C	-6914.18	34241.5	21182.53	55424.03
G-W-AAC-C	-7106.36	34292.33	21369.88	55662.21
G-C-AAC-C	-7131.4	34297.39	21394.72	55692.11
G-GW-AAC-C	-7133.28	34293.54	21397.01	55690.55
G-PS-AAC-C	-7134.02	34301.79	21398.13	55699.92
G-SW-AAC-C	-7134.04	34304.33	21398.91	55703.24
G-R-AAC-C	-7248.67	34336.88	21510.66	55847.54
G-CP-AAC-C	-7312.93	34359.8	21575.89	55935.69
G-PW-AAC-C	-7530.16	34440.87	21814.43	56255.3
G-0-AAC-C	-7700.1	34489.06	22005.12	56494.18

wool (GW), plywood (PW), polystyrene (PS), polyurethane foam (PU), rock wool (SW), rice husk (R), and wool (W), as well as a non-insulated option (0). All insulation layers have a uniform thickness of 1 cm. The external finish of the building is defined as ca cement layer with a thickness of 2 cm, marked as (C). To facilitate comparison, the energy outputs of all 10 scenarios are collected in table 3.

Note: In all scenarios, wall systems, openings, structural and non-structural elements, and other variables remain consistent, with the only difference being the insulation layer. For calculation ease, the Design Builder software expresses gas consumption in kilowatt-hours. To determine the cost of gas consumption and convert it to cubic meters, kilowatt-hours are divided by 10.4 (the calorific value of each cubic meter of gas).

In table 3, the first column lists the coded scenarios. The second column shows heat loss from the external envelope, the third column indicates total electricity consumption for the building, the fourth column presents annual gas consumption during the operational phase, and the fifth column displays total energy consumption. Sorting this table by the metrics mentioned results in tables 4, 5, and 6.

Table. 6
Sorted by Total Energy Consumption

Scenario	Heat Loss	Electricity Consumption (kWh)	Gas Consumption (kWh)	Total Energy Consumption (kWh)
G-PU-AAC-C	-6914.18	34241.5	21182.53	55424.03
G-W-AAC-C	-7106.36	34292.33	21369.88	55662.21
G-GW-AAC-C	-7133.28	34293.54	21397.01	55690.55
G-C-AAC-C	-7131.4	34297.39	21394.72	55692.11
G-PS-AAC-C	-7134.02	34301.79	21398.13	55699.92
G-SW-AAC-C	-7134.04	34304.33	21398.91	55703.24
G-R-AAC-C	-7248.67	34336.88	21510.66	55847.54
G-CP-AAC-C	-7312.93	34359.8	21575.89	55935.69
G-PW-AAC-C	-7530.16	34440.87	21814.43	56255.3
G-0-AAC-C	-7700.1	34489.06	22005.12	56494.18

9. Conclusion

The findings indicate that the best thermal insulation layer for reducing energy consumption is polyurethane foam. By comparing Tables 4 and 5, it is evident that the rankings of scenarios G-GW-AAC-C and G-C-AAC-C differ in terms of electricity and gas consumption. Specifically, using glass wool insulation results in greater electricity savings, whereas cork insulation leads to higher gas savings.

Analyzing Tables 4, 5, and 6 makes it clear that scenario G-0-AAC-C, which represents the case without using any thermal insulation layer, ranks last.

- Not using a thermal insulation layer results in the loss of 247.56 kilowatt-hours of electricity in one year.
- Not using a thermal insulation layer results in the loss of 79 cubic meters of gas in one year.
- Not using a thermal insulation layer results in the loss of 1070.15 kilowatt-hours of total energy in one year.

The data emphasize the critical role that thermal insulation plays in reducing energy consumption and highlight the considerable energy-saving potential of polyurethane foam in particular. This insight underscores the importance of selecting the appropriate insulation layer to optimize energy efficiency in buildings.

References

[1] Azizkhani, M., A. Vakili, Y. Noorollahi, and F. Naseri. "Potential survey of photovoltaic power plants using Analytical Hierarchy Process (AHP) method in Iran." Renewable and Sustainable Energy Reviews 75 (2017): 1198–1206. https://doi.org/10.1016/j.rser.2016.11.103

[2] Ramakrishnan, S., X. Wang, J. Sanjayan, and J. Wilson. "Thermal performance of buildings integrated with phase change materials to reduce heat stress risks during extreme heatwave events." Applied Energy 194 (2017): 410–421. https://doi.org/10.1016/j.apenergy.2016.04.084

[3] Navayi, A. M., A. F. Jouzayi, A. Ghafouri, and M. M. Adeli. "The effect of using air gap in the walls on reducing the energy consumption of a residential building." New Practice and Computer Findings in Mechanics and Systems (2023). https://civilica.com/doc/2053356

[4] Soltani, M. and A. Atashi. "Second Skin of Facade Impact on Office Building Life Cycle Energy Consumption: A Comparative Study." International Journal of Architectonic, Spatial, and Environmental Design 18.1 (2024).

[5] Feehan, A., H. Nagpal, A. Marvuglia, and J. Gallagher. "Adopting an integrated building energy simulation and life cycle assessment framework for the optimisation of facades and fenestration in

building envelopes." Journal of Building Engineering 43 (2021): 103138. https://doi.org/10.1016/j.jobe.2021.103138
[6] Ustaoglu, A., A. Yaras, M. Sutcu, and O. Gencel. "Investigation of the residential building having novel environment-friendly construction materials with enhanced energy performance in diverse climate regions: Cost-efficient, low-energy and low-carbon emission." Journal of Building Engineering 43 (2021): 102617. https://doi.org/10.1016/j.jobe.2021.102617
[7] Pedroso, M., J. de Brito, J. D. Silvestre, and V. M. Ferreira. "Characterisation of a multilayer external wall thermal insulation system. Application in a Mediterranean climate." Journal of Building Engineering 30 (2020): 101265. https://doi.org/10.1016/j.jobe.2020.101265
[8] Mahmoud, S., M. Fahmy, M. Mahdy, I. Elwy, and M. Abdelalim. "Comparative energy performance simulation for passive and conventional design: A case study in Cairo, Egypt." Energy Reports 6 (2020): 699–704. https://doi.org/10.1016/j.egyr.2019.09.052
[9] Mirrashid, N. and L. Mirsaeedie. "The Effect of Thrombus Wall System on Thermal Comfort in Temperate and Humid Climates (Case study of a residential building in Gonbad Kavous)." (2020).
[10] Fathalian, A. and H. Kargarsharifabad. "Investigating the effect of different energy saving strategies on energy rating of building by design builder software (case study: office building)." (2020).
[11] Toosi, Golnoosh. "Influence of Vegetation in The Flood Drainage Ditch." Journal of Civil Engineering Researchers 5.4 (2023): 16–21. https://doi.org/10.61186/JCER.5.4.16
[12] Alimohammadi, Hossein and Ashfaq A. Memon. "Case Study of Mechanically Stabilized Earth (MSE) Retaining Wall Failure in the State of Tennessee; Recommendations for Future Design and Constructions." Journal of Civil Engineering Researchers 5.1 (2023): 52–65. https://doi.org/10.61186/JCER.5.1.52
[13] Oliaei, Mohammadreza, Mahdi Mashhadiyan, and Reza Forootan. "Seismic Performance Evaluation of Friction Damper and Yielding Metallic Damper in Steel Frame." Journal of Civil Engineering Researchers 5.3 (2023): 1–14. https://doi.org/10.61186/JCER.5.3.1

J-Researchers

Journal of Civil Engineering Researchers

Journal homepage: www.journals-researchers.com

Forensic Investigation and Petrographic Analysis of Concrete Apron Distresses; A Case Study in Nashville, Tennessee)

Hossein Alimohammadi,[a,*] David A. Been,[a] and James Duncan[a]

[a] Terracon Consultants, Inc., Nashville, TN, USA 37217

ABSTRACT

This study presents a forensic investigation into pavement distress in a concrete apron located in Nashville, Tennessee. The investigation involved detailed engineering observations and a comprehensive pavement condition survey in accordance with ASTM D5340. To identify the underlying causes of deterioration, petrographic examinations were conducted on three concrete cores extracted from the apron, following ASTM C856 guidelines. The analysis revealed consistent aggregate distribution, primarily composed of micritic limestone and quartz-based sand, with air content (total of entrapped and purposefully entrained air) ranging from 3.9% to 5.2% and air void spacing factors exceeding American Concrete Institute (ACI) recommendations for freeze-thaw durability. No carbonation was detected in the cores, but moderate to abundant ettringite, calcium hydroxide, and alkali-silica gel resulting from Alkali-Silica Gel (ASG) were observed lining voids and fractures. The findings indicate that Alkali-Silica Reaction (ASR)-related damage, exacerbated by cyclic wetting and drying, is a primary contributor to the pavement deterioration. Freeze-thaw damage due to inadequate air entrainment was also identified as a contributing factor. Based on the results, recommendations for improving the long-term performance and durability of the concrete apron include using low-alkali cement, selecting better-graded and less reactive aggregates, increasing the percentage of purposefully entrained air to reduce air void spacing and improve freeze-thaw durability, and incorporating supplementary cementitious materials (SCMs) to reduce alkali availability and enhance ASR resistance. We note the use of lithium nitrate has also been proven to mitigate ASR in new concrete. However, the mechanism of mitigation is not fully understood, and the relatively high cost and limited availability of lithium introduces challenges for this alternative. This study underscores the importance of petrographic examination in understanding concrete deterioration mechanisms and developing targeted repair strategies to enhance infrastructure durability.

ARTICLE INFO

Received: April 05, 2025
Accepted: August 21, 2025

Keywords:
Concrete Apron
Petrographic Examination
Freeze-thaw Damage
Freeze-thaw Damage
Petrographic Analysis

DOI: 10.61186/JCER.7.3.40
DOR: 20.1001.1.2538516.2025.7.3.4.4

1. Introduction

Concrete pavements are widely used in infrastructure due to their strength, durability, and cost-effectiveness. Their ability to withstand heavy loads and environmental stresses makes them a preferred choice for highways, airport runways and aprons, and other critical infrastructure [1] to [3]. However, despite their inherent strength,

* Corresponding author. Tel.: +12254853307; e-mail: Hossein.Alimohammadi@terracon.com.

concrete pavements are susceptible to various forms of deterioration over time, including cracking, scaling, and spalling, which can significantly reduce their lifespan and structural integrity. Among the various mechanisms of concrete deterioration, alkali-silica reaction (ASR) is one of the most critical factors affecting the long-term durability of concrete pavements. ASR leads to the formation of expansive gels within the concrete matrix, causing internal stresses that result in cracking and surface degradation. Understanding the causes and progression of ASR is essential for improving the performance and longevity of concrete pavements [4] to [8].

Petrographic analysis has emerged as a valuable tool for diagnosing the causes of concrete deterioration, including ASR and other chemical and physical damage. It provides critical insights into the microstructural and mineralogical characteristics of concrete, enabling engineers to identify reactive aggregates, monitor gel formation, and assess microcracking [9] to [15]. The ability to diagnose ASR-related distress at an early stage allows for the implementation of targeted mitigation strategies, improving the performance and longevity of concrete pavements. Petrography involves the microscopic examination of concrete core samples to evaluate the composition, texture, and microstructural characteristics of concrete. The American Society for Testing and Materials (ASTM) provides guidelines for petrographic examination under ASTM C856 – Standard Practice for Petrographic Examination of Hardened Concrete (ASTM, 2022) [1]. Petrographic analysis helps identify the mineralogical composition of aggregates, the presence of reactive products, microcracking patterns, and evidence of chemical reactions such as ASR. Through petrography, engineers can diagnose deterioration mechanisms, evaluate the quality of construction materials, and assess the effectiveness of mitigation strategies [16] to [22].

Alkali-silica reaction is a chemical reaction between the hydroxyl ions (OH^-) in the pore solution of concrete and reactive silica in aggregates. When reactive aggregates, such as opaline chert, strained quartz, and volcanic glass, are exposed to high-alkali environments, they form an expansive alkali-silica gel. This gel absorbs moisture and swells, generating internal tensile stresses that lead to cracking, surface spalling, and reduced structural integrity of concrete pavements (Swamy, 2002) [23] to [29]. The severity of ASR-related damage depends on several factors, including the type and reactivity of aggregates, the alkali content of the cement, and the availability of moisture (Thomas et al., 2013). Fournier and Bérubé (2000) [30] demonstrated that ASR-related damage is progressive and accelerates under cyclic wetting and drying conditions, which increase moisture availability and enhance the swelling of the gel.

Petrographic analysis allows for the early detection of ASR-related distress by identifying reactive products and microstructural changes in concrete. ASR gel typically appears as a birefringent material under polarized light microscopy, forming within cracks and voids around reactive aggregates. The formation of microcracks and reaction rims on aggregate surfaces is a common indicator of ASR activity (Thomas and Fournier, 2013) [31]. Optical microscopy is used to identify aggregate types, cracks, and reaction products, while scanning electron microscopy (SEM) provides detailed insights into the chemical composition and morphology of the gel (Scrivener & Kirkpatrick, 2008). SEM combined with energy-dispersive spectroscopy (EDS) allows for precise identification of reaction phases and the extent of silica dissolution [32] to [37].

Petrographic examination is instrumental in diagnosing ASR and assessing its impact on concrete durability. It enables the identification of reactive aggregates, the degree of microcracking, and the distribution of alkali-silica gel within the concrete matrix. Poole (1991) [38] emphasized that petrographic analysis provides a detailed understanding of the microstructure of concrete and the interaction between aggregates and the cement paste. This information is critical for identifying the root causes of ASR and implementing effective mitigation strategies.

Studies have shown that ASR-related damage is influenced by both intrinsic and extrinsic factors. Intrinsic factors include the mineralogical composition of aggregates and the chemical properties of the cement. Aggregates containing opal, chert, and strained quartz are highly susceptible to ASR due to their high silica content and reactive nature (Stark, 1991) [39]. The alkali content of the cement also plays a significant role, with high-alkali cements increasing the availability of hydroxyl ions for the reaction. Extrinsic factors such as moisture availability, temperature fluctuations, and exposure to deicing salts further accelerate ASR-related deterioration (Sanchez et al., 2017). Pavements subjected to high traffic loading experience additional mechanical stresses that exacerbate internal cracking, moisture infiltration and the progression of ASR (Stark and Gress, 1994) [40].

Petrographic analysis also has proven useful in evaluating the effectiveness of mitigation strategies for ASR. The use of supplementary cementitious materials (SCMs) such as fly ash, slag, and silica fume has been shown to reduce ASR by lowering the alkali content of the concrete and modifying the pore structure (Shehata and Thomas, 2000) [41]. SCMs reduce the availability of hydroxyl ions and limit the expansion of alkali-silica gel, thereby improving the durability of concrete pavements. Petrographic examination of SCM-treated concrete often reveals reduced gel formation, improved aggregate-paste bonding, and decreased microcracking, confirming the success of these mitigation strategies.

Petrographic analysis provides insights into secondary reactions and microstructural changes associated with ASR. The formation of secondary deposits, such as calcium hydroxide and ettringite, within cracks and voids is a sign of ongoing chemical activity (Grattan-Bellew, 1995) [42]. Delayed ettringite formation (DEF) is another durability issue that can occur in conjunction with ASR, particularly in high-temperature curing conditions. DEF leads to additional expansion and cracking, compounding the damage caused by ASR (Taylor, 1997) [43]. The identification of these secondary products through petrography provides valuable evidence of the chemical and physical processes affecting concrete performance.

Microstructural defects such as poor compaction, inadequate air-void spacing, and improper aggregate grading can also compromise concrete durability [44] to [51]. Petrographic examination helps identify these flaws and their contribution to reduced performance. Mehta and Monteiro (2014) [52] noted that well-graded aggregates, low water-cement ratios, and proper curing enhance concrete durability, while deficiencies in these areas lead to increased permeability, shrinkage cracking, and freeze-thaw damage. Petrography provides a means of diagnosing these issues and informing corrective measures [53] to [62].

a) b)

Figure 1 a) and b) existing durability cracking and potential alkali-silica reaction distresses observed on the existing concrete

This study includes a forensic investigation of concrete pavement distress in Tennessee, focusing on ASR-related damage in a concrete apron. Concrete core samples were extracted and analyzed using petrographic techniques to identify the presence of reactive aggregates, alkali-silica gel, and microcracking patterns. The analysis provided evidence of ASR activity and highlighted contributing factors such as high alkali content in the cement, aggregate reactivity, exposure to moisture, lack of purposefully entrained air and excessive air void spacing. Based on the findings, recommendations were developed for mitigating ASR and improving the long-term performance of the concrete apron. These recommendations included the use of low-alkali cement, improved aggregate selection, the incorporation of SCMs to reduce alkali availability and improve resistance to ASR and increasing the amount of purposefully entrained air to improve freeze-thaw durability. The findings from this study highlight the importance of petrographic examination in forensic investigations and the development of durable concrete mixtures. Further advancements in petrographic techniques and analytical methods will continue to enhance the understanding and management of ASR and other durability challenges in concrete infrastructure.

2. Case study information, introduction and background

This study was conducted first to evaluate the Pavement Condition Index (PCI) of an existing concrete apron located in Nashville, Tennessee. The primary objective was to perform a forensic investigation of the existing distresses observed in the concrete apron and to provide recommendations for addressing the underlying causes and developing an appropriate rehabilitation plan. Terracon performed detailed engineering observations and a comprehensive condition survey during site visits. The surveyed area covered approximately 100,003 square feet of concrete apron. A range of distresses of varying severity levels were identified on the concrete apron during the survey. The observed distress types included: Corner Breaks, Settlement/Faulting, Longitudinal, Transverse, and Diagonal Cracks, Joint Seal Damage, Spalling at Corners and Joints, Patching (Small, ≤ 5 square feet), Scaling, Durability Cracking (D-Cracking), and evidence of Alkali-Silica Reaction (ASR). The visual pavement condition survey was conducted in general accordance with ASTM D5340 and locally accepted pavement engineering practices. Evidence of durability cracking, slab division, corner breaks, and joint spalling was present in all sample unit slabs of the rigid concrete pavement apron. These types of failures are typically associated with factors such as Freeze-thaw susceptibility of the aggregates, Poor concrete quality, Chemical reactions between the aggregates and the cementitious matrix, Over-finishing of the slab, Loss of surface moisture during placement due to environmental conditions (e.g., air temperature and wind).

The D-cracking observed at the joints of the concrete panels indicated a significant issue with freeze-thaw durability of the concrete and exposure to moisture. The widespread map cracking in the concrete apron slabs, extrusion of joint sealant and spalling of the concrete suggested the potential involvement of alkali-silica reaction (ASR). To confirm the presence of ASR and better understand the distress mechanisms, a petrographic investigation involving core sampling was performed. This testing enabled a more accurate diagnosis of the underlying causes and allowed for the formulation of targeted repair solutions. Figures 1 a and b illustrate the existing durability cracking and alkali-silica reaction distresses observed on the existing concrete.

3. Petrographic Examinations

Three concrete cores (designated as C-1 through C-3), each with a diameter of 95 mm, were extracted from the site and analyzed at Terracon's materials laboratory in Cincinnati, Ohio. The objective of the petrographic examination was to identify the cause(s) of the observed cracking and deterioration. The investigation was performed in accordance with ASTM C856. As restrictions to this study, it should be mentioned that no approved concrete mix design, batch plant records, or concrete break reports (beams and/or cylinders) were available for review. Additionally, daily field observation reports containing information regarding ambient weather conditions during placement, construction procedures, or finishing methods were not provided. Lack of pertinent information is unfortunately typical in forensic/failure studies. Therefore, all findings and conclusions are based exclusively on the observations from the obtained cores.

Table 1
Concrete Proportions and Hardened Air Contents, % Volume

Core ID	Total Aggregate	Total Hardened Paste[1]	Total Air[2]
C1	61.7	33.1	5.2 (1.6)
C2	65.2	30.2	4.6 (2.4)
C3	65.3	30.8	3.9 (2.3)

1- Hardened paste includes the total of all cementitious materials.
2- Numbers in parentheses represent entrapped-size air (>0.04 inches). ASTM C457 (procedure B) does not distinguish between entrained and entrapped air. The distinction is made by the petrographer based on void size, shape, and location.

Table 2
Air Void System Parameters

Core ID	Length of Traverse (in)	Total Air Content (%)	Paste/Air Ratio[1]	Void Frequency (voids/mm)[2]	Average Chord Length (mm)	Specific Surface (mm^2/mm^3)[2]	Void Spacing Factor[2] (mm)
C1	135.2	5.18	6.40	4.49	0.2921	346.9	0.37846
C2	133.5	4.64	6.50	3.16	0.37338	272.3	0.48768
C3	129.7	3.86	8.00	3.25	0.29972	337.6	0.4318

1- Paste/Air Ratio values fall within the specifications recommended in ACI 201 and Appendix X1 of ASTM C457/C457M.
2- Void Frequency, Specific Surface, and Void Spacing Factor values do not fall within the recommended ranges in ACI 201 and Appendix X1 of ASTM C457/C457M. ASTM C457 Procedure B.

3.1. Petrographic Methodology

All three cores were examined visually and stereomicroscopically following ASTM C856. Air void system parameters were determined using ASTM C457, Procedure B (Modified Point Count). Portions of the cement paste from the samples were also analyzed under polarized light microscopy with refractive index oils to detect the presence of ground granulated blast-furnace slag (GGBFS). Photographs of the cores were taken at three stages including: as received in the lab, after lapping and following the application of phenolphthalein stain. The core images are included in Figures 2 to 9, along with photomicrographs of thin sections. Volumetric concrete proportions and air void system parameters are summarized in Tables 1 and 2, respectively.

Thin sections, approximately 25 microns thick, were prepared from each core to assess carbonation, the depth of deterioration, micro-fracturing, cement hydration, and the presence and extent of deleterious chemical reactions. Blue-dyed epoxy was used during thin section preparation to enhance the visibility of microstructural features

3.2. General Core Characteristics

The examined cores exhibited similar material characteristics. The concrete contained a 19 mm maximum size crushed micritic limestone. The coarse aggregate was fresh, angular, and densely packed. The fine aggregate was a subrounded natural sand comprised mainly of quartz with subordinate chert and granite and lesser coarse fines (limestone). Distribution of the aggregate was generally even, with no segregation or preferred orientation in any of the cores.

a) b) c)

Figure 2 a) Core C1 as received, b) sawn surface after the application of phenolphthalein stain indicating no carbonation, and c) sawn and polished surface. Fractures noted in red.

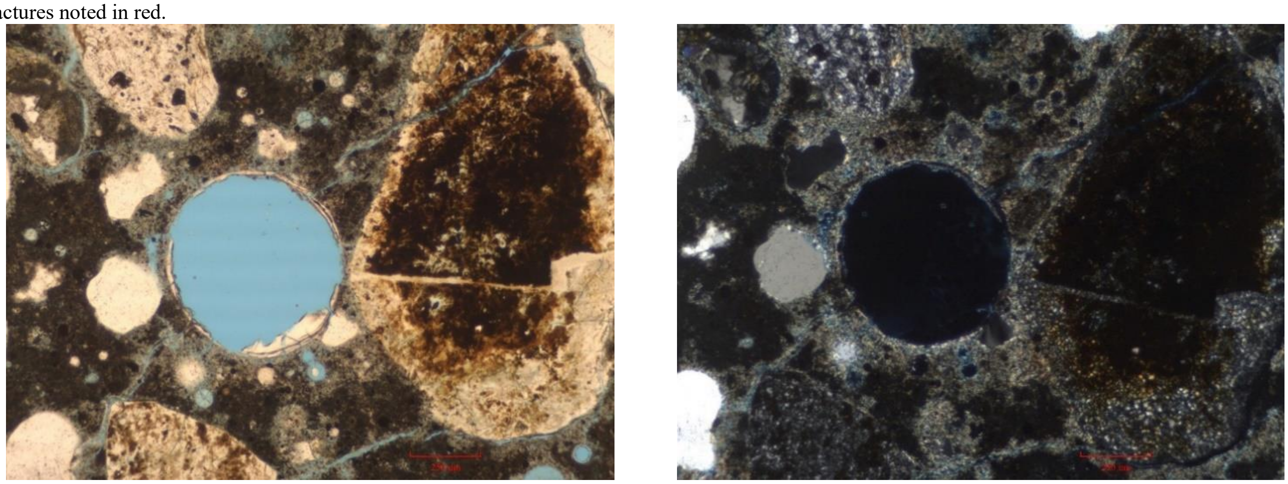

a) b)

Figure 3 a) Core C1 photomicrograph of alkali silica gel (ASR) lining a void with fractures through paste and aggregate. Plane polarized light. b) photomicrograph of alkali silica gel (ASR) lining a void with fractures through paste and aggregate. Cross polarized light.

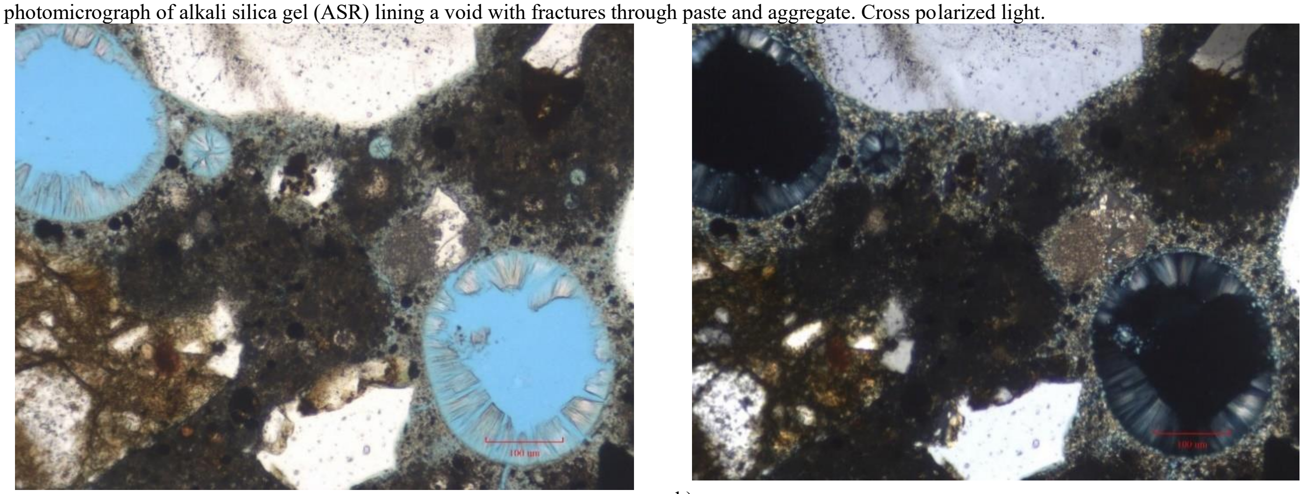

a) b)

Figure 4 a) Core C1 photomicrograph of ettringite lined/filled voids. Plane polarized light. b) photomicrograph of ettringite lined/filled voids. Cross polarized light.

Cementitious materials consisted of fairly to moderately well-hydrated Portland cement, with minor to moderate un-hydrated fly ash. The concrete was slightly to moderately air entrained. Void fillings were common, and most voids and fractures contained deposits of calcium hydroxide, calcium carbonate, ettringite, and varying degrees of ASR. Based on the application of phenolphthalein stain, the concrete was not carbonated.

Core C1 Summary of Analysis

The overall core was approximately 280 mm long by 95 mm in diameter. The core was received in the lab as intact, with a network of fine fractures throughout, illustrated in Figures 2 to 4. The exterior surface was sandy, slightly discolored, and exhibited slight chipping around the core circumference. The core was a full-depth core and terminated at an asphalt base. No steel reinforcement or wire mesh was observed.

Drilled surfaces exhibited moderate entrained air. Overall air content was 5.2%. Air distribution appeared moderately even throughout. No honeycombing nor coalescing voids were visibly apparent. Minor irregularly shaped voids were observed. The largest air void was approximately 6 mm in size. Void fillings were common, with most consisting of calcium hydroxide and calcium carbonate, as well as ettringite.

The matrix was hard and moderately dense. The matrix was greenish gray and uniform in color (Munsell color 5GY 5/1) when wet. Cementitious materials consisted of fairly to moderately hydrated Portland cement and fly ash. Slag cement was not present. Aggregate-matrix bonds were strong, with the concrete breaking predominantly through the coarse aggregate when struck by a hammer. However, micro-fracturing was common, and occurred both in the cement paste, and occasionally through limestone coarse aggregate particles. Calcium hydroxide was also observed in many of these fractures, as fillings/linings in voids, and along fracture surfaces. Moderate to abundant ettringite was frequently observed as both fracture and void fillings/linings. Alkali silica gel was observed in minor amounts as deposits in fractures. Based on the application of phenolphthalein stain, the concrete at this location was not carbonated.

Core C2 Summary of Analysis

The core was approximately 280 mm long by 95 mm in diameter and arrived in two pieces. The core was separated along an angular fracture at a depth of one to 50 mm. The

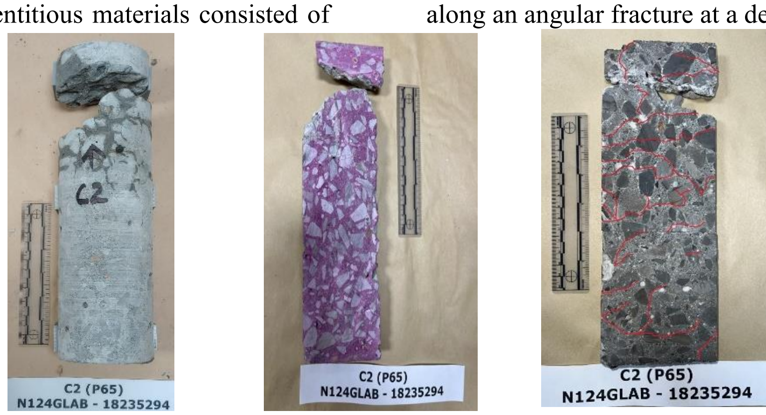

a) b) c)

Figure 5 a) Core C2 as received, b) sawn surface after the application of phenolphthalein stain indicating no carbonation. and c) sawn and polished surface. Fractures noted in red.

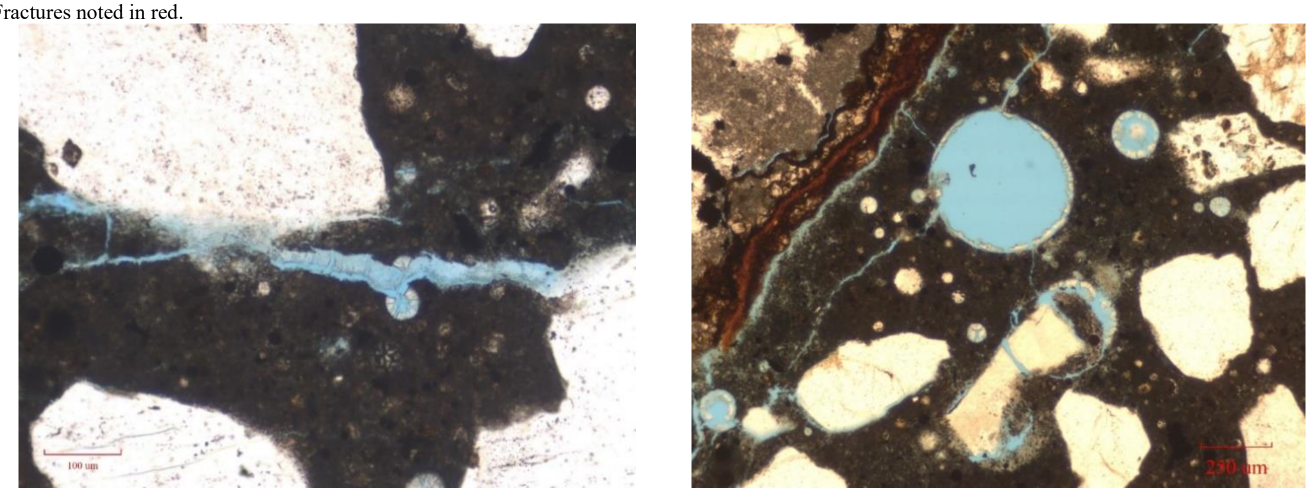

a) b)

Figure 6 a) Core C2 photomicrograph of ettringite filled fractures that have been displaced by continued widening of fractures. Plane polarized light. b) photomicrograph of fracturing and ettringite linings. Plane polarized light.

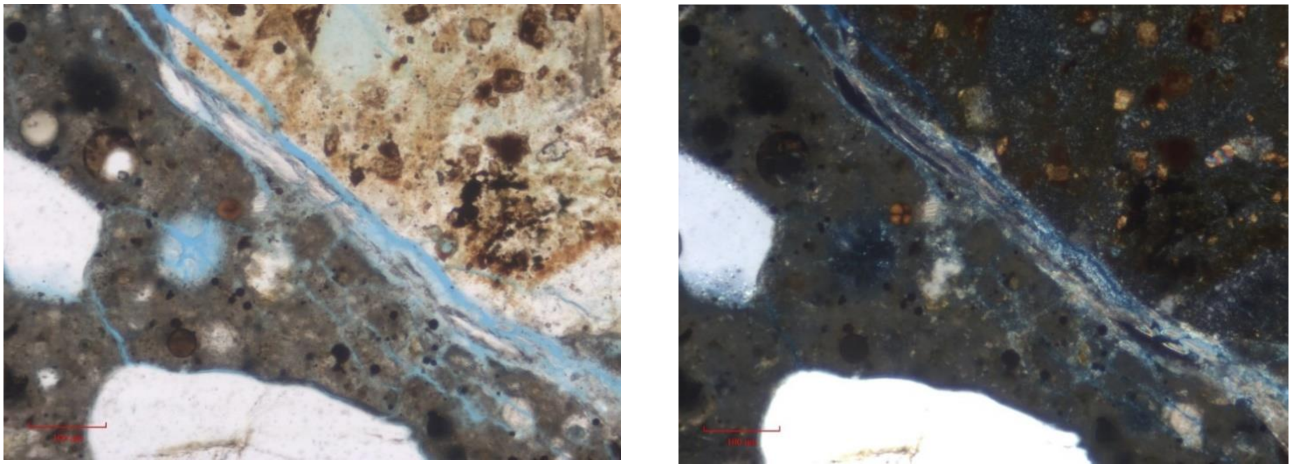

a) b)

Figure 7 a) Core C2 photomicrograph of alkali silica gel (ASR) filled fractures. Plane polarized light. b) photomicrograph of alkali silica gel (ASR) filled fractures. Cross polarized light.

top surface was sandy and exhibited a network of variably oriented fractures which extended to a depth of approximately 127 mm. The surface expression of these fractures was notably darker than the remainder of the surface. A network of fine, interior fractures was also observed throughout, illustrated in Figures 5 to 7. The core was full depth and terminated at an asphalt base with no steel reinforcement or wire mesh. Coarse and fine aggregates were similar to those observed in Core C1 in both size and composition.

Core C2 Summary of Analysis

The core was approximately 280 mm long by 95 mm in diameter and arrived in two pieces. The core was separated along an angular fracture at a depth of one to 50 mm. The top surface was sandy and exhibited a network of variably oriented fractures which extended to a depth of approximately 127 mm. The surface expression of these fractures was notably darker than the remainder of the surface. A network of fine, interior fractures was also observed throughout, illustrated in Figures 5 to 7. The core was full depth and terminated at an asphalt base with no steel reinforcement or wire mesh. Coarse and fine aggregates were similar to those observed in Core C1 in both size and composition

Drilled surfaces exhibited minor amounts of entrained air. Total air content was 4.6%. More than half of the air (2.4%) was entrapped air. Air distribution appeared moderately even throughout, and no honeycombing nor coalescing voids were visibly apparent. Minor irregularly shaped voids were observed. The largest air void was a "bug hole" approximately 22 mm in size. Void fillings were common, with most consisting of calcium hydroxide and calcium carbonate, as well as ettringite.

The matrix was hard and moderately dense. The matrix was dark greenish gray (Munsell color 10Y 4/1) and uniform in color when wet. Cementitious materials consisted of moderately hydrated Portland cement and minor fly ash. Slag cement was not apparent. Aggregate-matrix bonds were strong, with the concrete breaking predominantly through the coarse aggregate when struck by a hammer. Calcium hydroxide was observed in only minor quantities in the matrix and along matrix/aggregate interfaces. Surface micro-fracturing was not significant and randomly oriented. Discontinuous micro-fracturing was observed throughout the interior. Trace alkali-silica gel was observed as fillings/linings in some interior microfracture margins. Moderate to significant ettringite was observed as void fillings and linings. Based on the application of phenolphthalein stain, the concrete at this location was not carbonated

Core C3 Summary of Analysis

The core was approximately 260 mm long by 95 mm in diameter. The core was received intact, with no macroscopic fractures, illustrated in Figures 8 and 9. The top surface exhibited some wear and was sandy with minor exposed coarse aggregate. The core appeared to have been broken off at the bottom. No steel reinforcement or wire mesh was observed. Aggregate materials appeared to be similar to those in the previous two cores.

Drilled surfaces exhibited minor amounts of air. Total air content was 3.9%. More than half of the air (2.3%) was entrapped air. Air distribution appeared moderately even throughout, and no honeycombing nor coalescing voids were visibly apparent. Minor irregularly shaped voids were observed. The largest air void was approximately 6 mm in size. Void fillings were common, with most consisting of calcium hydroxide and calcium carbonate, as well as ettringite.

The matrix was hard and moderately dense. The matrix was greenish gray in color (Munsell color 10Y 5/1) and uniform in color when wet. Cementitious materials were similar to those in the previous samples. Aggregate matrix bonds were moderate, with the concrete breaking predominantly, though not entirely, through the coarse aggregate when struck by a hammer. Micro-fractures were abundant, and many of the fractures contained calcium hydroxide and/or calcium carbonate. The micro-fractures appeared to be roughly oriented at 45 degrees to the core axis. Calcium hydroxide was also observed in minor quantities in the matrix and along matrix/aggregate interfaces. Based on the application of phenolphthalein stain, the concrete at this location was not carbonated.

4. Findings and Conclusions

A forensic investigation was conducted to evaluate the causes of deterioration in the concrete apron in a case study located in Nashville, Tennessee. The investigation involved detailed engineering observations, pavement condition surveys, and petrographic examinations of extracted concrete cores. The primary objective of this study was to assess the nature and extent of the distresses observed in the concrete apron and to provide recommendations for appropriate rehabilitation measures. The key findings and conclusions from the investigation are summarized as follows:

- The concrete represented by the examined cores exhibited similar composition and material characteristics. The concrete was generally well-proportioned, well-mixed, and well-consolidated, with a maximum coarse aggregate size of 19 mm consisting of crushed micritic limestone and fine aggregate composed primarily of natural sand. Cementitious materials included moderately hydrated Portland cement with minor quantities of unhydrated fly ash.

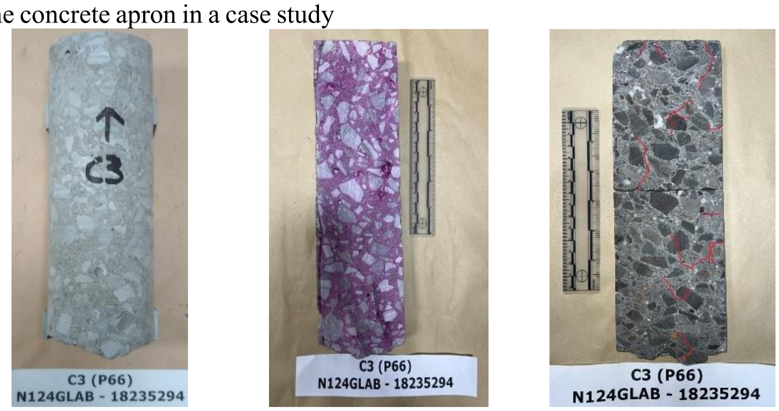

a) b) c)

Figure 8 a) Core C3 as received, b) sawn surface after the application of phenolphthalein stain indicating no carbonation, and c) sawn and polished surface. Fractures noted in red.

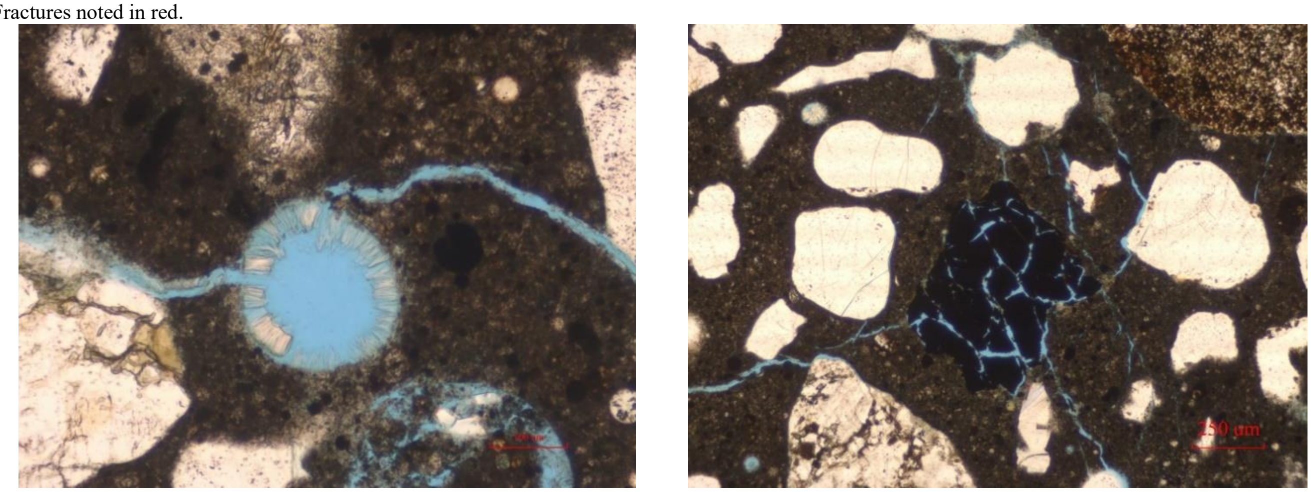

a) b)

Figure 9 a) Core C3 photomicrograph of ettringite lined voids and nearby fracture. Plane polarized light. b) photomicrograph of network of interior fracturing. Plane polarized light.

No slag cement was identified in the concrete matrix. The measured total air contents ranged from 3.9% to 5.2%, with the majority of the air in cores C2 and C3 consisting of entrapped air rather than entrained air. Air void spacing factors exceeded the ACI recommended maximum value of 0.2032 mm for optimal freeze-thaw durability. The distribution of air voids was generally uniform, with no evidence of honeycombing or coalescing voids.

- The petrographic analysis identified moderate to abundant ettringite, calcium hydroxide, and alkali-silica gel (ASR) in varying degrees within the concrete matrix. These materials were commonly observed as void fillings and along fracture surfaces. Calcium hydroxide was also frequently present along aggregate-matrix boundaries, suggesting ongoing chemical reactions and possible microstructural weakening. While evidence of ASR and secondary ettringite formation was observed, their presence was primarily confined to voids and fractures, indicating that they were not the dominant cause of the observed deterioration. The high air void spacing factors, which exceeded the ACI recommended limits, indicate that the concrete is susceptible to freeze-thaw damage. However, the fracture patterns observed in Core C2, including angular fractures and interior micro-fracturing, were not typical of distress caused solely by saturated freezing and thawing, suggesting that other mechanisms may also be contributing to the observed deterioration.
- The application of phenolphthalein stain to the core surfaces confirmed that the concrete was not carbonated. The absence of carbonation suggests that the chemical stability of the concrete matrix has not been compromised by carbon dioxide infiltration. The combination of distress patterns, the presence of ettringite and ASR, and the high air void spacing factors suggest that the observed deterioration is likely the result of multiple interacting mechanisms. Freeze-thaw damage due to inadequate air entrainment appears to be a primary contributing factor, with secondary contributions from possible sulfate attack (secondary ettringite formation) and ASR-related microstructural damage. However, the extent of ASR and sulfate attack appears to be limited and does not fully account for the observed distress patterns.
- Based on the findings, targeted repair strategies should address both the freeze-thaw susceptibility and the underlying chemical reactions within the concrete matrix. Improving air entrainment and implementing protective surface treatments may enhance the concrete's resistance to freeze-thaw cycles. Further evaluation of the sulfate and ASR activity, including long-term monitoring and potential mitigation measures, such as treating the surface with a solution of lithium nitrate, is also recommended to prevent future deterioration (Thomas et al, 2007). However, current studies have indicated limitations on the use of lithium nitrate treatment. Very little lithium penetrates below 25 to 50 mm unless the concrete is heavily cracked, and its ability to suppress ASR expansion is questionable Before treating a structure with lithium-based compounds it should be determined that the main cause is ASR, as the lithium treatment is unlikely to cure deterioration related to freeze-thaw damage, corrosion of embedded steel or even alkali-carbonate reaction. Further, there remains the potential for continued expansion and damage due to ASR, and the treatment will not "repair" any damage that has already occurred.
- In conclusion, the observed deterioration in the concrete apron is likely the result of a combination of inadequate freeze-thaw resistance, localized ASR, and possible sulfate attack. The prolific observation of D-cracking (i.e., cracking resulting from freeze-thaw) within the concrete apron is of significant concern as D-cracking is a terminal condition. Once it starts there's no known cure. D-cracking typically begins at the bottom of the concrete slab due to the natural accumulation of water under pavements in the base and subbase layers. The aggregate may eventually become saturated and crack from cycles of freezing and thawing and the cracking progresses upward to the surface of the slab where expansion, scaling and crumbling of the concrete surface occurs. The only way to prevent D-cracking is to avoid using coarse aggregates susceptible to freezing and thawing deterioration.

Acknowledgments

The authors would like to acknowledge the petrographers in the rock and soil mechanics laboratory facility in the Terracon Consultants, Inc. office in Cincinnati, Ohio for their help in providing the data in this research. The opinions, findings, and conclusions presented herein are those of the authors and do not necessarily reflect any sponsors.

Conflict of interest

The authors declare that they have no conflict of interest.

References

[1] ASTM International. "Standard Practice for Petrographic Examination of Hardened Concrete." ASTM C856-22 (2022).

[2] Fournier, B. and M. A. Bérubé. "Alkali-aggregate reaction in concrete: a review of basic concepts and engineering implications." Canadian Journal of Civil Engineering 27.2 (2000): 167–191.

[3] Grattan-Bellew, P. E. "Microstructural investigation of deteriorated concrete." Cement and Concrete Composites 17.1 (1995): 23–32.

[4] Abu-Farsakh, M., H. Alimohammadi, and L. N. Mohammad. "Finite Element Analysis to Evaluate the Benefits of Geosynthetic Reinforcement in Flexible Pavements Over Weak Subgrade for Low-Volume Traffic Roads." Transportation Research Board Conference 99th Annual Meeting (2020). https://annualmeeting.mytrb.org/OnlineProgramArchive/Details/12333

[5] Alimohammadi, H. and B. Izadi Babokani. "Finite element electrodynamics modeling of a layered piezoelectric composite shell with different materials by using numerical software." ISSS Journal of Micro and Smart Systems (2020). https://doi.org/10.1007/s41683-020-00052-3

[6] Poole, A. B. "Introduction to alkali-aggregate reaction in concrete." Proceedings of the International Conference on Alkali-Aggregate Reaction (1991): 1–19.

[7] Alimohammadi, H. "A framework for evaluation of existing pavement conditions and selection of feasible maintenance/rehabilitation alternatives; a case study in some routes of Livingston Parish in the state of Louisiana." SN Applied Sciences 2.2 (2020): 289. https://doi.org/10.1007/s42452-020-1999-6

[8] Zheng, G., H. Alimohammadi, J. Zheng, and V. R. Schaefer. "Effectiveness of Geosynthetics in the Construction of Roadways: A Full-Scale Field Studies Review." International Foundations Congress and Equipment Expo 2021 (2021): 223–232. https://doi.org/10.1061/9780784483411.022

[9] Sanchez, L. F. M., B. Fournier, and M. Jolin. "Evaluation of damage in concrete affected by ASR: A comparison of damage rating index and residual expansion tests." Construction and Building Materials 157 (2017): 139–151.

[10] Alimohammadi, H., V. R. Schaefer, J. Zheng, and H. Li. "Performance evaluation of geosynthetic reinforced flexible pavement: a review of full-scale field studies." International Journal of Pavement Research and Technology (2020). https://doi.org/10.1007/s42947-020-0019-y

[11] Alimohammadi, H., V. Schaefer, J. Ashlock, A. Buss, C. Rutherford, and B. Li. "Effectiveness of geogrids in roadway construction; determine a granular equivalent (G.E.) factor."

[12] Shehata, M. H. and M. D. A. Thomas. "The effect of fly ash composition on the expansion of concrete due to alkali–silica reaction." Cement and Concrete Research 30.7 (2000): 1063–1072.

[13] Alimohammadi, H., J. Zheng, A. Buss, V. R. Schaefer, C. Williams, and G. Zheng. "Field and simulated rutting behavior of hot mix and warm mix asphalt overlays." Construction and Building Materials 265 (2020): 120366. https://doi.org/10.1016/j.conbuildmat.2020.120366

[14] Kalhor, K., R. Ghasemizadeh, L. Rajic, and A. Alshawabkeh. "Assessment of groundwater quality and remediation in karst aquifers: A review." Groundwater for Sustainable Development 8 (2019): 104–121. https://doi.org/10.1016/j.gsd.2018.10.004

[15] Alimohammadi, H. and J. Tahat. "A case study experimental pile load testing (PLT) for evaluation of driven pile behaviors." Arabian Journal of Geosciences 15.9 (2022): 1–11. https://doi.org/10.1007/s12517-022-10176-5

[16] Alimohammadi, H. and J. Tahat. "A Case Study Pile Load Testing (PLT) to Evaluate Driven Pile Behaviors." Indian Geotechnical Journal 52 (2022): 959–968. https://doi.org/10.1007/s40098-022-00613-3

[17] Stark, D. "The moisture condition of field concrete exhibiting alkali-silica reactivity." Cement, Concrete, and Aggregates 13.1 (1991): 81–89.

[18] Alimohammadi, H., M. Amirmojahedi, and J. N. Tahat. "A Case History of Application of Deep Compaction Method with Comparison to Different Ground Improvement Techniques." Transportation Infrastructure Geotechnology (2022): 1–26. https://doi.org/10.1007/s40515-022-00229-3

[19] Satvati, S., H. Alimohammadi, M. A. Rowshanzamir, and S. M. Hejazi. "Evaluation the Effects of Geosynthetic Reinforcement on Bearing Capacity of Shallow Foundations in Soil Slopes." 101st Transportation Research Board Annual Meeting (2022). https://annualmeeting.mytrb.org/OnlineProgram/Details/17240

[20] Alimohammadi, H., V. R. Schaefer, J. Zheng, C. T. Jahren, G. Zheng, and D. White. "Effectiveness of Geotextiles/Geogrids in Roadway Construction; Determine a Granular Equivalent (GE) Factor." Minnesota Department of Transportation (2021). https://www.dot.state.mn.us/research/reports/2021/202126.pdf

[21] Alimohammadi, H., V. Schaefer, J. Zheng, D. J. White, and G. Zheng. "A State-of-the-art Large-scale Laboratory Approach to Evaluating the Effectiveness of Geogrid Reinforcement in Flexible Pavements." Geosynthetics Conference 2021 (2021). https://osf.io/2d4gk/

[22] Alimohammadi, H., A. Buss, V. R. Schaefer, J. Zheng, and G. Zheng. "Finite element viscoelastic simulations of rutting behavior of hot mix and warm mix asphalt overlay on flexible pavements." International Journal of Pavement Research and Technology (2020). https://doi.org/10.1007/s42947-020-0057-5

[23] Alimohammadi, H., J. Zheng, A. Buss, V. R. Schaefer, and G. Zheng. "Rutting Performance Evaluation of Hot Mix Asphalt and Warm Mix Asphalt Mixtures by Using Dynamic Modulus, Hamburg Wheel Tracking Tests, and Viscoelastic Finite Element Simulations." International Conference on Transportation and Development 2020 (2020): 83–94. https://doi.org/10.1061/9780784483183.009

[24] Zheng, J., H. He, and H. Alimohammadi. "Three-dimensional Wadell roundness for particle angularity characterization of granular soils." Acta Geotechnica 9 (2020). https://doi.org/10.1007/s11440-020-01004-9

[25] Alimohammadi, H., K. Yashmi Dastjerdi, and M. Lotfollahi Yaghin. "The study of progressive collapse in dual systems." Civil and

Environmental Engineering 16 (2020). https://doi.org/10.2478/cee-2020-0009
[26] Alimohammadi, H., J. Zheng, A. Buss, V. Schaefer, C. Williams, and G. Zheng. "Performance Evaluation of Hot Mix and Warm Mix Asphalt Overlay Layers Based on Field Measurements and Finite Element Viscoelastic Simulations." Transportation Research Board Conference 99th Annual Meeting (2020). https://annualmeeting.mytrb.org/OnlineProgramArchive/Details/13743
[27] Alimohammadi, H., A. Hesaminejad, and M. Lotfollahi Yaghin. "Effects of different parameters on inelastic buckling behavior of composite concrete-filled steel tubes." International Research Journal of Engineering and Technology 6.12 (2019). https://www.researchgate.net/publication/337856971_Effects_of_different_parameters_on_inelastic_buckling_behavior_of_composite_concrete-filled_steel_tubes
[28] Stark, D. and D. Gress. "Effects of alkali-silica reaction on concrete pavements." Transportation Research Record 1448 (1994): 54–61.
[29] Alimohammadi, H., M. D. Esfahani, and M. L. Yaghin. "Effects of openings on the seismic behavior and performance level of concrete shear walls." International Journal of Engineering and Applied Sciences (2019). https://www.researchgate.net/publication/337596926_Effects_of_openings_on_the_seismic_behavior_and_performance_level_of_concrete_shear_walls
[30] Alimohammadi, H. "Finite element analysis of a Piezoelectric layered plate with different materials." International Journal of Engineering and Applied Sciences 6.7 (2019). https://doi.org/10.31873/IJEAS.6.8.2019.09
[31] Thomas, M. D. A., B. Fournier, and K. J. Folliard. "Report on the diagnosis, prognosis, and mitigation of alkali-silica reaction (ASR) in transportation structures." FHWA Report No. FHWA-HIF-13-019 (2013).
[32] Alimohammadi, H. and M. Lotfollahi Yaghin. "Study on the Effect of the Concentric Brace and Lightweight Shear Steel Wall on Seismic Behavior of Lightweight Steel Structures." International Research Journal of Engineering and Technology 6.8 (2019): 1358–1362. https://www.researchgate.net/publication/336846191_Study_on_the_Effect_of_the_Concentric_Brace_and_Lightweight_Shear_Steel_Wall_on_Seismic_Behavior_of_Lightweight_Steel_Structures
[33] Alimohammadi, H. and M. Abu-Farsakh. "Finite Element Parametric Study on Rutting Performance of Geosynthetic Reinforced Flexible Pavements." Transportation Research Board 98th Annual Meeting (2019). https://trid.trb.org/view/1572248
[34] Alimohammadi, H. and A. Memon. "A Case Study of Mechanically Stabilized Earth (MSE) Retaining Wall Failure in the State of Tennessee; Recommendations for Future Design and Constructions." OSF Preprints (2023). https://doi.org/10.31219/osf.io/uy76r
[35] Alimohammadi, H., V. R. Schaefer, J. Zheng, and D. White. "A full-scale field approach for evaluating the geogrid reinforcement effectiveness in flexible pavement." 22nd International Conference on Soil Mechanics and Geotechnical Engineering (2022).
[36] Alimohammadi, H. and J. Tahat. "A State-of-The-Art Evaluation of Driven Pile Behaviors Using Pile Load Testing (PLT)." 101st Transportation Research Board Annual Meeting (2022). https://annualmeeting.mytrb.org/OnlineProgram/Details/17332
[37] Alimohammadi, H. "Effectiveness of Geogrids in Roadway Construction: Determine a Granular Equivalent (G.E.) Factor." Iowa State University (2021). https://www.proquest.com/docview/2576937127
[38] Alimohammadi, H. "Rutting Behavior of Laboratory, Field, and Finite Element Simulated Hot Mix and Warm Mix Asphalt Overlays." Iowa State University (2021).
[39] Thomas, M. D. A., B. Fournier, K. J. Folliard, J. H. Ideker, and Y. Resendez. "The Use of Lithium to Prevent or Mitigate Alkali-Silica Reaction in Concrete Pavements and Structures." FHWA Report No. FHWA-HRT-06-113 (2007).
[40] Alimohammadi, H. and M. Abu-Farsakh. "Evaluating Geosynthetic Reinforcement Benefits of Flexible Pavement." 8th Annual Graduate Student Research Conference (2019).
[41] Alimohammadi, H. and A. Memon. "Failure Analysis and Recommendations For Improving Mechanically Stabilized Earth (MSE) Retaining Wall Design and Construction: A Case Study from Tennessee, USA." Transportation Research Board 103rd Annual Meeting (2024).
[42] Alimohammadi, H. and A. Memon. "A Case Study of Failure Analysis of an MSE Retaining Wall in Tennessee: Lessons Learned and Recommendations for Reconstruction." OSF Preprints (2023). https://doi.org/10.31219/osf.io/nf95e
[43] Alimohammadi, H. and A. Memon. "Forensic Investigation of Slope Stability Issues and Design Practices: A Case Study in Nashville, Tennessee." OSF Preprints (2023). https://doi.org/10.31219/osf.io/9yx82
[44] Alimohammadi, H. and J. Tahat. "Evaluation of Driven Pile Using Pile Load Testing: A Case Study in the State of Ohio." Geo-Congress 2024 (2024).
[45] Alimohammadi, H. and J. Tahat. "Evaluating Driven Pile Behaviors Through Case Study Experimental Pile Load Testing (PLT)." 48th Annual Conference on Deep Foundations (2023).
[46] Satvati, S., H. Alimohammadi, M. Rowshanzamir, and S. M. Hejazi. "Bearing Capacity of Shallow Footings Reinforced with Braid and Geogrid adjacent to Soil Slope." International Journal of Geosynthetics and Ground Engineering 6.41 (2020). https://doi.org/10.1007/s40891-020-00226-x
[47] Alimohammadi, H., J. Zheng, A. Buss, V. R. Schaefer, and G. Zheng. "Evaluating the Rutting Performance of Hot Mix Asphalt and Warm Mix Asphalt Mixtures by Using Viscoelastic Finite Element Simulations." International Conference on Transportation and Development 2020 (2020). https://doi.org/10.1061/9780784483183.009
[48] Swamy, R. N. "The alkali-silica reaction in concrete." Spon Press (2002).
[49] Alimohammadi, H., J. Zheng, V. Schaefer, J. Siekmeier, and R. Velasqueze. "Evaluation of Geogrid Reinforcement of Flexible Pavement Performance: A Review of Large-Scale Laboratory Studies." Transportation Geotechnics (2020). https://doi.org/10.1016/j.trgeo.2020.100471
[50] Alimohammadi, H. and B. Izadi Babokani. "Finite element electrodynamics modeling of a layered piezoelectric composite shell with different materials by using numerical software." ISSS Journal of Micro and Smart Systems (2020). https://doi.org/10.1007/s41683-020-00052-3
[51] Alimohammadi, H. and M. D. Esfahani. "Investigating the Opening Effect of Constant Cross-Section and Various Forms of Seismic Behavior and Performance levels in Concrete Shear Walls." First international conference on civil engineering architecture and stable urban development (2015).
[52] Alimohammadi, H. and M. Lotfollahi Yaghin. "Evaluation of seismic properties of light weight concentric brace on seismic behavior of light weight steel structures." National Conference in applied civil engineering and new advances (2014).
[53] Alimohammadi, H. and M. Lotfollahi Yaghin. "Evaluation of seismic properties of lightweight steel frames coated with lightweight steel shear wall." First international conference on urban

development based on new technologies and 4th national conference on urban development (2014).

[54] Wang, X., J. Lai, S. He, and Y. Wang. "Karst geology and mitigation measures for hazards during metro system construction in Wuhan, China." Natural Hazards 103 (2020): 2905–2927. https://doi.org/10.1007/s11069-020-04108-3

[55] Song, K-I., G-C. Cho, and S-B. Chang. "Identification, remediation, and analysis of karst sinkholes in the longest railroad tunnel in South Korea." Engineering Geology 135–136 (2012): 92–105. https://doi.org/10.1016/j.enggeo.2012.02.018

[56] Gracia, A., F. J. Torrijo, J. Garzón-Roca, M. Pérez-Picallo, and O. Alonso-Pandavenes. "Identification and Mitigation of Subsidence and Collapse Hazards in Karstic Areas: A Case Study in Alcalá de Ebro (Spain)." Applied Sciences 13.9 (2023): 5687. https://doi.org/10.3390/app13095687

[57] Goldscheider, N. "A holistic approach to groundwater protection and ecosystem services in karst terrains." Carbonates and Evaporites 34 (2019): 1241–1249. https://doi.org/10.1007/s13146-019-00492-5

[58] Alimohammadi, H. "Shallow Foundations and Deep Foundations; Drilled Piers, Aggregate Piers and Stone Columns; Design Recommendations, Construction Considerations, and Performance." Journal of Civil Engineering Researchers 6.3 (2024): 18–28. https://doi.org/10.61186/JCER.6.3.18

[59] Alimohammadi, H. and A. Memon. "Comprehensive Sinkhole Mitigation: A Case Study and Application of Compaction Grouting in Karstic Environments in the State of Tennessee, USA." Journal of Civil Engineering Researchers 6.2 (2024): 1–16. https://doi.org/10.61186/JCER.6.2.1

[60] Alimohammadi, H. and A. Memon. "Mitigation of A Sinkhole in Nashville, Tennessee: A Case Study with Compaction Grouting Approach." OSF Preprints (2024). https://osf.io/preprints/osf/63nyv_v1

[61] Alimohammadi, H. and A. Memon. "Failure Analysis and Recommendations For Improving Mechanically Stabilized Earth (MSE) Retaining Wall Design and Construction: A Case Study from Tennessee, USA." Transportation Research Board 103rd Annual Meeting (2024).

[62] Alimohammadi, Hossein and Behrooz Izadi Babokani. "Finite element electrodynamics modeling of a layered piezoelectric composite shell with different materials by using numerical software." ISSS Journal of Micro and Smart Systems 9.1 (2020): 79–88. https://doi.org/10.1007/s41683-020-00052-3

J-Researchers

Journal of Civil Engineering Researchers

Journal homepage: www.journals-researchers.com

2D Equivalent Linear Seismic Site Response Analysis in SBFEM

Morteza Iraniparast, [a] M. Iman Khodakarami [a,*]

[a] *Faculty of Civil Engineering, Semnan university, Semnan, Iran*

ABSTRACT

Understanding the dynamic behavior of soil layers under seismic loading is pivotal for accurate seismic design and risk assessment. This study conducts a two-dimensional equivalent linear site response analysis using the Scaled Boundary Finite Element Method with Rayleigh damping to enhanced modeling accuracy. SBFEM combines the advantages of finite and boundary element methods, offering high efficiency in simulating wave propagation and stress concentrations in semi-infinite domains. A MATLAB implementation of the method was validated against previous studies, confirming consistent accuracy across various soil profiles and seismic scenarios. The method demonstrates convergence, accuracy, and stability, requiring fewer elements due to boundary-only discretization. This reduces both computational cost and time while accurately modeling the infinite domain condition. The findings highlight the method's effectiveness for site response analysis under diverse seismic inputs and layered soil configurations, combining the equivalent linear method with SBFEM as a robust and practical tool for dynamic geotechnical applications.

ARTICLE INFO

Received: May 21, 2025
Accepted: August 20, 2025

Keywords:
Seismic Site Response Analysis
Equivalent Linear
Layered Semi-Infinite Soil
Scaled Boundary Finite Element Method (SBFEM)
Two-dimensional

DOI: 10.66224/JCER.7.3.52
DOR: 20.1001.1.2538516.2025.7.3.5.5

1. Introduction

1.1. Site Response Analysis

Site response analysis is an essential part of geotechnical and earthquake engineering because it evaluates the changes in seismic waves as they propagate through soil and rock layers; therefore, influencing the intensity and traits of ground shaking during earthquakes.

It uses linear, equivalent linear, and non-linear methods for different seismic intensities and soil conditions [1]. Boore [2] discusses the challenges and prospects in predicting site responses, highlighting the complexities and uncertainties in modeling seismic behaviors accurately. Linear methods are used for low-intensity earthquakes and assume elastic soil behavior [3]. In contrast, the equivalent linear method approximates soil's non-linear response for various scenarios [4]. Non-linear methods update soil dynamics at each time step, accurately depicting soil actual stress-strain behavior during high-intensity events [5,6].

For these problems, analytical, semi-analytical, and numerical methods are used in time and frequency domains [7,8].

* Corresponding author. Tel.: +989125314408; e-mail: khodakarami@semnan.ac.ir.

The seismic source, soil complexity, and analysis goals determine the model's dimensionality from 1D to 3D, which affects soil behavior under seismic loads [8-12].

Damping is crucial in site response analysis for capturing energy dissipation mechanisms within soil layers under seismic loads. It significantly reduces seismic energy, affecting both the amplitude and duration of surface ground motion. By incorporating damping into models, predictions of soil behavior during seismic events become more accurate, reflecting the natural energy loss from hysteresis and viscous behavior in soil materials [7,12]. Properly calibrated damping parameters yield more realistic ground motion estimates, particularly vital for high-intensity seismic events [13]. Park and Hashash [14] highlight the importance of precise damping modeling in the context of non-linear time domain site response analysis.

1.2. Overview of the Scaled Boundary Finite Element Method for Site Response Analysis

Introduced by Wolf and Song in 1996 [15], the Scaled Boundary Finite Element Method (SBFEM) evolved from the Consistent Infinitesimal Finite Element Cell Method. SBFEM adeptly handles site response analysis challenges, effectively modeling complex soil profiles and seismic interactions. It adjusts for varying soil properties, dimensions, and boundaries, ensuring precise analysis [16, 17]. SBFEM combines the advantages of Finite Element Method (FEM) and Boundary Element Method (BEM), reducing computational effort by discretizing only domain boundaries, unlike traditional finite element methods [18]. This semi-analytical method accurately captures stress concentrations and wave propagation, ideal for dynamic geotechnical earthquake analysis [16, 17].

Zhang, Wegner, and Haddow [19] utilized SBFEM in a comprehensive three-dimensional dynamic soil-structure interaction analysis in the time domain, providing insights into interactions between soil layers and structures during seismic events. Birk, Prempramote, and Song [20] enhanced SBFEM's utility in time-domain analyses of unbounded domains by introducing an improved high-order transmitting boundary that substantially reduces computational errors from wave reflections at artificial boundaries. Further advancements by Birk, Chen, Song, and Du [21] demonstrated the method's efficacy in transient wave propagation, which broadened its applications in industrial settings. Bazyar and Song [10] developed its applications to transient wave scattering, improving predictions of seismic wave behavior across various soils. Their earlier work, Bazyar and Song [22], expanded its use to non-homogeneous domains, thus enhancing the accuracy of seismic analyses. Additionally, Chen, Birk, and Song [23] extended SBFEM's capabilities to anisotropic soils using a displacement unit-impulse-response-based formulation, pivotal for accurately modeling how anisotropic soil properties affect wave propagation. Yaseri, Bazyar, and Hataf [24] further showcased SBFEM's versatility by applying a 3D coupled scaled boundary finite element/finite element analysis to study ground vibrations induced by underground train movements, demonstrating the method's applicability beyond traditional earthquake engineering contexts.

1.3. Equivalent Linear Analysis

Idriss and Seed [25] first proposed the equivalent linear method for analyzing site response, approximating a non-linear response through a linear analysis of soil layer characteristics during earthquake motions. Subsequently, Schnabel [26], Idriss and Sun [27], and Ordonez [28] implemented the method, adapting it to approximate the nonlinear soil behaviors commonly encountered in earthquake engineering. Various relationships for modulus reduction and damping suitable for equivalent-linear analyses are available, including those by Seed [12], Vucetic and Dobry [29], EPRI [30], Ishibashi and Zhang [31], Darendeli [32], and Zhang, Andrus, and Juang [33].

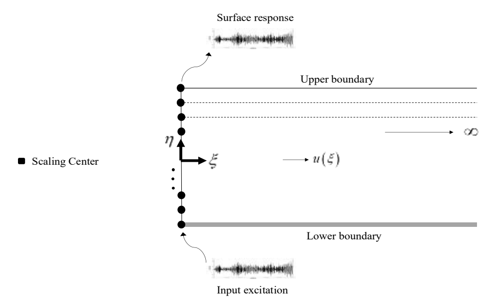

Figure 1. SBFEM applied to semi-infinite layer

In this research, we address the critical challenge of predicting the surface response to earthquake-induced ground motions, which is pivotal for designing resilient structures in seismically active regions. Our approach employs the SBFEM for equivalent linear site response analysis, a sophisticated computational method that models seismic wave propagation in two-dimensional, layered, unbounded domains. This method improves accuracy by incorporating Rayleigh damping and discretizing vertical boundaries with line elements (Fig. 1), effectively simulating real-world seismic conditions. Our research methodology includes a comprehensive comparison of simulated responses—such as acceleration time histories, spectra, and sublayer shear strain and modulus—with actual earthquake data from events like Parkfield and Nahanni. The expected results will underscore the model's precision in capturing complex seismic behaviors and its effectiveness compared to traditional methods, providing insights into both the strengths and potential limitations of SBFEM in earthquake engineering applications.

2. Theoretical Foundations

2.1. Formulation of Elastodynamic Equations for Soil Media

The equation of motion is derived by considering an infinitesimal element of the solid medium:

$$\frac{\partial \sigma_x}{\partial x}+\frac{\partial \tau_{xy}}{\partial y}+\frac{\partial \tau_{zx}}{\partial z}+p_x=\rho\ddot{u}_x \qquad (1)$$
$$\frac{\partial \tau_{xy}}{\partial x}+\frac{\partial \sigma_y}{\partial y}+\frac{\partial \tau_{yz}}{\partial z}+p_y=\rho\ddot{u}_y$$
$$\frac{\partial \tau_{zx}}{\partial x}+\frac{\partial \tau_{yz}}{\partial y}+\frac{\partial \sigma_z}{\partial z}+p_z=\rho\ddot{u}_z$$

whereσ_x,σ_y , andσ_z are normal stresses in the x,y, and z directions; τ_{xy},τ_{zx}, τ_{yz}, and τ_{zx} are shear stresses p_x,p_y, and p_z are the body forces; ρ is the mass density. For $\ddot{u}_x$, $\ddot{u}_y$, and $\ddot{u}_z$, the double dots (̈) indicate the accelerations, i.e. the second time derivatives of displacements. The governing equations for elastodynamics in frequency domain are expressed in Soliman [34].

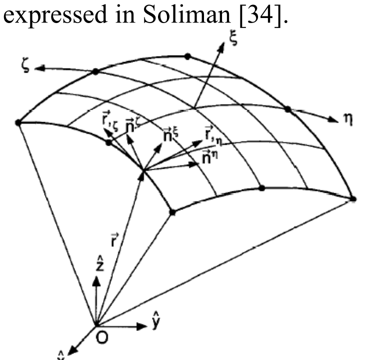

Figure 2. Curvilinear and Cartesian coordinates with surface elements

2.2. Coordinate Transformation from Cartesian to Local Systems

To simplify the governing equations of a medium, the interface is discretized using surface elements, where the points of the elements are related to each other with assumed shape functions. The local coordinates are more suitable, and Cartesian coordinates can translate into these coordinates. Therefore, Curvilinear coordinates are introduced: ξ (radial direction) extends from the origin outward, η and ζ(circumferential directions) run parallel to the interface (see Fig. 2 for 2D layered medium). The discretization on the interface, resulting in exact solutions in the radial direction and approximate solutions in the circumferential directions [23, 34].

2.3. Discretization Techniques for Motion Equations

After getting the equation in local coordinate, the governing equation should be solved numerically. To derive a finite-element approximation, the weighted-residual technique is applied to the equilibrium equation [17]. Finally, the SBFEM equation in displacement can be obtained [34].

2.4. Derivation of Scaled Boundary Finite Element Equation in time-domain

After getting the SBFEM equation in displacement, the values of dynamic stiffness need to be obtained too. First of all, internal nodal forces $\{Q(\xi)\}$ should be defined, and for unbounded domain, external nodal force $\{R(\xi)\}$ applied, which is equal to $\{Q(\xi)\}$ with opposite direction. So, the relation between these two forces with respect to the dynamic stiffness S^{∞}(∞ stands for infinity) as follows:

$$\{R(\xi)\}=-\{Q(\xi)\}=[S^{\infty}(\omega,\xi)]\{u(\xi)\}-\{R_F(\xi)\} \qquad (2)$$

where $\{R_F(\xi)\}$ is the vector of external body forces and boundary traction.

By establishing the relationship between the nodal internal forces and the boundary traction, and employing a weighting function to address approximation errors, the formulation of the dynamic stiffness matrix is derived. Consequently, the SBFEM equation for dynamic stiffness is constructed based on this formulation.

The next step is to express this formulation in the time domain; That process begins by establishing a relationship between two forms of dynamic stiffness: one associated with acceleration response, and the other associated with displacement. After simplification, to transition from the frequency to the time domain, inverse Fourier transformation is applied. Finally, the SBFEM equation in time domain for $\xi=1$ looks like:

$$\int_0^t [m^{\infty}(t-\tau)][m^{\infty}(\tau)]d\tau + \int_0^t\int_0^{\tau}[m^{\infty}(\tau')]d\tau' d\tau\left([e_1]^T-\left(\frac{s+1}{2}\right)[I]\right) + \left([e_1]-\left(\frac{s+1}{2}\right)[I]\right)\int_0^t\int_0^{\tau}[m^{\infty}(\tau')]d\tau' d\tau + \frac{t^3}{6}([e_1][e_1]^T-[e_2]) + t\int_0^t[m^{\infty}(\tau)]d\tau - t[m_0]=[0] \qquad (3)$$

where

$$([U]^T)^{-1}[M_0][U]^{-1} = [m_0] \quad (4)$$
$$([U]^T)^{-1}[E_1][U]^{-1} = [e_1]$$
$$([U]^T)^{-1}[E_2][U]^{-1} = [e_2]$$
$$([U]^T)^{-1}[M^\infty(t,\xi)][U]^{-1} = [m^\infty(t,\xi)]$$

matrices $[E_0(\eta,\zeta)]$, $[E_1(\eta,\zeta)]$ and $[E_2(\eta,\zeta)]$ are the stiffness matrices in a finite element model, and the matrix term $[M_0(\eta,\zeta)]$ is the mass matrix. Decomposing of $[E_0]$ (by using Cholesky decomposition) is:

$$[E_0] = [U]^T[U] \quad (5)$$

where, $[U]$is an upper triangular matrix. Then, inverse matrix of $[E_0]$ is shown below:

$$[E_0]^{-1} = [U]^{-1}[U]^{-T} \quad (6)$$

Also, $[M^\infty(\tau,\xi)]$ is the unit impulse response function for acceleration and $[I]$ is the identity matrix. Where the values of $[m_0]$, $[e_1]$ and $[e_2]$ have been given, the only unknown in this equation is the term $[m^\infty(t)]$ [22,34 and 35].

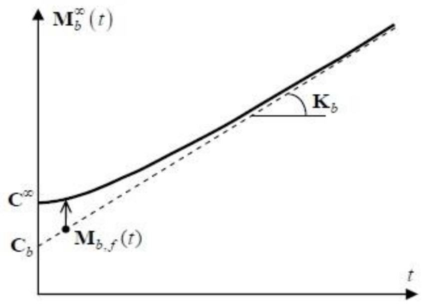

Figure 3. Decomposition of $M_b^\infty(t)$

2.5. Linear Scheme of Obtaining Acceleration Unit-Impulse Response Matrix

The integration of Eq. (10) lacks an analytical solution, and thus discretization in time is required for its numerical evaluation. In the original discretization scheme [15, 22], the acceleration unit-impulse response matrix $[M^\infty(t)]$is assumed to remain constant within the time step. This method is only conditionally stable and necessitates the use of small-time steps. Furthermore, the computation of integrals involving $[M^\infty(t)]$ requires solving a Lyapunov matrix equation at every time step, resulting in a substantial computational burden for large-scale systems.

In the new scheme introduced by Radmanović and Katz [36], a different discretization strategy is adopted wherein the time variation of $[M^\infty(t)]$ is modeled as piecewise linear within each time interval. Additionally, the use of an extrapolation parameter θ enhances the numerical stability of the method, allowing for the use of larger time steps. To further improve computational efficiency, a truncation time is introduced beyond which the $[M^\infty(t)]$is assumed to evolve linearly (Fig. 3). This approach leads to a significant reduction in computational cost.

2.6. Dynamic Response Calculation of Soil Systems

The equation of motion of the soil in the time domain can be written as:

$$[M]\{\ddot{u}(t)\} + [C]\{\dot{u}(t)\} + [K]\{u(t)\} = \{P(t)\} - \{R(t)\} \quad (7)$$

where $[M]$, $[C]$ and $[K]$ represent the mass, damping and stiffness matrices of the soil, $\{\ddot{u}(t)\}$, $\{\dot{u}(t)\}$ and $\{u(t)\}$for acceleration, velocity and displacement respectively, while $\{P(t)\}$ and $\{R(t)\}$ are the applied force and the reaction of the unbounded domain, respectively.

In the SBFEM, the mass matrix is derived from the physical properties of the system's elements, including density and geometric configuration. The stiffness matrix characterizes the system's resistance to deformation and is computed based on material properties such as Young's modulus and Poisson's ratio, along with the geometric arrangement of the elements [16].

The calculation of the Rayleigh damping matrix involves a systematic approach, starting from the computation of eigenvalues and natural frequencies to the final construction of the damping matrix. This method ensures that the dynamic behavior of the system is accurately characterized. The first step is to determine the eigenvalues of the system, which are essential in understanding the dynamic characteristics. Eigenvalues are computed through an eigenvalue analysis of the system matrices, specifically the mass and stiffness matrices. This problem is expressed as:

$$[K]v = \lambda[M]v \quad (8)$$

where λ represents the eigenvalues, and v are the corresponding eigenvectors. The eigenvalues are then used to calculate the natural frequencies ω by taking the square root:

$$\omega = \sqrt{\lambda} \quad (9)$$

Natural frequencies are crucial as they represent the inherent vibrational properties of the system. Once the natural frequencies are obtained, the next step is to determine the Rayleigh damping coefficients, α and β . Rayleigh damping is a proportional damping model where the damping matrix $[C]$ is a linear combination of the mass and stiffness matrices. The coefficients are derived to achieve a specified damping ratio ξ_D at two selected frequencies. The system of equations for α and β is formulated as:

$$\begin{bmatrix} 1 & \omega_1^2 \\ 1 & \omega_2^2 \end{bmatrix} \begin{bmatrix} \alpha \\ \beta \end{bmatrix} = \begin{bmatrix} 2\xi_D \\ 2\xi_D \end{bmatrix} \quad (10)$$

Here, ω_1 and ω_2 are the chosen natural frequencies. Solving this system yields the values for α and β, and with these determined coefficients, the damping matrix $[C]$ can be constructed. The damping matrix is expressed as:

$$[C] = \alpha[M] + \beta[K] \quad (11)$$

This linear combination ensures that the damping characteristics are appropriately distributed within the system, corresponding to the specified damping ratio at the selected frequencies [15, 37].

The interacting force-acceleration relationship for the soil in the time domain can be represented by the convolution integral as [36]:

$$\{R(t)\} = \int [M^{\infty}(\tau)]\{\ddot{u}(t-\tau)\}d\tau \quad (12)$$

In the detailed analysis of seismic response within soil layers, accurately computing the shear strain is crucial for assessing the structural integrity and dynamic behavior of the soil under seismic forces. This process begins with the acquisition of nodal displacements, which are essentially the movement of predefined points within the soil matrix during seismic activity. Each node's displacement is recorded in a two-dimensional space, allowing for the subsequent computation of displacement gradients.

The displacement gradient is a fundamental concept in continuum mechanics, representing the rate of change of displacement across a finite distance within the material. In this analysis, the displacement gradient is mathematically defined by the difference in displacements between adjacent nodes, normalized by the spatial distance between these nodes. This calculation provides a local view of deformation specific to the area around each node.

Following the determination of displacement gradients, the deformation gradient tensor, H, is calculated. This tensor is pivotal in transitioning from the undeformed state to the deformed state of the soil element, encapsulating both rotational and translational deformation components. The tensor is computed as:

$$H = I + \nabla u \quad (13)$$

where I represents the identity matrix and ∇u is the displacement gradient tensor [38]. Subsequently, the Green-Lagrange strain tensor,E, is derived to measure the strain experienced by the soil element relative to its original configuration. The tensor is calculated using as:

$$E = \frac{1}{2}(H^T H - I) \quad (14)$$

where H^T is the transpose of the deformation gradient tensor. This expression captures the quadratic contributions of the deformation, essential for describing strains in scenarios involving displacements and rotations typical in seismic activities. The final step involves extracting the engineering shear strain,γ, from the Green-Lagrange strain tensor. The shear strain, specifically, is calculated as twice the value of the off-diagonal component of the tensor S, that is (assuming symmetry $E_{12} = E_{21}$):

$$\gamma = 2E_{12} \quad (15)$$

This value, engineering shear strain, is crucial because it quantifies the material's deformation under shear loading, thereby reflecting its capacity to withstand seismic-induced stresses.

2.7. Equivalent Linear Approach

The linear model is the foundational constitutive model for site response, treating soil behavior as viscoelastic. It assumes a constant equivalent viscous damping ratio, unaffected by strain level or frequency. Using the small-strain shear modulus $G_{s\ max}^2$, derived from the soil's shear-wave velocity (V_s) and density (ρ), this model enables linear site-response analysis with inputs like shear-wave velocity, density, damping ratio, and base motion.

Unlike linear models with fixed soil properties, the equivalent linear method approximates nonlinear soil behavior by adjusting properties based on strain levels from cyclic loading. It divides the soil into sub-layers, improving seismic response predictions and enabling detailed analysis of interlayer interactions. This method offers a practical balance between computational efficiency and accuracy, especially when full nonlinear analysis is impractical.

In addition to the parameters used in linear models, the equivalent-linear approach requires strain-dependent modulus-reduction and damping curves. Shear modulus and damping are iteratively adjusted to match the effective shear strain and then held constant during each loading cycle. This tuning, based on peak strain, improves predictions of peak strains and displacements. In this study, we used Seed's [12] relationships for modulus-reduction and damping, modeling stress-strain behavior in layers above the bedrock. Calculations used a strain ratio of 0.65, with up to 20 iterations, and sublayers no thicker than 1 meter. After each iteration, shear modulus and damping were evaluated and compared with previous values for all sublayers to ensure convergence.

Fig. 4 presents a flowchart outlining the equivalent linear site response analysis using the SBFEM. It summarizes key steps from problem setup, material property input, and element selection to dynamic response calculation. This structured approach emphasizes accurate soil behavior modeling under seismic loading. The algorithm accommodates 2D, 3D, or axisymmetric problems, with inputs as force, displacement, or acceleration (this study considers a 2D in-plane acceleration case under sinusoidal and earthquake loading). Essential soil properties—Poisson's ratio, density, and shear wave velocity—are used to assign materials. Depending on the problem, elements such as L2 and L3 (2D) or Q4, Q8, Q9 (3D) are selected [39]. This analysis uses two-node elements with two degrees of freedom each. Once materials and elements are defined, soil layering is performed. Node coordinates are assigned counterclockwise around the scaling center, and boundary restraints and matrix dimensions are set. The total analysis time is defined by excitation duration and the time step, including that for unit impulse response. Subdividing soil

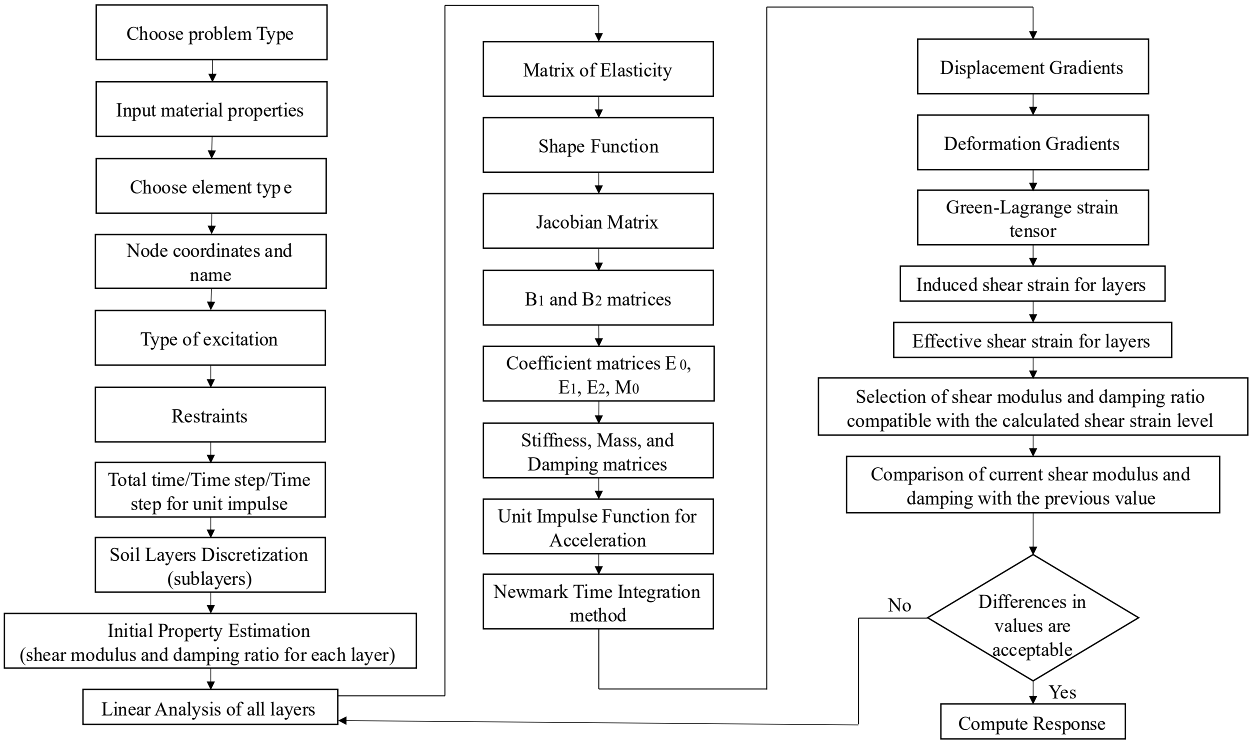

Figure 4. Flowchart of Equivalent Linear approach for layered soil

Table 1.
Characteristics of Earthquakes

Earthquake	Date	Location	Peak Ground Acceleration (PGA)	Peak Ground Velocity (PGV)	Vmax/Amax
Parkfield	September 28, 2004	Near Parkfield, California	0.35736 g	21.48479 cm/s	0.06129 sec
Nahanni	December 23, 1985	Nahanni Region, Northwest Territories, Canada	0.14275 g	6.06058 cm/s	0.04328 sec

Table 2.
Soil layers properties

Shear Wave Velocity m/s	Density kg/m³	Unit Weight kN/m³	Poisson's ratio
200	1836	18	0.4
300	1938	19	0.35
500	2040	20	0.3
700 (Bedrock)	-	22	-

layers into thinner sublayers enhances accuracy. The analysis begins with initial shear modulus and damping values at low strain. These are updated iteratively based on effective strain using empirical relationships. If differences between iterations fall within an acceptable range, the results are finalized; otherwise, the process continues until convergence or the iteration limit is reached.

This methodology is particularly effective in stratigraphically complex conditions, where varying mechanical properties across layers significantly affect seismic response. Iterative updates to modulus and damping are essential for accurately predicting ground motion. By analyzing each layer in relation to adjacent ones, the method offers a clear understanding of seismic wave amplification and energy dissipation throughout the soil profile.

3. Verification

3.1. Selection of Input Motions and Description of Soil Profiles

3.1.1. Overview of Seismic Input and Soil Configurations

To rigorously compare the outputs from the proposed approach with those from DEEPSOIL and QUAKE/W, a variety of input motions were used. These included sinusoidal excitations and actual earthquake such as the Parkfield and Nahanni earthquakes, categorized as in-plane motions.

Table 1 provides detailed specifications of the seismic events used in the verification studies, namely the Parkfield and Nahanni earthquakes. Additionally, the properties of the soil layers in the analyzed profiles are summarized in the Table 2.

3.1.2. Sinusoidal Excitations and Soil Profiles

This section details the setup for simulations using sinusoidal excitations on various soil profiles. Each profile is designed to understand the response of different soil types under controlled vibratory conditions.

- Soil Profiles: Three single-layer soil profiles are considered, see Table 3 and Fig. 5.
- Excitation Characteristics: The excitations are applied for a duration of 10 seconds and feature a periodicity of 0.4 seconds. The amplitude of the sinusoidal waves varies, with tests conducted at 0.375g, 0.75g, 1.5g, and 3g (respectively excitations SI, SII, SIII and SIV), see Fig. 6.

Table 3.
Soil profiles for sinusoidal excitations

Profile	No. of Layers	Layer Thickness (m)	Shear Wave Velocity (m/s)
S500	1	30	500
S300	1	30	300
S200	1	30	200

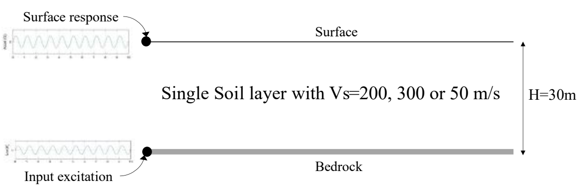

Figure 5. Soil profile with single layer

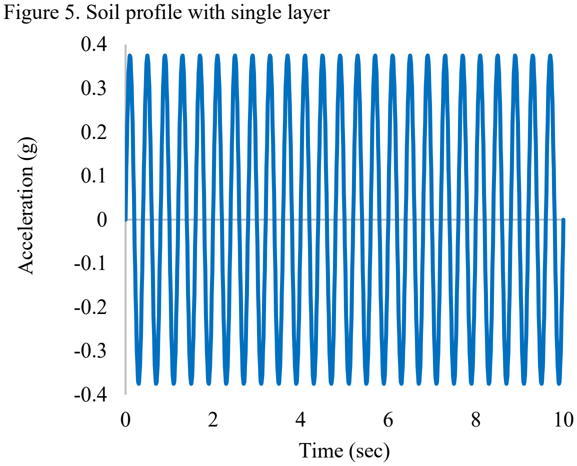

Figure 6. Input motion with amplitude of 0.375g

3.1.3. Parkfield Earthquakes and Soil Profiles

- Soil Profiles: The details of the six soil profiles under the Parkfield earthquake are shown in Table 4 and Fig. 7.
- Duration and Intensity: The duration of the earthquake simulation is 10 seconds, with intensity levels adjusted to half, original, and double the original recorded scales (respectively excitations EI, EII, EIII), see Fig. 8.

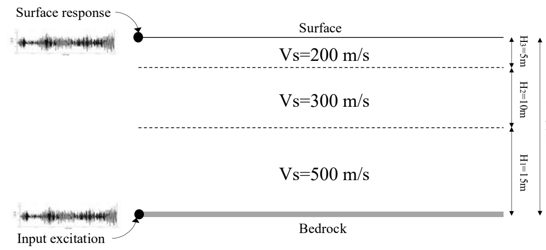

a) P532

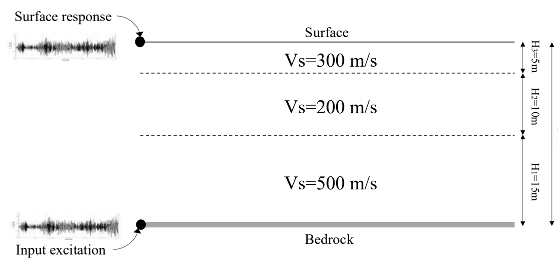

b) P523

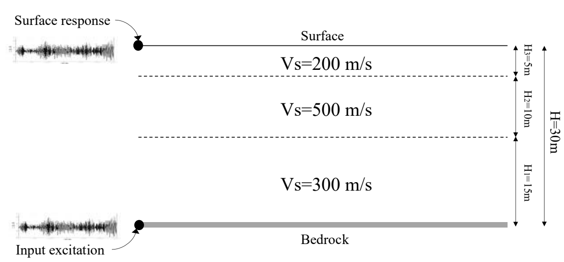

c) P352

Figure 7. Three-layer soil profiles

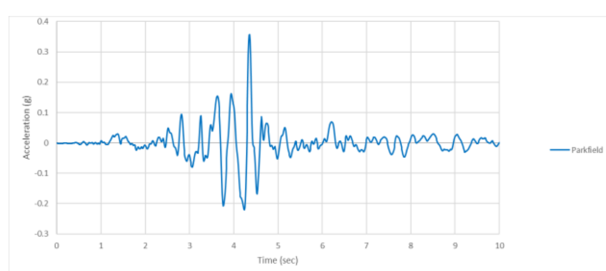

Figure 8. Original Parkfield earthquake

3.1.4. Nahanni Earthquakes and Soil Profiles

- Soil Profiles: Further validation is performed using data from the Nahanni earthquake, applying similar profiles as those in the Parkfield scenarios but adjusting for the unique characteristics of the Nahanni event and the prefix N instead of P is used in naming the profiles (such as N500, N300, etc.).
- Duration and Intensity: The duration for these tests extends to 19 seconds to accommodate the longer-lasting Nahanni earthquake dynamics, with intensity variations also set at half, original, and double the original scale (respectively excitations QI, QII, QIII), see Fig. 9.

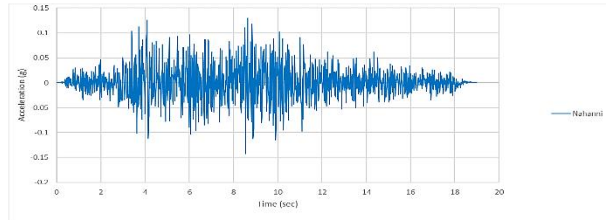

Figure 9. Original Nahanni earthquake

This section aims to not only verify the accuracy of the proposed approach but also to highlight the comparative efficiency and applicability of the proposed approach, DEEPSOIL, and QUAKE/W in handling diverse seismic scenarios.

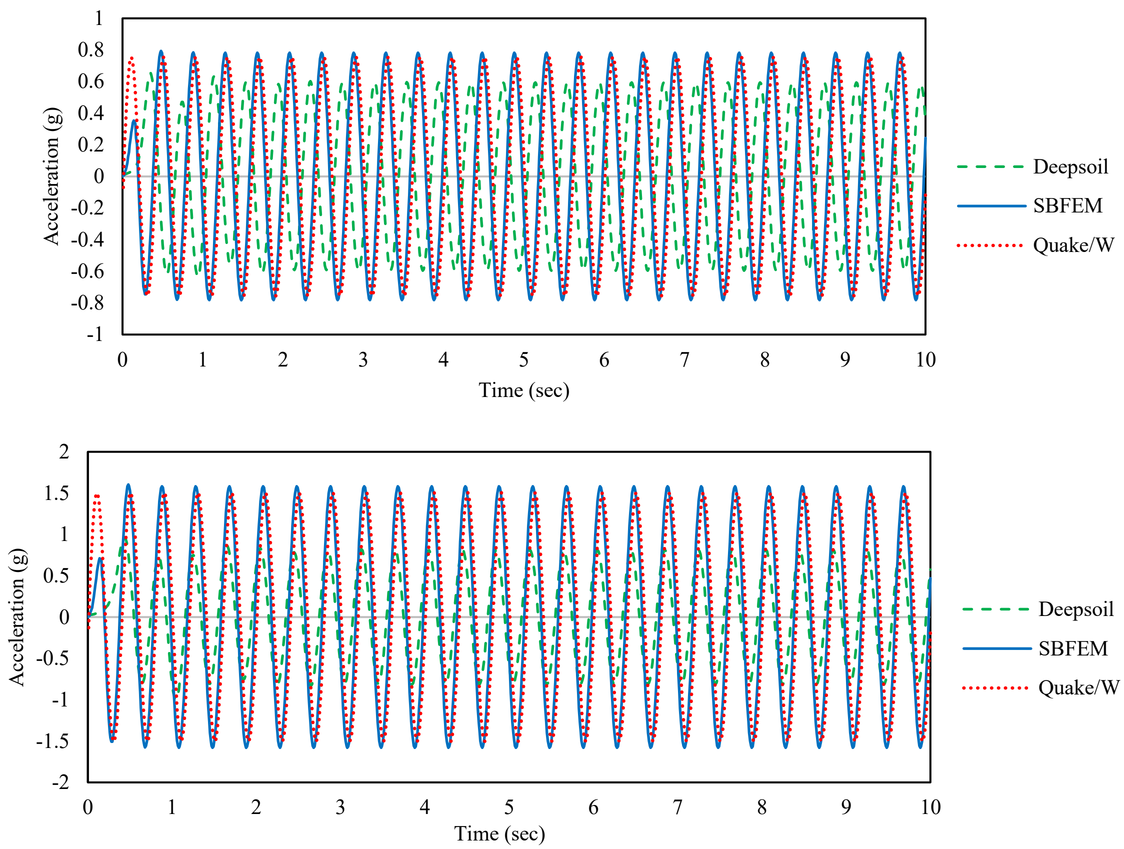

(a)

(b)

Figure 10. Response acceleration time history of profile S300 for sinusoidal excitations of a) A=0.75g and b) A=1.5g

4. Comparative Analysis of Site Response Under Various Seismic Conditions

4.1. Analysis Results from Sinusoidal Excitations

The results from the sinusoidal excitation tests offer a comprehensive analysis of how single-layer soil profiles respond to varying seismic load amplitudes, utilizing the SBFEM as implemented in MATLAB. The acceleration time histories recorded at the surface are juxtaposed with results from established geotechnical analysis software, namely DEEPSOIL and QUAKE/W, to validate the proposed approach's efficacy.

Fig. 10, as the sample, illustrates the surface acceleration time history for a single-layer soil profile with a shear wave velocity of 300 m s^{-1} (S300) under excitations

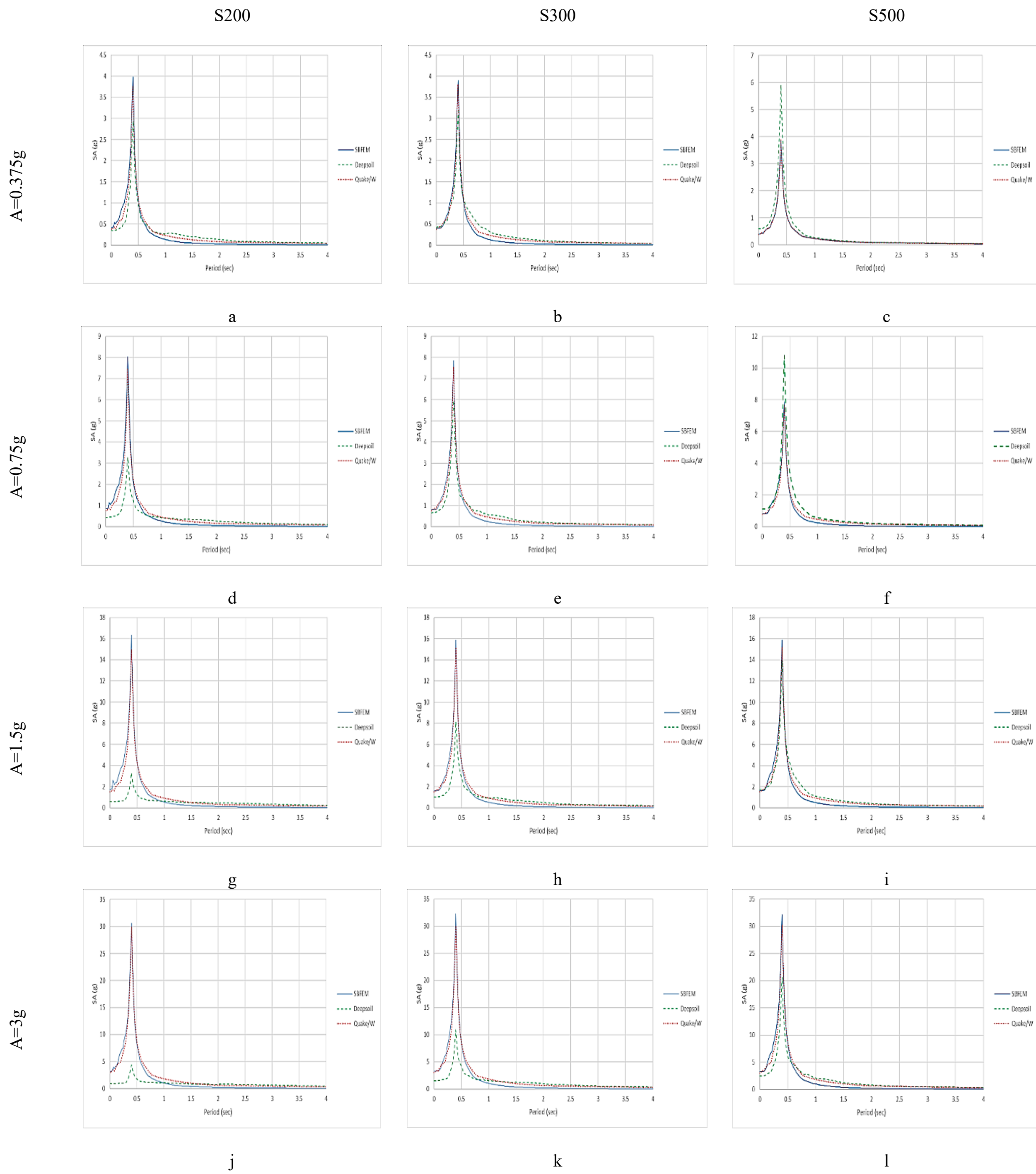

Figure 11. Acceleration response spectrum of sinusoidal excitations of single layer soils

SII and SIII. The response acceleration time histories for single-layer soil profiles (S200, S300, S500) under sinusoidal excitation show that the SBFEM closely matches QUAKE/W results, particularly at higher shear wave velocities. For instance, in the S200 profile under excitation SI, peak accelerations from SBFEM and QUAKE/W differed by only 8%, while DEEPSOIL deviated by 25% with a 0.1-second phase shift. In stiffer soils like S500, DEEPSOIL discrepancies increased to 33% in peak acceleration and 0.15 seconds in timing. Under excitation SIII, SBFEM demonstrated reliable performance in the S500 profile, with peak acceleration differences of respectively 12% and 4% compared to DEEPSOIL and QUAKE/W.

Fig. 11 presents the surface acceleration response spectrum under sinusoidal excitations. For example, Fig.

Table 5.
The peak percentage difference in the acceleration response spectrum of SBFEM compared to DEEPSOIL and QUAKE/W for sinusoidal excitation

		Profile					
		S200		S300		S500	
		DEEPSOIL	QUAKE/W	DEEPSOIL	QUAKE/W	DEEPSOIL	QUAKE/W
Excitation	SI	-35.1	-6.1	-22.7	-2.5	34.6	0.0
	SII	-145.3	-7.2	-31.5	-3.7	27.1	-3.0
	SIII	-396.9	-9.1	-94.5	-5.2	-13.6	-4.5
	SIV	-595.8	-2.3	-195.3	-7.2	-56.1	-6.3

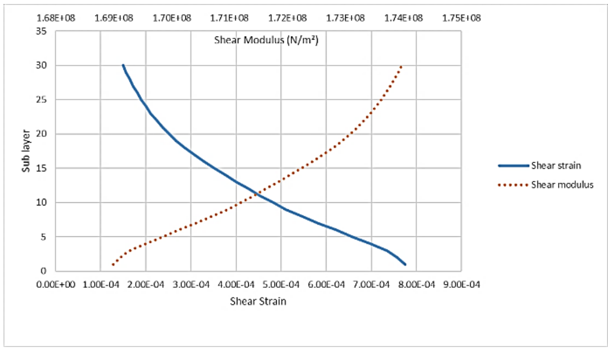

Figure 12. Shear strain and shear modulus of sublayers of profile S300 for sinusoidal excitation amplitudes A=0.75g

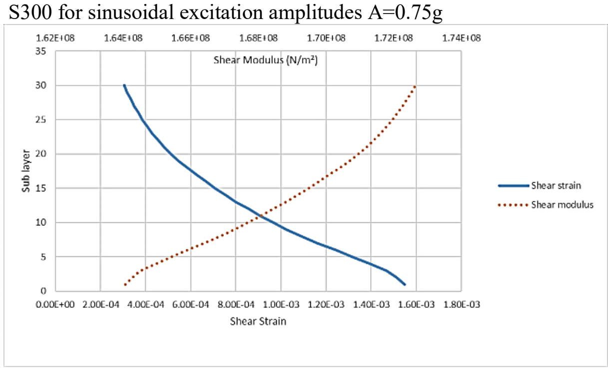

Figure 13. Shear strain and shear modulus of sublayers of profile S300 for sinusoidal excitation amplitudes A=1.5g

11a shows a peak at the soil's natural frequency, indicating resonance, with SBFEM and QUAKE/W closely matching, while DEEPSOIL shows slight deviations. Table 5 shows the percentage differences in peak spectral values between SBFEM and both DEEPSOIL and QUAKE/W, with signs indicating whether the reference method over- or underestimates the SBFEM result. The response spectra from Fig. 11a to Fig. 11l show consistent agreement between SBFEM and QUAKE/W, especially at primary resonance frequencies and peak accelerations, confirming both methods' ability to capture key dynamic behavior. At higher frequencies, DEEPSOIL aligns more closely with QUAKE/W than with SBFEM.

Fig. 12 and Fig. 13, serving as examples, illustrate the mechanical behavior of the S300 soil profile under A=0.75g and A=1.5g sinusoidal excitations, showing shear strain and shear modulus variations across the vertical profile. These figures provide key insights into deformation mechanisms and soil stiffness changes during seismic loading. All soil profiles show that shear strain is highest in the deepest layers near the excitation source and decreases toward the surface as wave energy dissipates. The S500 profile under excitation SI exhibits lower shear strains at all depths than S200 and S300, due to its higher stiffness affecting strain distribution. Across all soil profiles, shear modulus increases from the deepest layers to the surface, reflecting typical seismic soil behavior where higher strains cause soil softening. This trend highlights how seismic energy absorption reduces stiffness in deeper layers under higher strain conditions.

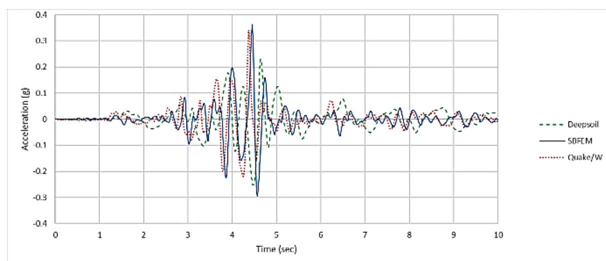

Figure 14. Response acceleration time history of profile P200 for excitation EII of Parkfield earthquake

4.2. Response Analysis of Parkfield Earthquake Simulations

The Parkfield earthquake analysis on single-layer soil profiles (P200, P300, P500) offers insights into dynamic responses under different seismic intensities. Three intensity levels (EI, EII, EIII) were used to assess soil behavior under varying stress conditions.

Fig. 14, as the sample, shows the surface acceleration time history for the P200 profile under excitation EII using SBFEM, compared against DEEPSOIL and QUAKE/W results. Under excitation EI, SBFEM slightly overestimates P200 by 6%, consistent with QUAKE/W and DEEPSOIL. For P300 and P500 under the same excitation, DEEPSOIL records peak accelerations 26% and 31% higher than SBFEM. In excitation EII, SBFEM yields higher accelerations for P200, exceeding DEEPSOIL and

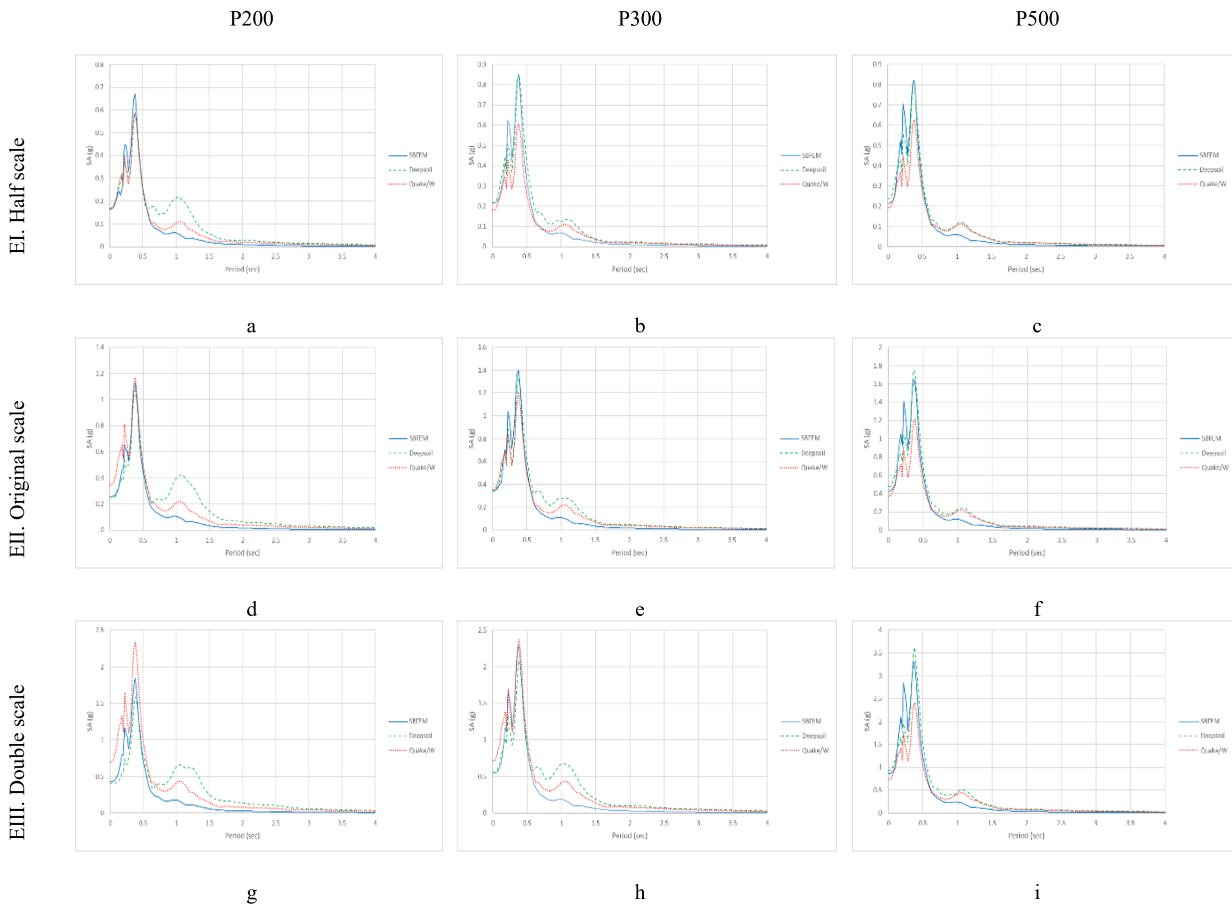

Figure 15. Acceleration response spectrum of Parkfield earthquakes for single layer soils

Table 6.
The peak percentage difference in the acceleration response spectrum of SBFEM compared to DEEPSOIL and QUAKE/W for Parkfield excitations of single layer profile

		Profile					
		P200		P300		P500	
		DEEPSOIL	QUAKE/W	DEEPSOIL	QUAKE/W	DEEPSOIL	QUAKE/W
Excitation	EI	-13.2	-14.4	0.6	-39.8	0.6	-30.1
	EII	-5.3	3.6	-5.8	-16.9	6.5	-34.0
	EIII	-15.7	21.3	-9.8	3.3	9.2	-36.8

QUAKE/W by 4% and 42%, respectively, with smaller differences in stiffer profiles (P300 and P500). Under excitation EIII, larger discrepancies occur for P200, where QUAKE/W exceeds SBFEM by over 48%, while differences in P300 and P500 are less pronounced.

Fig. 15 presents the surface acceleration response spectra for each soil profile and earthquake intensity, illustrating the soil layers' frequency response. Table 6 lists the percentage differences in peak spectral values compared to DEEPSOIL and QUAKE/W. In Fig. 15a, SBFEM predicts higher spectral accelerations at the predominant period, while QUAKE/W and DEEPSOIL align closely. In Fig. 15b and Fig. 15c, SBFEM matches DEEPSOIL at low periods, and DEEPSOIL matches QUAKE/W at mid to high periods. All methods show consistent phase responses, but amplitude differences reflect variations in energy distribution modeling. Fig. 15g, Fig. 15h, and Fig. 15i extend these spectral trends.

Fig. 16, a representative case, illustrates the final shear strain and shear modulus distribution for the P200 profile under excitation EII, highlighting variations in strain magnitude and soil stiffness across the sublayers. All profiles show lower shear strain at depth, reflecting the intrinsic characteristics of soil layers. Shear modulus consistently increases toward the surface, independent of seismic scaling, indicating mechanical stiffening with

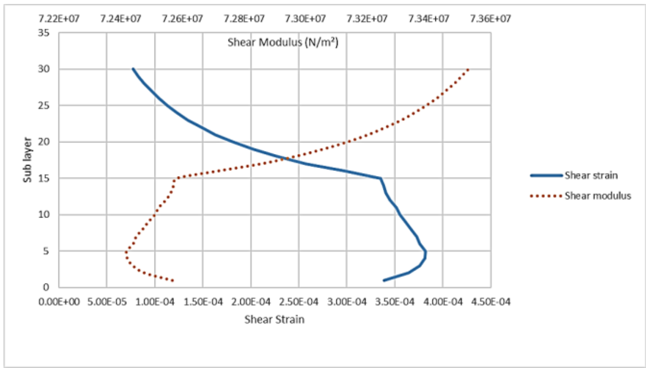

Figure 16. Shear strain and shear modulus of sublayers of profile P200 for excitation EII of Parkfield earthquake

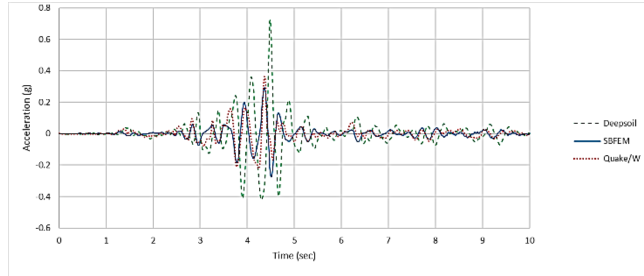

Figure 17. Response acceleration time history of profile P532 for excitation EII of Parkfield earthquake

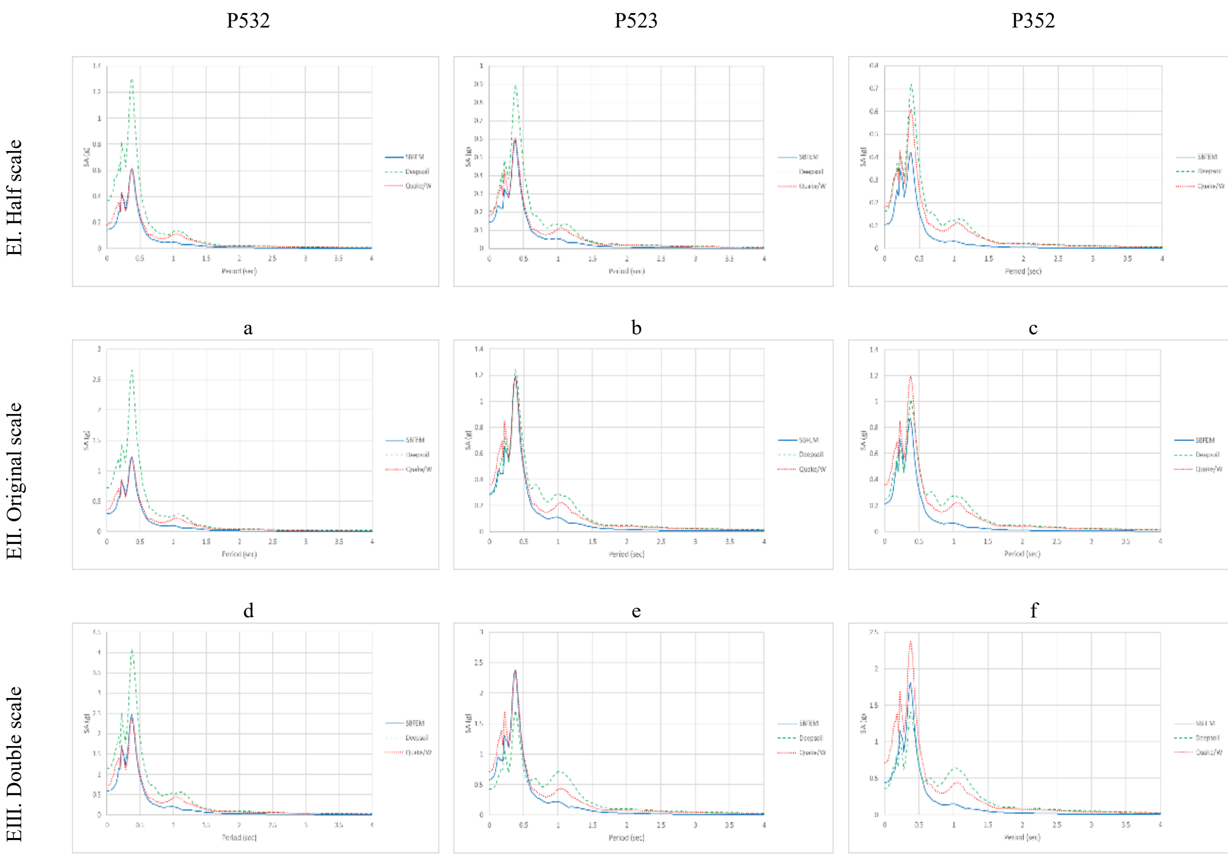

Figure 18. Acceleration response spectrum of Parkfield earthquakes for three layers soils

Table 7.

The peak percentage difference in the acceleration response spectrum of SBFEM compared to DEEPSOIL and QUAKE/W for Parkfield excitations of three-layer profiles

		Profile					
		P532		P523		P352	
		DEEPSOIL	QUAKE/W	DEEPSOIL	QUAKE/W	DEEPSOIL	QUAKE/W
Excitation	EI	53.0	-0.5	33.9	2.1	41.6	31.1
	EII	53.6	-2.5	4.5	0.6	14.4	27.5
	EIII	39.8	-3.9	-39.4	-0.7	-28.3	23.8

decreased depth. However, subtle deviations in deeper sublayers, particularly in P200 under excitations EI, EII, and EIII, suggest localized variations in soil behavior.

Similar to the single-layer cases, Fig. 19, as a sample, illustrates the final shear strain and shear modulus for the P532 profile under excitation EII. Across the three-layer profiles and intensity levels, shear strain consistently decreases with depth. In the P523 profile, a sharp strain drop occurs at the interface between 500 m s^{-1} and 200 m s^{-1} layers at 15 m depth, highlighting the strong influence of stiffness contrasts on strain distribution under dynamic loading.

4.3. Response Analysis of Nahanni Earthquake Simulations

Using the same approach as for the Parkfield earthquake, the Nahanni earthquake was analyzed for single-layer profiles N200, N300, and N500 across three intensity levels.

Fig. 20, as the sample, shows the surface acceleration time history for N300 under excitation QII using SBFEM, compared with DEEPSOIL and QUAKE/W. DEEPSOIL consistently predicts higher accelerations for N200 and N300, particularly under excitations QI and QII. The peak acceleration response for the N200 profile under excitation Q1 are 39% and 55% lower for SBFEM and QUAKE/W respectively compared to DEEPSOIL, and for excitation Q2, these values are 25% and 38% lower, respectively.

Fig. 21 shows the acceleration response spectra for the Nahanni earthquake, highlighting the soil's frequency response. At lower periods, SBFEM and QUAKE/W results align closely, indicating similar accuracy. At longer periods, DEEPSOIL and QUAKE/W converge, suggesting shared modeling behavior. Table 8 lists the percentage differences in peak spectral values compared to DEEPSOIL and QUAKE/W for single-layer profiles.

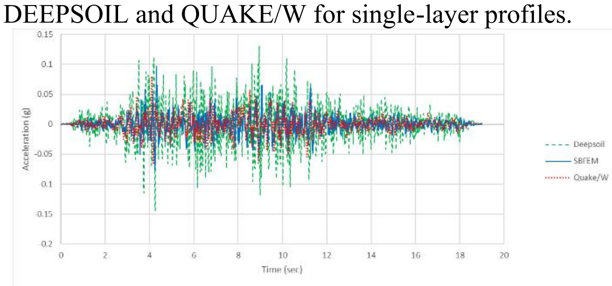

Figure 20. Response acceleration time history of profile N300 for excitation QII of Nahanni earthquake

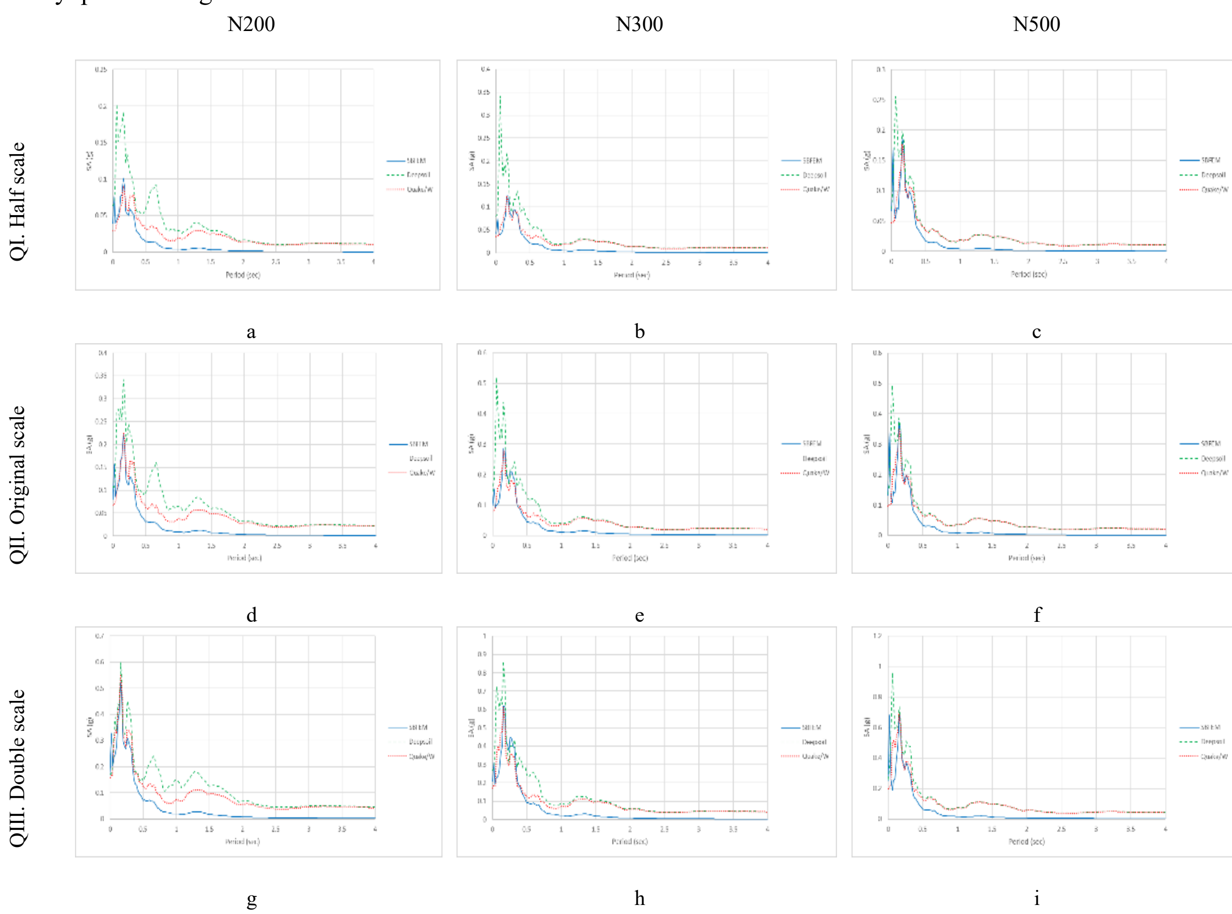

Figure 21. Acceleration response spectrum of Nahanni earthquakes for single layer soils

Table 8.
The peak percentage difference in the acceleration response spectrum of SBFEM compared to DEEPSOIL and QUAKE/W for Nahanni excitations of single layer profile

		Profile					
		N200		N300		N500	
		DEEPSOIL	QUAKE/W	DEEPSOIL	QUAKE/W	DEEPSOIL	QUAKE/W
Excitation	QI	47.5	-12.0	42.7	-0.9	6.7	-4.7
	QII	35.2	2.2	34.5	-2.0	3.2	-6.1
	QIII	12.4	4.7	28.2	-1.4	6.5	0.9

Fig. 22, an illustrative example, shows the final shear strain and shear modulus for N300 under excitation QII, highlighting earthquake-induced changes in mechanical properties. Shear strain increases with depth, while shear modulus generally rises toward the surface.

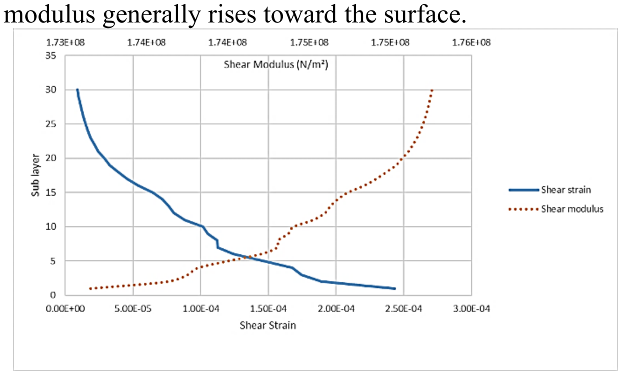

Figure 22. Shear strain and shear modulus of sublayers of profile N300 for excitation QII of Nahanni earthquake

The three-layer profiles N532, N523, and N352 were also analyzed under the same Nahanni earthquake intensity levels.

Fig. 23, as an example, shows the acceleration time history for N523 under excitation QII, and Fig. 24 presents surface response spectra for all three profiles. In the response acceleration time history for N532 and N352, DEEPSOIL and SBFEM results align closely, while QUAKE/W amplitudes are about 50% lower, suggesting similar sensitivity between DEEPSOIL and SBFEM. In contrast, for N523, SBFEM and QUAKE/W exhibit stronger agreement, with differences in response remaining below 10% for most of the analysis time steps, indicating their compatibility in modeling the unique characteristics of this profile.

In Fig. 24, DEEPSOIL consistently shows the highest spectral values—especially at natural periods—while SBFEM records the lowest, except in Fig. 24d. At higher periods, DEEPSOIL and QUAKE/W results overlap significantly, indicating similar performance in capturing long-period responses. Fig. 24d shows notable divergence, suggesting variability under certain seismic or soil conditions. Table 9 summarizes the percentage differences in peak spectral values between SBFEM, DEEPSOIL, and QUAKE/W for the three-layer profiles under the Nahanni earthquake.

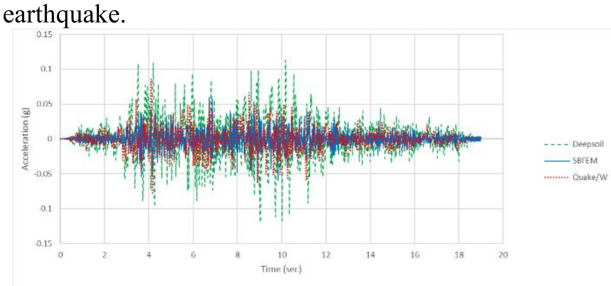

Figure 23. Response acceleration time history of profile N523 for excitation QII of Nahanni earthquake

As a sample, Fig. 25 presents the final shear strain and shear modulus for profile N523 under excitation QII. The results, which depict shear strain and shear modulus from the Nahanni earthquake show trends consistent with those observed in the Parkfield analyses.

5. Conclusions

This study has made a remarkably strong impact on the understanding of site response analysis in the geotechnical earthquake engineering discipline, combining versatile theoretical and computational techniques. Employing the SBFEM, we conducted a two-dimensional equivalent linear site response analysis that incorporated Rayleigh damping. Our results confirm that SBFEM provides a robust framework for accurately modeling the dynamic responses of soil layers to seismic activities. The method's ability to handle complex boundary conditions and its computational efficiency make it particularly suitable for analyzing earthquake-induced site responses.

We have successfully compared the SBFEM with traditional numerical methods, with the outcomes being similar and highly reliable, thus, clearly testifying to its precise performance in seismic analysis. The Rayleigh damping that is added to the SBFEM gives it an additional ability to simulate the real-world dissipation of energy by soils and thus, gives more information about the dampening characteristics during seismic events.

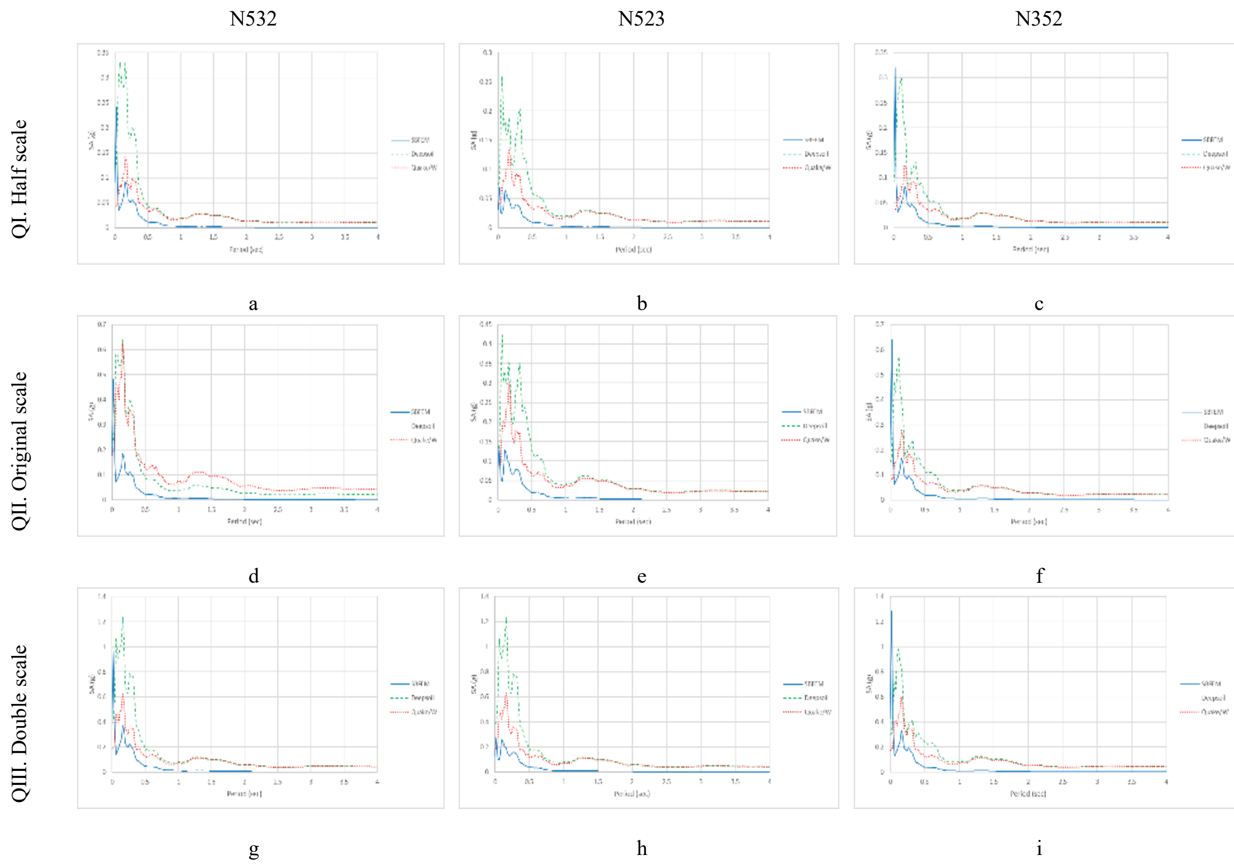

Figure 24. Acceleration response spectrum of Nahanni earthquakes for three layers soils

Table 9.

The peak percentage difference in the acceleration response spectrum of SBFEM compared to DEEPSOIL and QUAKE/W for Nahanni excitations of three-layer profiles

		Profile					
		N532		N523		N352	
		DEEPSOIL	QUAKE/W	DEEPSOIL	QUAKE/W	DEEPSOIL	QUAKE/W
Excitation	QI	71.7	33.6	66.0	52.5	72.1	33.1
	QII	70.9	70.3	64.0	57.2	70.9	40.2
	QIII	69.8	40.6	79.1	59.6	66.1	44.5

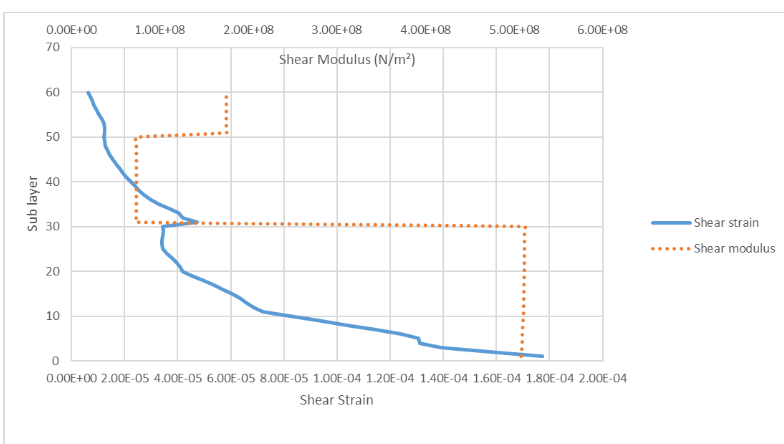

Figure 25. Shear strain and shear modulus of sublayers of profile N523 for excitation QII of Nahanni earthquake

Moreover, our research emphasizes the crucial influence of soil layer properties on seismic wave amplification and attenuation. Accurate characterization of these properties is essential for enhancing earthquake-resistant design and improving seismic risk assessments. The adaptation of SBFEM for various intensity excitations and for unbounded domains represents a significant methodological advancement, providing a powerful tool for more effectively predicting seismic responses. Besides, results highlight the importance of method choice in seismic analysis across varying soil types.

The implications of this research are significant for the field of geotechnical earthquake engineering, especially in regions susceptible to earthquakes. By delivering a more precise assessment of soil behavior under seismic loads, our approach can significantly contribute to the development of safer and more effective earthquake-resistant designs.

Future efforts will focus on the extension of SBFEM to non-linear site response analyses and the exploration of three-dimensional modeling capabilities. These advancements are expected to deepen our understanding of the complex interactions between soil layers and seismic waves, leading to enhanced predictive models and engineering solutions.

References

[1] Jia, J. and Jia, J. "Site-response Analysis in Geotechnical Earthquake Engineering." Soil Dynamics and Foundation Modeling: Offshore and Earthquake Engineering (2018): 109–165. https://doi.org/10.1007/978-981-10-5773-9_4

[2] Boore, D. M. "Can Site Response Be Predicted?." Journal of Earthquake Engineering 8.spec01 (2004): 1–41. https://doi.org/10.1080/13632460409350519

[3] Wang, Z. and Carpenter, N. S. "Linear Site Responses from US Borehole Arrays: Primary Site-Response Parameters and Proxies." Soil Dynamics and Earthquake Engineering 164 (2023): 107578. https://doi.org/10.1016/j.soildyn.2022.107578

[4] Hashash, Y. M. A. et al. DEEPSOIL 7.0 User Manual. Urbana, IL: Board of Trustees of the University of Illinois at Urbana-Champaign, 2020.

[5] Kaklamanos, J., Baise, L. G., Thompson, E. M., and Dorfmann, L. "Comparison of 1D Linear, Equivalent-Linear, and Nonlinear Site Response Models at Six KiK-net Validation Sites." Soil Dynamics and Earthquake Engineering 69 (2015): 435–460. https://doi.org/10.1016/j.soildyn.2014.11.008

[6] Kim, B. et al. "Relative Differences Between Nonlinear and Equivalent-Linear 1D Site Response Analyses." Earthquake Spectra 32.3 (2016): 1845–1865. https://doi.org/10.1193/063015EQS107M

[7] Kramer, S. L. Geotechnical Earthquake Engineering. Upper Saddle River, NJ: Prentice Hall, 1996.

[8] Song, C. The Scaled Boundary Finite Element Method: Introduction to Theory and Implementation. Hoboken, NJ: John Wiley & Sons, 2018. https://doi.org/10.1002/9781119078388

[9] Semblat, J.-F. "Modeling Seismic Wave Propagation and Amplification in 1D/2D/3D Linear and Nonlinear Unbounded Media." International Journal of Geomechanics 11.6 (2011): 440–448. https://doi.org/10.1061/(ASCE)GM.1943-5622.0000050

[10] Bazyar, M. H. and Song, C. "Analysis of Transient Wave Scattering and Its Applications to Site Response Analysis Using the Scaled Boundary Finite-Element Method." Soil Dynamics and Earthquake Engineering 98 (2017): 191–205. https://doi.org/10.1016/j.soildyn.2017.04.013

[11] Tönük, G. and Ansal, A. "Factors Affecting Site-Specific Response Analysis." Journal of Earthquake Engineering 26.16 (2022): 8629–8646. https://doi.org/10.1080/13632469.2022.2085851

[12] Seed, H. B. Soil Moduli and Damping Factors for Dynamic Response Analyses, Report No. EERC-70. Berkeley, CA: Earthquake Engineering Research Center, University of California, 1970.

[13] Hashash, Y. M. A. and Park, D. "Non-Linear One-Dimensional Seismic Ground Motion Propagation in the Mississippi Embayment." Engineering Geology62.1–3 (2001): 185–206. https://doi.org/10.1016/S0013-7952(01)00047-0

[14] Park, D. and Hashash, Y. M. A. "Soil Damping Formulation in Nonlinear Time Domain Site Response Analysis." Journal of Earthquake Engineering 8.2 (2004): 249–274. https://doi.org/10.1080/13632460409350493

[15] Wolf, J. P. and Song, C. Finite-Element Modelling of Unbounded Media. Chichester: Wiley, 1996.

[16] Song, C. and Wolf, J. P. "The Scaled Boundary Finite-Element Method---Alias Consistent Infinitesimal Finite-Element Cell Method---for Elastodynamics." Computer Methods in Applied Mechanics and Engineering 147.3–4 (1997): 329–355. https://doi.org/10.1016/S0045-7825(97)00038-1

[17] Wolf, J. P. The Scaled Boundary Finite Element Method. Chichester: John Wiley & Sons, 2003.

[18] Khaji, N. and Khodakarami, M. I. "A New Semi-Analytical Method with Diagonal Coefficient Matrices for Potential Problems." Engineering Analysis with Boundary Elements 35.6 (2011): 845–854. https://doi.org/10.1016/j.enganabound.2010.12.006

[19] Zhang, X., Wegner, J. L., and Haddow, J. B. "Three-Dimensional Dynamic Soil-Structure Interaction Analysis in the Time Domain." Earthquake Engineering and Structural Dynamics 28.12 (1999): 1501–1524. https://doi.org/10.1002/(SICI)1096-9845(199912)28:12<1501::AID-EQE891>3.0.CO;2-Y

[20] Birk, C., Prempramote, S., and Song, C. "An Improved Continued-Fraction-Based High-Order Transmitting Boundary for Time-Domain Analyses in Unbounded Domains." International Journal for Numerical Methods in Engineering 89.3 (2012): 269–298. https://doi.org/10.1002/nme.3240

[21] Birk, C., Chen, D., Song, C., and Du, C. "The Scaled Boundary Finite Element Method for Transient Wave Propagation Problems." Seismic Design of Industrial Facilities: Proceedings of the International Conference on Seismic Design of Industrial Facilities (SeDIF-Conference) (2014): 547–556. https://doi.org/10.1007/978-3-658-02810-7_43

[22] Bazyar, M. H. and Song, C. "Transient Analysis of Wave Propagation in Non-Homogeneous Elastic Unbounded Domains by Using the Scaled Boundary Finite-Element Method." Earthquake Engineering & Structural Dynamics 35.14 (2006): 1787–1806. https://doi.org/10.1002/eqe.605

[23] Chen, X., Birk, C., and Song, C. "Transient Analysis of Wave Propagation in Layered Soil by Using the Scaled Boundary Finite Element Method." Computers and Geotechnics 63 (2015): 1–12. https://doi.org/10.1016/j.compgeo.2014.11.007

[24] Yaseri, A., Bazyar, M. H., and Hataf, N. "3D Coupled Scaled Boundary Finite-Element/Finite-Element Analysis of Ground

Vibrations Induced by Underground Train Movement." Computers and Geotechnics 60 (2014): 1–8. https://doi.org/10.1016/j.compgeo.2014.01.008

[25] Idriss, I. M. and Seed, H. B. Response of Horizontal Soil Layers During Earthquakes. Berkeley, CA: Earthquake Engineering Research Center, University of California, 1967.

[26] Schnabel, P. B. SHAKE: A Computer Program for Earthquake Response Analysis of Horizontally Layered Sites, Report No. EERC-72/12. Berkeley, CA: Earthquake Engineering Research Center, University of California, 1972.

[27] Idriss, I. M. and Sun, J. I. SHAKE91: A Computer Program for Conducting Equivalent Linear Seismic Response Analyses of Horizontally Layered Soil Deposits. Davis, CA: Center for Geotechnical Modeling, Department of Civil and Environmental Engineering, University of California, 1992.

[28] Ordonez, G. A. SHAKE2000: A Computer Program for the 1D Analysis of Geotechnical Earthquake Engineering Problems. Seattle, WA: GeoMotions, LLC, 2000.

[29] Vucetic, M. and Dobry, R. "Effect of Soil Plasticity on Cyclic Response." Journal of Geotechnical Engineering 117.1 (1991): 89–107. https://doi.org/10.1061/(ASCE)0733-9410(1991)117:1(89)

[30] Electric Power Research Institute (EPRI). Guidelines for Determining Design Basis Ground Motions, Final Report No. TR-102293. Palo Alto, CA: EPRI, 1993.

[31] Ishibashi, I. and Zhang, X. "Unified Dynamic Shear Moduli and Damping Ratios of Sand and Clay." Soils and Foundations 33.1 (1993): 182–191.

[32] Darendeli, M. B. Development of a New Family of Normalized Modulus Reduction and Material Damping Curves, PhD dissertation, University of Texas at Austin, 2001.

[33] Zhang, J., Andrus, R. D., and Juang, C. H. "Normalized Shear Modulus and Material Damping Ratio Relationships." Journal of Geotechnical and Geoenvironmental Engineering 131.4 (2005): 453–464. https://doi.org/10.1061/(ASCE)1090-0241(2005)131:4(453)

[34] Soliman, M. A. K. A. Dynamic Analysis of Unbounded Domain Problems by Applying the Scaled Boundary Finite-Element Method, MSc thesis, Faculty of Engineering Shoubra, Benha University, 2015.

[35] Khani, B. M. and Mohammad, H. Dynamic Soil-Structure Interaction Analysis Using the Scaled Boundary Finite-Element Method, PhD dissertation, UNSW Sydney, 2007.

[36] Radmanović, B. and Katz, C. "A High Performance Scaled Boundary Finite Element Method." IOP Conference Series: Materials Science and Engineering 10.1 (2010): 012214. https://doi.org/10.1088/1757-899X/10/1/012214

[37] Ju, S. H. and Ni, S. H. "Determining Rayleigh Damping Parameters of Soils for Finite Element Analysis." International Journal for Numerical and Analytical Methods in Geomechanics 31.10 (2007): 1239–1255. https://doi.org/10.1002/nag.586

[38] Bonet, J. and Wood, R. D. Nonlinear Continuum Mechanics for Finite Element Analysis. Cambridge: Cambridge University Press, 1997. https://doi.org/10.1017/CBO9780511755446

[39] Astley, R. J. Finite Elements in Solids and Structures: An Introduction. London: Chapman & Hall, 1992.

J-Researchers

Journal of Civil Engineering Researchers

Journal homepage: www.journals-researchers.com

The Evaluation of Bond Strength of Heavyweight Concrete Containing Iron Pellets

Seyed Abbas Hosseini,[a,*] Mansour Bagheri[b]

[a] Faculty of Engineering, Yasouj University, Yasouj, Iran, Iran

[b] Department of civil engineering, Birjand University of technology, Birjand, Iran

ABSTRACT

Heavyweight concrete incorporating iron aggregates is widely utilized as a radiation-shielding material in environments with harmful radiation due to its high density. Although this material is also employed as a structural component, certain mechanical properties, such as the bond strength between concrete and reinforcing steel bars, remain insufficiently studied. This paper investigates the bond strength of concrete containing varying percentages of iron pellets and its interaction with steel reinforcement. For this study, 25%, 75%, and 100% of the concrete aggregate was replaced with iron pellets, ensuring an appropriate grain size distribution. After curing under standard conditions, the specimens were subjected to direct pull-out tests. The results indicate that, except for the sample with 25% iron pellets, the inclusion of iron pellets slightly reduces compressive strength but enhances bond strength across all samples. Notably, adding 25% iron pellets combined with 5% micro silica in heavyweight concrete significantly improves compressive strength by 20% and bond strength by 43%.

ARTICLE INFO

Received: March 18, 2025
Accepted: April 28, 2025

Keywords:
Heavyweight Concrete
Bond Strength
Iron Pellts
Pull-Out Test
Micro Silica

DOI: 10.6624/JCER.7.3.69
DOR: 20.1001.1.2538516.2025.7.3.6.6

1. Introduction

Concrete, a durable, economical, and highly functional material with excellent mechanical properties, is one of the most widely used materials in the construction industry. A key reason for its increasing utilization is its adaptability; concrete can be modified in numerous ways to suit specific environmental conditions or desired performance requirements. One of the high-risk environments where the use of concrete is indispensable is in areas exposed to harmful nuclear radiation. In such settings, concrete is expected not only to fulfill its structural functions and meet durability requirements but also to provide effective shielding against harmful radiation. In these environments, heavyweight concrete, which has a higher density than conventional concrete, is typically employed. Concrete with a density exceeding 2600 kg/m³ is typically classified as heavyweight concrete. This type of concrete reduces the

* Corresponding author. Tel.: +987431005000; e-mail: a.hosseini@yu.ac.ir (AssociateProf. Seyed Abbas Hosseini).

transmission of radiation due to the inclusion of elements with high atomic numbers and elevated density. High-density aggregates, often containing iron, are commonly used in the production of heavyweight concrete.

The bond strength between concrete and rebar is a critical mechanical parameter that ensures the composite performance of reinforced concrete components. It enables the effective transfer of forces between the concrete and the rebar, which is essential for structural integrity. This bond strength is primarily achieved through adhesion, friction, and the mechanical interlocking of aggregates with the rebar ribs. Research indicates that the bond strength primarily occurs through the interlocking mechanism of aggregates and reinforcement [1, 2]. Several factors influence bond strength, with the most significant being the concrete's compressive strength, the geometry of the rebar ribs, the rebar diameter, and the presence of transverse reinforcement [3]. Research has demonstrated that ribbed bars exhibit bond strengths up to 30% higher than plain bars, irrespective of the concrete's compressive strength [3]. While increasing the compressive strength enhances bond strength, larger bar diameters typically reduce it [4, 5]. Xuan proposed a predictive relationship for bond strength based on compressive strength [6]. The thickness of the concrete cover over the bars also significantly influences bond strength. This effect is often evaluated using the c/D ratio, where c denotes the concrete cover thickness and D represents the bar diameter [7]. Ahmed et al. highlighted that increasing the c/D ratio enhances bond strength and reduces slip for bars of varying diameters [8]. Additionally, the presence of transverse reinforcement further improves bond strength [4].

Dragomirová and Palou demonstrated that the adhesion between iron-containing aggregates and cement paste is weaker in the transition zone compared to ordinary concrete, potentially compromising the structural integrity of the concrete [9]. Wang et al. investigated the influence of rebar length, diameter, and concrete cover on bond strength in heavyweight concrete, concluding that rebar length is a highly significant parameter affecting bond strength [10]. Additionally, Rosyidah et al. examined the impact of rebar rib geometry on the failure mechanisms associated with bond deterioration [11].

Several methods are available for quantitatively evaluating the bond strength between concrete and rebar, with the most widely used being the direct pull-out test and the beam end test, as outlined in the ASTM C944 standard. In the direct pull-out method, a rebar of specified length is embedded within a cubic or cylindrical concrete specimen. A tensile force is then applied to the rebar, and the maximum force required to pull out the rebar is measured based on the potential failure mechanisms. Although the results obtained from these methods are not directly applicable for design purposes, they serve as valuable comparative criteria. Numerous theoretical and empirical models have been developed to evaluate bond strength, with theoretical models typically yielding more conservative estimates [12]. Empirical models, however, can vary depending on the type of test conducted (reference). Hou et al. proposed a model based on key influential parameters, incorporating results from both direct tensile tests and beam tests [13]. Zhou et al. developed a predictive model for bond strength by analyzing data from a large number of tests conducted by other researchers. Through regression analysis, they found that both beam and pull-out test specimens were influenced by the same coefficients related to the development length-to-diameter ratio and restraint conditions, with the exception of concrete strength [1]. Despite the development of numerous models, no specific model has been proposed for concrete containing iron pellets. Furthermore, although extensive research has been conducted on bond strength, studies on heavyweight concrete, particularly concrete incorporating iron pellets, remain limited. Addressing this gap and responding to the growing interest in the mechanical properties of such concrete, this study investigates the bond strength of concrete with varying percentages of iron aggregate. The effects of different iron aggregate proportions on compressive strength and bond strength are examined, and the results are compared with existing empirical models.

2. Materials and methods

2.1. Materials

The materials used to fabricate the studied samples consisted of Type 2 Portland cement sourced from the Behbahan Cement Factory, potable water from Behbahan city, fine and coarse aggregates obtained from local Behbahan mines, iron aggregate from the Gol Gohar mines in Sirjan, Ahvaz iron shell, Azna micro silica, and a polycarboxylate-based superplasticizer. The properties of the Type 2 cement utilized in this study, including its initial and final setting times, as well as the compressive strength of samples at various curing ages for quality control purposes, are presented in Table 2. Micro silica in powder form, with the properties detailed in Table 3, was incorporated into the mixtures. To maintain consistent workability and reduce the water-to-cement ratio, a polycarboxylate-based superplasticizer, whose properties are outlined in Table 4, was employed. The aggregates, with a modified gradation curve as illustrated in Figure 1, exhibited saturated surface-dry densities of 2528 kg/m^3 for coarse aggregates and 2597 kg/m^3 for fine aggregates. The water absorption percentages were 1.6% for coarse aggregates and 1.56% for fine aggregates. Iron pellets, with a bulk density of 4540 kg/m³ and chemical composition detailed in Table 1, along with iron shells having a bulk density of 4230 kg/m³, were used as partial replacements for conventional aggregates in this study. The visual appearance and gradation of the iron aggregates are presented in Figure 2.

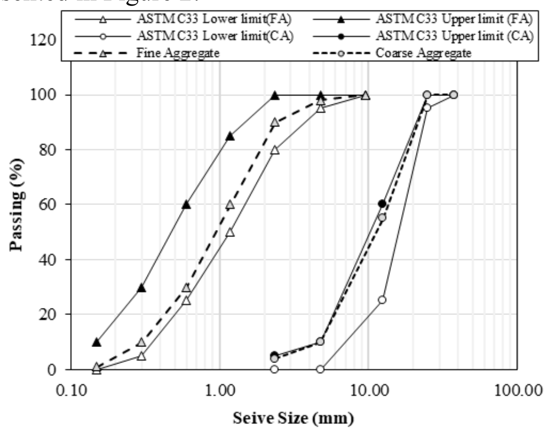

Fig. 1. Aggregate size distributions

Table 1
Chemical composition of iron pelts.

Composition	Fe (T)	SiO_2	Al_2O_3	CaO	MgO	FeO	P	S
Amount (%)	68	3.5	0.7	1.5	1.6	1.2	0.07	0.01

Table 2
Properties of Portland cement type II.

Initial set time (minutes)	Final set time (minutes)	Compressive strength (kg/cm^2)		
		3 days	7 days	28 days
185	220	245	405	546

Table 3
Properties of micro silca powder.

Silica (%)	Moisture (%)	Density (kg/m^3)	Blaine (m^2/gr)
93	0.25		22

Table 4
Properties of Polycarboxylate superplasticizers.

Name	pH	Solid content (kg/m^3)	Specific gravity
HF5000M	7.2	34	1.02

2.2. Sample preparation

To evaluate the influence of iron pellets on bond strength, 25%, 75%, and 100% of the coarse aggregate in the control mix design was replaced with iron pellets. The quantities of materials used in the examined mix designs are detailed in Table 5. Additionally, micro silica was incorporated into the mix design to enhance the permeability properties of the concrete. Two sets of samples were prepared for testing: one for compressive strength testing, consisting of 15 cm cube specimens, and the other for direct pull-out testing, which involved embedding a 14 mm diameter rebar at the center of a cube specimen during casting. As illustrated in Figure 3, a 5 cm length of PVC pipe was used to cover the upper portion of the rebar to prevent concrete-rebar bonding in that region, thereby eliminating stress and pressure effects at the top of the sample. Bond strength was thus developed only along the lower 10 cm of the rebar. The tests were conducted at 28 and 90 days, with three replicates tested for each mix design.

The direct pull-out test is the most widely used method for evaluating bond strength. This test employs a metal box, the dimensions of which are illustrated in Figure 6. As depicted in the figure, one side of the box is secured to the lower jaw of the tensile testing machine, while the upper jaw pulls the rebar after the concrete sample is positioned inside the box. As the tensile force on the rebar increases, different failure modes may occur: (1) if the tensile strength of the rebar is lower than the bond strength, the rebar ruptures at the top of the sample; (2) the rebar is pulled out of the sample without splitting the concrete; or (3) failure occurs due to concrete splitting.

Fig. 2. Iron mill scale and Iron pelts shapes and sizes.

Table 5

Mixes design and material compositions in one cubic meter of concrete samples.

Mixes	water (kg)	cement (kg)	Iron powder (%)	Iron pelts (%)	Iron powder (kg)	Iron pelts (kg)	Fine aggregates (kg)	Coarse aggregates (kg)	Micro-silica(kg)
C	180	370	-	-	-	-	960	860	-
CM	180	350	-	-	-	-	960	860	20
H25M	180	350	25	25	356	336	720	645	20
H75M	180	350	75	75	1068	1010	240	215	20
H100M	180	350	75	100	1068	1350	240	-	20

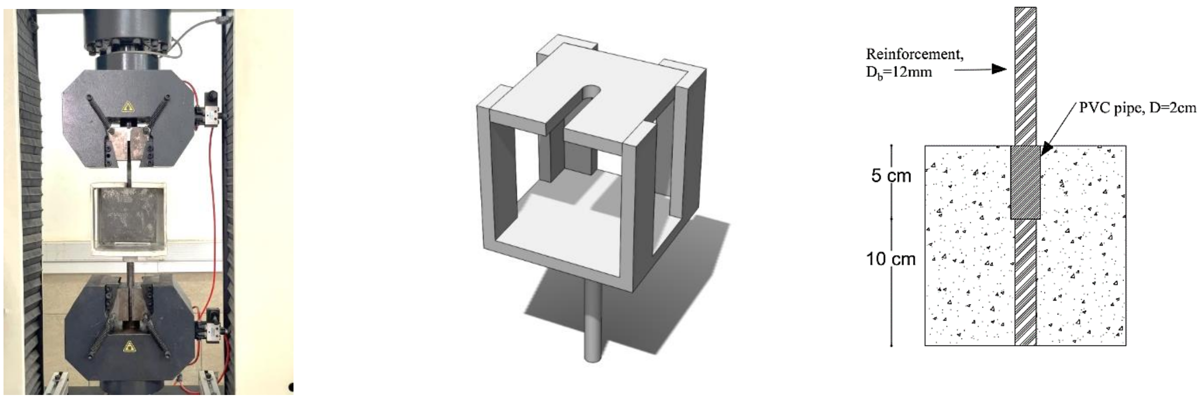

Fig. 3. Test setup and specimen for direct pull out test.

Table 6
Compressive strength of Mixes at 28 days and 90 days.

Mixes	28 days (MPa)	90 days (MPa)	Density(kg/m^3)
C	35	37	2403
CM	31	42	2407
H25M	37	45	2653
H75M	30	37	3169
H100M	28	35	3589

3. Results and discussion

3.1. Compressive strength

The compressive strength results of the samples are presented in Table 2. Figure 2 illustrates the ratio of the compressive strength of each sample to that of the control sample. At 28 days, all samples except the one containing 25% iron pellets exhibited lower compressive strength than the control. The compressive strength ratios for samples H75M and H100M were 0.86 and 0.8, respectively, indicating a maximum strength reduction of 20% when all aggregate was replaced. In contrast, sample H25M showed a 6% increase in compressive strength, suggesting an effective synergy between iron and conventional aggregates in load-bearing capacity.

At 90 days, similar to the 28-day results, the compressive strength of the H25M sample exceeded that of the control sample, showing a significant 22% increase compared to the control. This represents a notable improvement over its 28-day performance. The compressive strength of the H75M sample matched that of the control, while the H100M sample exhibited only a 5% reduction. Overall, the negative effects of using iron aggregate diminished over time, with the samples achieving acceptable strength levels by 90 days. The inclusion of micro silica further enhanced strength development, as evidenced by the results at 90 days. For instance, the control sample without micro silica showed a strength increase from 35 MPa to 37 MPa, whereas the CM sample (with micro silica) demonstrated a more substantial increase from 31 MPa to 42 MPa, highlighting the activation of micro silica's pozzolanic properties. This trend was also observed in samples containing iron aggregate.

Consistent with findings from other studies (references), increasing the proportion of iron aggregate generally reduces compressive strength. However, the strength reduction observed in this study was less pronounced than values reported elsewhere, likely due to the beneficial effects of micro silica (references). For example, Karami et al. reported that the use of naphthalene-based superplasticizers in samples containing iron pellets contributed to increased strength.

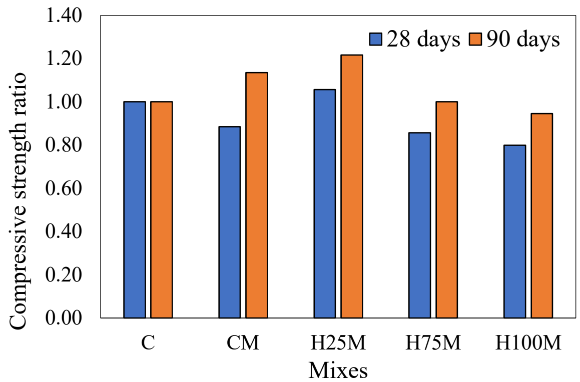

Fig. 4. Compressive strength ratio of specimens to reference specimen

3.2. Bond strength

Based on the experimental setup illustrated in Figure 3, the maximum force sustained by the rebar prior to failure was recorded. The ultimate bond strength, τ_u (in MPa), was calculated using the following equation:

$$t_u = F/(\pi L_d D_b) \quad (1)$$

where F is the maximum force sustained by the specimen (in N), D_b is the rebar diameter (in mm), and L_d is the embedment length of the rebar in contact with the concrete (in mm). For the specimens in this study, L_d was set to 100 mm, and D_b was 14 mm.

Table 3 presents the bond strength values calculated using the maximum force obtained from the direct pull-out test and Equation (1) at 28 and 90 days. The results indicate that, at 28 days, the bond strength of all samples exceeded that of the control sample, with the highest bond strength of 10.25 MPa observed for the H25M sample. As the proportion of iron pellets increased, the bond strength decreased, reaching 8.25 MPa and 8.10 MPa for the H75M and H100M samples, respectively. The inclusion of micro silica also enhanced bond strength at this age, the control sample showing an approximately 9% improvement.

By 90 days, bond strength increased further, likely due to the activation of pozzolanic reactions and the greater contribution of micro silica. The bond strength increased by 24% for samples containing 75% and 100% iron aggregate and by 43% for the sample with 25% iron aggregate. At this age, only the sample containing 25% iron aggregate exhibited higher bond strength than the micro silica-containing control sample. Compared to normal concrete (sample C), the bond strength values demonstrate the effective improvement achieved through the combined use of iron pellets and micro silica.

Table 7
Bond strength of Mixes at 28 days and 90 days, τu.

Mixes	28 days (MPa)	90 days (MPa)
C	7.52	7.92
CM	8.16	13.34
H25M	10.25	14.70
H75M	8.52	10.57
H100M	8.10	10.02

To compare the results of this study with existing empirical models, Table 4 summarizes several widely used models for calculating bond strength. As evident from the table, the most influential parameters in these models are concrete cover, rebar diameter, and concrete compressive strength. In this study, the observed failure mechanism was concrete splitting, which occurs when the maximum tensile stress around the rebar exceeds the concrete's tensile strength. Since the relationship between concrete's ultimate tensile stress and compressive strength is often expressed as a factor of fc0.5fc0.5 in the literature (references), empirical bond strength models typically incorporate this factor along with other influencing parameters. Based on the specimen configurations used in this study, Figure 7 compares the experimental bond strength values with those predicted by the empirical models.

Based on the geometry and compressive strength of specimens, Figures 4 and 5 present the bond strength values predicted by empirical models at 28 and 90 days, respectively. At 28 days, the experimental bond strength values were lower than those predicted by most models, except the model proposed by Hadi, which provided more conservative estimates.

Table 8
Bond strength models.

References	Bond strength, τ_u
Orangun et al. [14]	$0.083045\sqrt{f_c'}\left[1.2+3\left(\frac{c}{d_b}\right)+50\left(\frac{d_b}{L_d}\right)\right]$
Darwin et al. [15]	$0.083045\sqrt{f_c'}\left[\left(1.06+2.12\left(\frac{c}{d_b}\right)\right)+\left(0.92+.08\left(\frac{C^*_{max}}{C_{min}}+75\left(\frac{d_b}{L_d}\right)\right)\right)\right]$
Hadi [16]	$0.083045\sqrt{f_c'}\left[22.8-0.208\left(\frac{c}{d_b}\right)-38.212\left(\frac{d_b}{L_d}\right)\right]$
Esfahani, & Rangan [17]	$8.6\left(\frac{\frac{c}{d_b}+.5}{\frac{c}{d_b}+5.5}\right)f_{ct}$
Diab et al. [18]	$\sqrt{f_c'}\left[0.1377+0.1539\left(\frac{c}{d_b}\right)+2.673\left(\frac{d_b}{L_d}\right)+1.053\left(\frac{h_r}{s_r}\right)\right]$

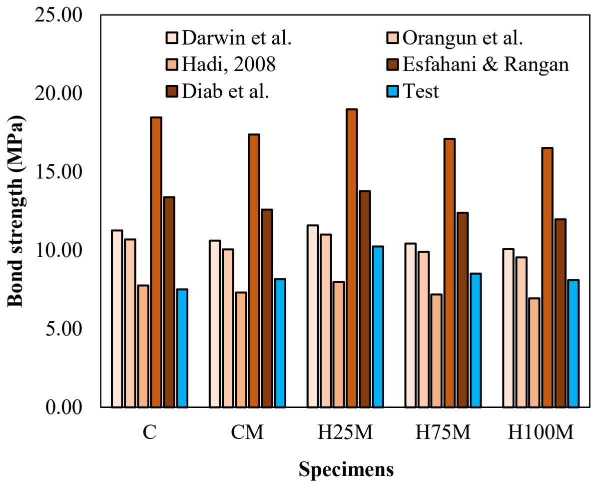

Fig. 5. Bond strength based on some available models and test result at 28 days.

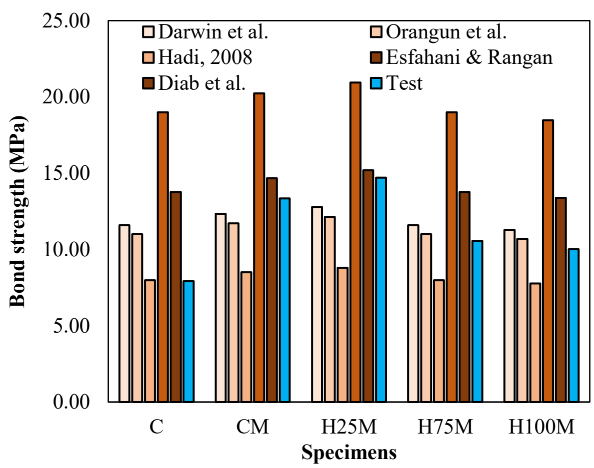

Fig. 6. Bond strength based on some available models and test result at 90 days.

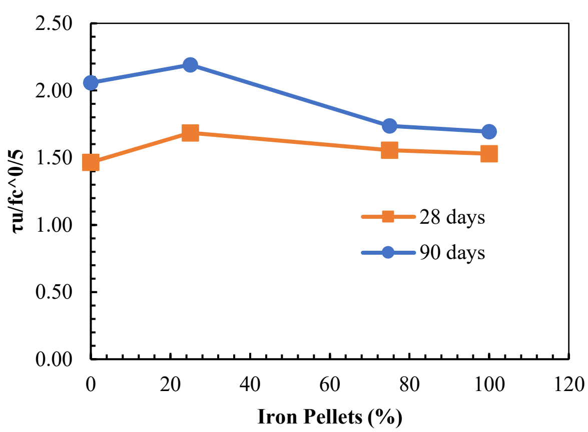

Fig. 7. Bond strength based on percentage of Iron Pelts.

Given the minor discrepancy between Hadi's model and the experimental results, this model can be reasonably applied to other aggregate percentages. By 90 days, the bond strength for the H25M sample exceeded the predictions of most models. However, for samples containing higher proportions of iron aggregate, the experimental values remained consistent with or slightly below the model predictions.

Conclusions

In this study, the compressive strength and bond strength of heavyweight concrete incorporating varying amounts of iron pellets were evaluated at 28 and 90 days using direct pull-out tests. The following general findings were obtained:

- Replacing all aggregate with iron pellets resulted in a 20% reduction in compressive strength, whereas replacing 25% of the aggregate with iron pellets led to a 6% increase in compressive strength at 28 days.
- Increasing the concrete age to 90 days, combined with the addition of micro silica, enhanced the compressive strength of the samples, mitigating the strength reduction caused by iron pellets. In the sample containing 25% iron pellets, the compressive strength exceeded that of the control sample by 20%.
- The inclusion of iron pellets improved bond strength at all ages, with the highest bond strength observed in the sample containing 25% iron pellets. Although bond strength decreased as the percentage of iron pellets increased, it remained higher than that of the control sample without micro silica.
- The combination of micro silica and iron pellets further increased bond strength.

References

[1] Zhou, K.-P., Yi, W.-J., Hwang, H.-J. and Zhou, Y., "Influence of bond test methods on the bond performance between reinforcing bars and concrete", in Structures, Elsevier. Vol. 54, No., (2023), 1299-1311. https://doi.org/10.1016/j.istruc.2023.05.083

[2] Syll, A.S. and Kanakubo, T., "Impact of corrosion on the bond strength between concrete and rebar: A systematic review", Materials, Vol. 15, No. 19, (2022), 7016. https://doi.org/10.3390/ma15197016

[3] Hosseini, S.A. and Etedali, S., "Laboratory evaluation of bond strength between rebar and concrete containing limestone powder", Amirkabir J Civ Eng, Vol. 52, No. 9, (2019), 10-10. https://doi.org/10.22060/ceej.2019.16315.6186

[4] Rao, G.A., Pandurangan, K., Sultana, F. and Eligehausen, R., "Studies on the pull-out strength of ribbed bars in high-strength concrete", Proc. of FraMCoS-6, Vol., No., (2007), 295-301

[5] Sonebi, M., Davidson, R. and Cleland, D., "Bond between reinforcement and concrete–influence of steel corrosion", in International conference on Durability of building Materials and Components, Porto–Portugal. Vol., No., (2011), 1-8

[6] Zhao, J., Luo, X., Wang, Z., Feng, S., Gong, X. and Shumuye, E.D., "Experimental study on bond performance of carbon-and glass-fiber reinforced polymer (cfrp/gfrp) bars and steel strands to concrete", Materials, Vol. 14, No. 5, (2021), 1268
[7] Hosseini, S.A. and Bagheri, M., "The effect of fly ash on the bond strength of steel reinforcement and concrete", Iranian Journal of Science and Technology, Transactions of Civil Engineering, Vol. 46, No. 1, (2022), 285-292. https://doi.org/10.1007/s40996-021-00617-8
[8] Ahmed, K., Siddiqi, Z., Ashraf, M. and Ghaffar, A., "Effect of rebar cover and development length on bond and slip in high strength concrete", Pakistan Journal of Engineering and Applied Sciences, Vol., No., (2008),
[9] Lin, R., Yu, X., Qin, C. and Ju, Y., "Study on the bonding performance between reactive powder concrete and steel bar", in Journal of Physics: Conference Series, IOP Publishing. Vol. 2368, No. 1, (2022), 012034
[10] Wang, D., Han, L., Ju, Y., Zeng, C. and Li, Z., "Bond behavior between reinforcing bar and reactive powder concrete", Structural Concrete, Vol. 23, No. 4, (2022), 2630-2642
[11] Rosyidah, A., Tjondro, J.A. and Sucita, I.K., "The bond strength of steel bar base on rib geometry bar in pullout test", Stavební obzor-Civil Engineering Journal, Vol. 30, No. 1, (2021),
[12] Burdziński, M. and Niedostatkiewicz, M., "Experimental-numerical analysis of the effect of bar diameter on bond in pull-out test", Buildings, Vol. 12, No. 9, (2022), 1392
[13] Hou, L., Sun, H., Liu, G., Huang, T. and Chen, D., "Bond strength of deformed reinforcement embedded in steel fiber reinforced concrete: Influencing factors and prediction model", Construction and Building Materials, Vol. 407, No., (2023), 133436
[14] Orangun, C., Jirsa, J. and Breen, J., "A reevaulation of test data on development length and splices", in Journal Proceedings. Vol. 74, No. 3, (1977), 114-122
[15] Darwin, D., McCabe, S.L., Idun, E.K. and Schoenekase, S.P., "Development length criteria: Bars not confined by transverse reinforcement", ACI structural Journal, Vol. 89, No., (1992), 709-709
[16] Hadi, M.N., "Bond of high strength concrete with high strength reinforcing steel", Vol., No., (2008),
[17] Esfahani, M.R. and Rangan, B.V., "Bond between normal strength and high-strength concrete (hsc) and reinforcing bars in splices in beams", Structural Journal, Vol. 95, No. 3, (1998), 272-280
[18] Diab, A.M., Elyamany, H.E., Hussein, M.A. and Al Ashy, H.M., "Bond behavior and assessment of design ultimate bond stress of normal and high strength concrete", Alexandria Engineering Journal, Vol. 53, No. 2, (2014), 355-371

Journal of Civil Engineering Researchers

Journal homepage: www.journals-researchers.com

J-Researchers

Viscoelastic Damper Connected to Adjacent Structure with Seismic Isolation System

Hosein Sarkoyeh,[a,*] Mohammad Ali Hajarizadeh,[b] Saeed Alaie[c]

[a] Department of Civil Engineering,Cha.C.,Islamic Azad univerity, Chalus, Iran

[b]Department of Civil Engineering, Bu.C.,Islamic Azad univerity, Bushehr, Iran

[c]Department of Civil Engineering, Ah.C.,Islamic Azad univerity, Ahvaz, Iran

ABSTRACT

Base isolation solutions are efficient alternatives for seismic protection of buildings and for enhancing resilient capacity. Currently, seismic isolation is primarily focused on the critical infrastructure of public health, transportation, education, and other essential sectors. The seismic response of a base-isolated structure with a storied configuration to various types of isolation systems, connected via viscoelastic dampers to an adjacent dissimilar base-isolated or fixed base structure, is investigated. The multi-storied structures are modelled as a shear-type structure with lateral degree of freedom at each floor, which are connected at different floor levels by viscoelastic dampers. The variation of top-floor absolute acceleration of both the buildings and bearing displacement under different real earthquake ground motions is computed to study the behavior and effectiveness of the resulting connected system. It is concluded that connecting two adjacent base-isolated buildings with viscoelastic dampers is beneficial in controlling large horizontal base displacements in base-isolated structures, thereby preventing isolator damage that can arise from large displacements or pounding with adjacent ground structures during earthquakes. The viscoelastic damper connection between adjacent structures is found to be most effective when the adjacent base-isolated and fixed base buildings are connected. Such a scheme is hence useful in upgrading the seismic performance of existing fixed-base structures adjacent to a base-isolated structure

ARTICLE INFO

Received: February 21, 2025
Accepted: June 02, 2025

Keywords:
Earthquake
Elastomeric Bearing
Isolation System
Sliding System
Retrofit
Viscoelastic Damper

DOI: 10.61186/JCER.7.3.76
DOR: 20.1001.1.2538516.2025.7.3.7

1. Introduction

The conventional earthquake-resistant design technique is based on the philosophies that structural safety must be assured in extreme earthquakes and that structural damage should be minimized or avoided in moderate earthquakes. To satisfy these design criteria, a structure needs to be designed with sufficient strength to withstand earthquake forces, adequate ductility to absorb earthquake energy, and appropriate stiffness to maintain structural integrity and serviceability. The dynamic response of a base-isolated structure, therefore, is considerably reduced when compared to its counterpart, the fixed-base structure, as documented in the literature available on base isolation [1-

* Corresponding author. Tel.: +9889111944420; e-mail: hosein.sarkoyeh@gmail.com.

2]. Base isolation has been widely accepted as one of the most widely accepted seismic protection systems that should substantially dissociate a superstructure from its substructure resting on a shaking ground, thereby sustainably preserving entire structures against earthquake forces as well as inside non-structural integrities. Base isolation devices can operate very effectively against near-fault (NF) ground motions with large velocity pulses and permanent ground displacements. [3] The earthquake caused large acceleration values at stories in stiff buildings and caused large inter-story drift values in soft buildings. In the seismic rehabilitation of structures, instead of increasing the bearing capacity of the structure under lateral forces, the forces acting on it can be reduced. [4] In seismic isolation, the fundamental frequency is lowered and kept away from the predominant frequency range of most earthquake ground motions. Although with the decreasing frequency, floor accelerations are reduced, helping to limit the structure damages, the increased displacement at the isolation level calls for the necessity of maintaining an adequate separation gap distance to accommodate the large bearing displacement. The separation gap requirement in case of a base-isolated structure is therefore more than that of the fixed-base structure. In modern cities, however, due to a high value of land space, limited availability of land, and preference for centralized services, there is a tendency to construct buildings nearby without maintaining proper separation gaps. During an earthquake event, these buildings vibrate vigorously and may become a cause for severe damage because of mutual pounding. The 1985 Mexico City and 1989 Loma Prita earthquakes are typical examples of the large-scale damage caused by structural pounding. Given this, the building codes made stringent requirements for base-isolated structures, specifying accommodation of larger bearing displacements during maximum capable earthquakes and the need for supplemental damping devices. In overcoming this dilemma, the present study suggests the use of viscoelastic damper connections between the adjacent buildings.

The papers reported by Housner et al [5] and Soong and Spencer [6] provide a detailed review of earlier and recent studies made on structural control and supplemental energy dissipation devices and their applications to seismic protection. To avoid pounding damages, the concept of linking adjacent fixed-base buildings is introduced and verified analytically and experimentally by a number of researchers [7-8]. However, mitigation of pounding and›or /or impact damages in case of base isolated and adjacent structures through incorporation of damper links ages between them is untried yet. Therefore, it would be interesting to investigate the effectiveness of connecting the base-isolated building with the adjacent building as an alternative for the protection against possible destruction due to pounding because of an inadequate separation gap provided between the two, and improving the seismic performance of the existing fixed base buildings.

This paper investigates the advantages of connecting the base-isolated building to the adjacent base-isolated or fixed-base building using viscoelastic dampers. The main objectives of this study are to investigate the dynamic characteristics of a base-isolated building connected to the adjacent base-isolated or fixed-base building by discrete linear viscoelastic dampers and to propose this scheme for seismic retrofit of existing earthquake-prone fixed-base structures.

2. Modelling of adjacent structures

Fig. 1 shows the two structural models under consideration, depicting multi-degree-of-freedom shear models with rigid floors. Fig. 1(a) shows the I-story base isolated building connected through viscoelastic dampers at different floors to the adjacent story base isolated building. In Fig. 1(b), a similar viscoelastic damper connected system with the story base isolated buckling mounted on various isolation systems connected to the adjacent m-story fixed base building is shown, along with the schematic of a typical viscoelastic damper. The masses in these models are assumed to be lumped at each floor level, and the stiffness is provided by axially inextensible massless columns. Both the adjacent connected buildings are assumed to behave linearly elastically and receive the same earthquake ground motion horizontally. The soil structure interaction effects are not taken into consideration. For both buildings, the mass at all floor levels is kept constant while the stiffness is varied to achieve the desired fundamental periods under a fixed base condition. These adjacent buildings are connected at different floor levels by linear viscoelastic dampers to serve as an energy dissipation mechanism.

2.1. Damping devices

Energy dissipation devices are of different types and may be categorized depending on the type of material used to transform energy, such as: viscous, viscoelastic, friction, metallic yielding, and magnetic dampers. In viscous and viscoelastic dampers, the viscous›. A viscoelastic material, in the form of either liquid (silicone or oil) or solid (special rubbers or acrylics), is provided. Friction devices contain interface materials, such as steel-to-steel. copper with graphite-to-steel, or brake pad-to-steel. Metallic yielding devices most commonly use mild steel plates in different shapes and materials such as lead, shape memory alloys, etc. The magnetic damper functions on the principle of magnetism of fluid particles, as seen in the

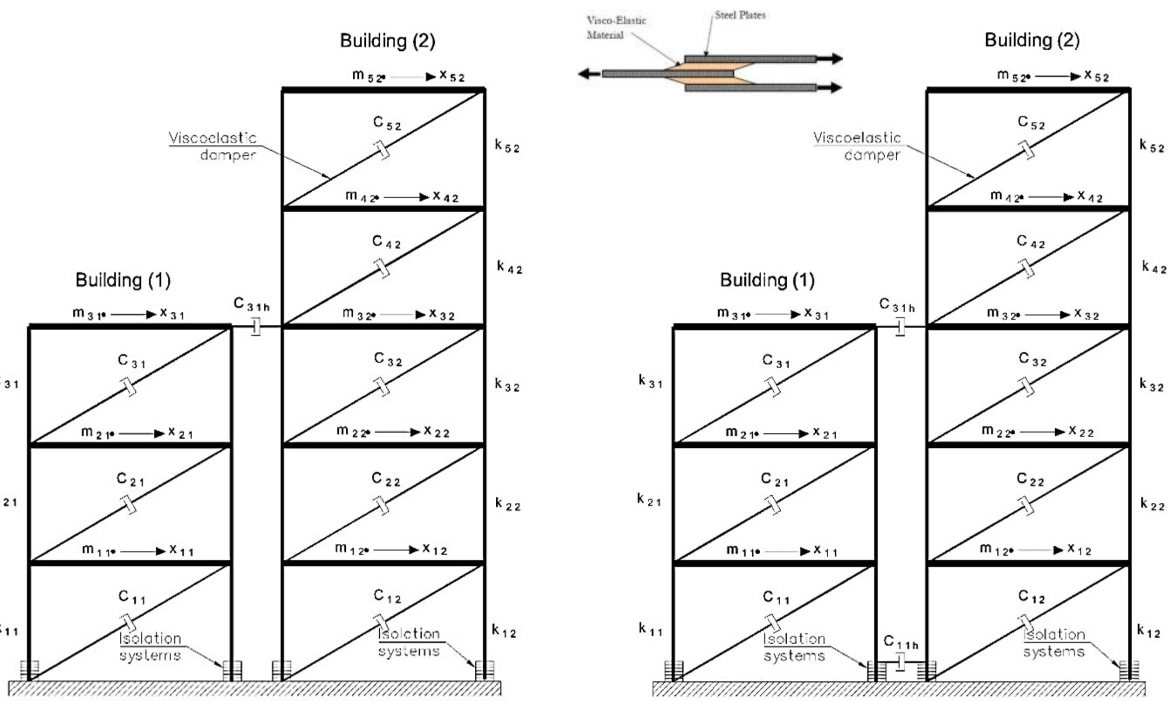

(a) Two base-isolated buildings

(b) Base-viscoelastic and Two base-isolated buildings

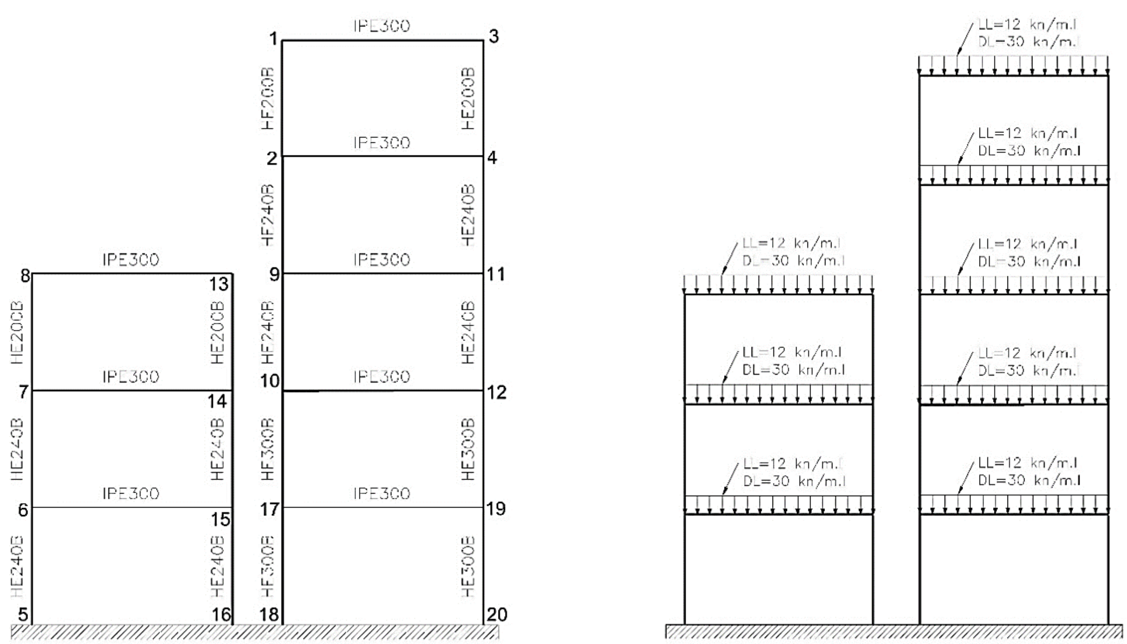

(c) Node number - frame sections

(d) Living and dead forces entering the frame

Fig 1. Mathematical model of viscoelastic damper connected adjacent buildings magnetorheological dampers. In the present study, the viscoelastic dampers are investigated for their usefulness in seismic response mitigation when used as connecting linkages between the two adjacent structures.

2.2. Viscoelastic damper

The viscoelastic solid materials are used as a means to dissipate energy in viscoelastic dampers [9- 10]. The viscoelastic materials generally used are copolymers or glassy substances. The energy is dissipated through shear deformation of the viscoelastic layers. Its behavior depends upon vibration frequency, strain levels, and temperature. However, the overall behavior of viscoelastic dampers can be represented by using a spring dashpot element acting in parallel. The typical viscoelastic damper consists of viscoelastic layers bonded with steel plates or solid thermoplastic rubber sheets sandwiched between steel plates; refer to Fig. 1(b). While in an active state, the relative motion between the central and outer plates gives rise to shear deformations in the viscoelastic fluid between these interfaces, and consequently, the energy is dissipated, leading to seismic response mitigation.

2.3. Damping force

The force generated in the viscoelastic damper comprises two components: elastic force and damping force. The elastic force is proportional to the relative displacement between the connected floors, whereas the damping force is essentially proportional to the relative velocity of the piston head concerning the damper casing. Hence, the damper force can be expressed as:

$$F_d = [K_d]\{Ub.U1.U2.\ldots.Ul\}^T + [C_d]\{\dot{U}b.\dot{U}1.\dot{U}2.\ldots.\dot{U}l\}^T \quad (1)$$

The vectors of relative displacement and velocity between the damper-connected floors of the adjacent buildings, and the over-dot denotes the derivative concerning time. Here, the stiffness elements of dampers placed along the height of the adjacent structures are:

$$[K_d] = \text{diag}\,[k_{db}, k_{d1}, k_{d2}, \ldots, k_{dl}] \quad (2)$$

where k_{db} , k_{d1} , k_{d2}, … , k_{dl} are the damper stiffness coefficients at the different floor levels. In addition, the damper damping matrix for the array of dampers placed along the height of the adjacent structures is expressed as:

$$[C_d] = \text{diag}\,[c_{db}, c_{d1}, c_{d2}, \ldots, c_{dl}] \quad (3)$$

where c_{db}, c_{d1}, c_{d2}, …, c_{dl} are the damper damping coefficients levels.

The total external damper stiffness and external damping added in the form of connection linkages between two adjacent buildings and are expressed respectively as a non-dimensional parameter

$$K_d = \frac{K_{db} + \sum K_{dj}}{\omega_e^2 \sum M_i} \qquad (I = 1,2 \text{ and } j = 1, L) \quad (4)$$

$$\eta_d = \frac{C_{db} + \sum C_{dj}}{2\xi\omega_e^2 \sum M_i} \qquad (I = 1,2 \text{ and } j = 1, L) \quad (5)$$

Where $M_i = m_{bi} + \sum_{j=1}^{l \text{ or } m} m_{ji}$ is the total mass of the base isolated building; m_{ji} is the mass of 5th floor of ith building, ω_e is the equivalent isolation frequency considered as π rad/sec; ξ_e is the equivalent viscous damping ratio taken as 15% This implies that the total external damper damping and damper stiffness is expressed in proportion with properties of an equivalent linear viscous rubber isolation system having damping ratio of 15% and isolation time period of 2 sce.

3. Governing equations of motion

For the systems under consideration, the governing equations of motion are obtained by considering the equilibrium of forces at the location of each degree of freedom during seismic excitations. Two individual cases of governing equations of motion for such systems under earthquake excitation are given below.

3.1. Unconnected building systems

When the adjacent buildings are not connected with any link, they act independently, and for such unconnected base-isolated buildings, the following two sets of governing equations of motion can be obtained, which are of order L and m, the degrees of freedom for adjacent base-isolated Buildings 1 and 2, respectively, under earthquake excitation.

The isolation layer forces for three different types of isolation systems used in the present study, namely, high-damping rubber bearings (HDRB), lead-rubber bearings (LRB), and friction pendulum systems (FPS), are placed under the base isolated buildings. For a fixed base building, the corresponding isolation in the above governing equations of motion with appropriate modifications in the mass, stiffness, and damping matrices.

3.2. Connected building system

Owing to the introduction of viscoelastic dampers as connecting links at the superstructure of the two adjacent buildings, it converts to a connected isolated system with (1+m) lateral degrees of freedom.

$$[M]\{\ddot{x}\} + [C]\{\dot{x}\} + [K]\{x\} + [F] = -[M]\{r\}(\ddot{x_g}) \quad (6)$$

The unknown floor displacement, velocity, and acceleration vectors for the adjacent connected Buildings 1 and 2, respectively. In Eq. (6), the mass matrix. [M] for the combined system is obtained by.

$$[M] = \begin{bmatrix} [M]_1 & [O]_1 \\ [O]_2 & [M]_2 \end{bmatrix} \quad (7)$$

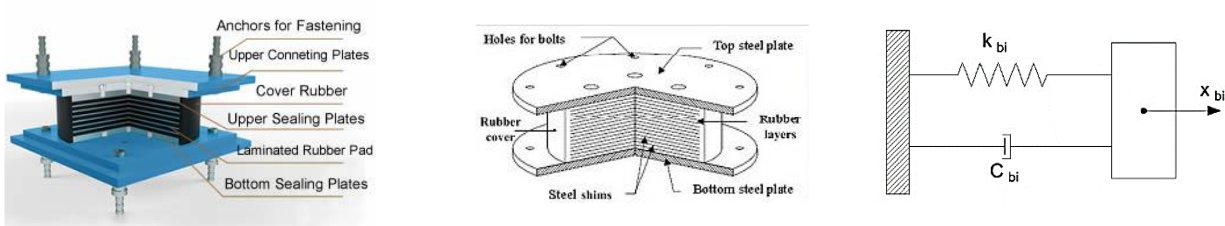

(a) HDRB

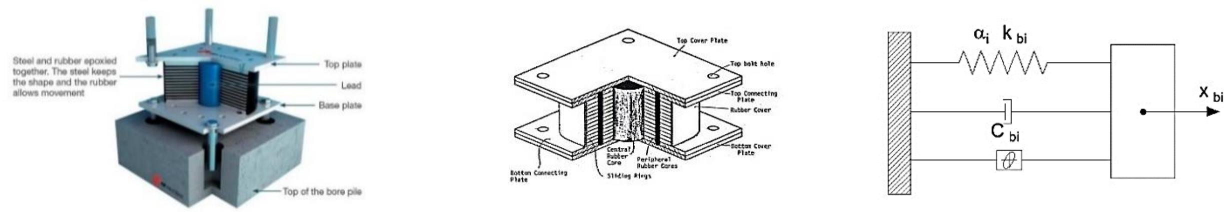

(b) LRB

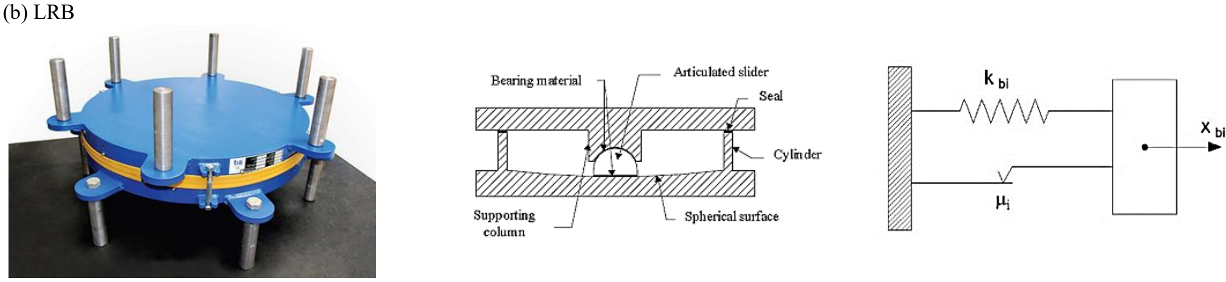

(c) FPS

Fig 2. Schematic models of isolation systems (a) HDRB (b) LRB and (c) FPS

where $[M_1]$ and $[M_2]$ are the individual diagonal mass matrices for the adjacent Buildings 1 and 2, respectively; $[O_1]$ and $[O_2]$ are the null matrices of order (L* m) and (m * L) respectively. The stiffness matrix for the connected system is expressed as.

$$[M]=\begin{bmatrix}[M]_1 & [O]_1\\ [O]_2 & [M]_2\end{bmatrix}+\begin{bmatrix}[K]_d & -[K]_d & [O]_3\\ -[K]_d & [K]_d & [O]_4\\ [O]_5 & [O]_6 & [O]_7\end{bmatrix} \quad (8)$$

where $[K_1]$ and $[K_2]$ are the stiffness matrices for the adjacent Buildings 1 and 2, respectively; and $[K_d]$ is as explained in eq (2).

$$[M]=\begin{bmatrix}[C]_1 & [O]_1\\ [O]_2 & [C]_2\end{bmatrix}+\begin{bmatrix}[C]_d & -[C]_d & [O]_3\\ -[C]_d & [C]_d & [O]_4\\ [O]_5 & [O]_6 & [O]_7\end{bmatrix} \quad (9)$$

where $[C_1]$ and $[C_2]$ are the damping matrices for the adjacent Buildings 1 and 2, respectively; and $[C_d]$ is as explained in eq (3). The bearing force vector for com bind system is

$$\{F\}=\begin{Bmatrix}\{F_{b1}\}\\ \{F_{b2}\}\end{Bmatrix} \quad (10)$$

The isolation layer forces $\{F_{b1}\}$ and $\{F_{b2}\}$ for three different types of isolation systems used the present study such as high damping rubber bearings, lead rubber bearings and friction pendulum systems under the adjacent buildings are derived as follows.

3.3. High-damping rubber bearing

The high-damping rubber bearing (HDRB) represents the commonly used elastomeric bearings. The basic components of HDRB are steel and rubber plates built in the alternate layers [11-12]. The dominant feature of HDRB is the parallel action of linear spring and damping as shown schematically in Fig. 2(a). The HDRB exhibits high damping capacity, horizontal flexibility, and high vertical stiffness. The damping constant of the system varies considerably with the strain level of the bearing (generally of the order of 15%). The system operates by decoupling the structure from the horizontal components of earthquake ground motion by interposing a layer of low horizontal stiffness between the structure and its foundation. The isolation effects in this type of system are produced not by absorbing the earthquake energy, but by deflecting through the system dynamics. Usually, there is a large difference in the damping of the structure and the isolation device, which makes the system non-classically damped.

The stiffness and damping of the HDRB are selected to provide the specific values of the two parameters characterizing the system namely the isolation time period (T_{bi}) and damping ratio (ξ_{bi}) defined as

$$T_{bi} = 2\pi\sqrt{\frac{M_i}{K_{bi}}} \qquad (i = 1 , 2) \qquad (11)$$

$$\xi_{bi} = \frac{C_{bi}}{2M_i\ \omega_{bi}} \qquad (i = 1 , 2) \qquad (12)$$

where $\omega_{bi} = \frac{2\pi}{T_{bi}}$ is the isolation frequency.

3.4. Lead-rubber bearing

The second category of elastomeric bearings is lead-rubber bearings [13]. Lead-plug rubber bearings were invented in New Zealand in 1975. The mechanism of lead-plug rubber bearings is very similar to that of low-damping natural rubber bearings. [14] This kind of frictional isolator has a sliding hinge part that slides on a spherical steel surface. The surface of the upper sliding part, which is in contact with the depression of the isolator during the time. [15] as shown schematically in Fig. 2(b). This system provides the combined features of vertical load support, horizontal flexibility, restoring force, and damping in a single unit. These bearings are similar to the HDRB, but a central lead core is used to provide an additional means of energy dissipation. The energy-absorbing capacity of the lead core reduces the lateral displacements of the isolator. The force-deformation. The behavior of the LRB is generally represented by nonlinear characteristics following a hysteretic nature. For the present study, Wen's model [16] is used to characterize the hysteretic behavior of the LRB.

where F_{yi} is the yield strength of the bearing; a_i anindex which represents the ratio of post to pre yielding stiffness; k_i the initial stiffness of the bearing: C_{bi} the viscous damping of the bearing; and Z_i is the non-dimensional hysteretic displacement component satisfying the following non-linear first order differential equation.

where q_i is the isolator yield displacement, dimension less parameters A, β , τ and are selected such that the predicted response from the model closely matches the experimentally obtained results. The parameter n is an integer constant, which controls smoothness of the transition from elastic to plastic response.

3.5. Friction pendulum system

One of the most popular and effective techniques for seismic isolation is the use of sliding isolation vices. The sliding systems exhibit an excellent performance under a variety of severe earthquake loading and are very effective in reducing large levels of the superstructure acceleration. These isolators are characterized by insensitivity to the frequency content of earthquake excitation because of the tendency of a sliding system to reduce and spread the earthquake energy over a wide range of frequencies. Another advantage of sliding isolation systems over conventional rubber bearings is the development of the frictional force at the base; it is proportional to the mass of the structure, and the center of mass and center of resistance of the sliding support coincide. Consequently, the torsional effects produced by the asymmetric building are diminished. The concept of sliding bearings is combined with the concept of a pendulum-type response, resulting in a conceptually interesting seismic isolation system known as a friction pendulum system (FPS) [17], as shown schematically in Fig. 2(c). In FPS, the isolation is achieved by means of an articulated slide on a spherical, concave chrome surface. The slide is faced with a bearing material which, when in contact with the polished chrome surface, results in a friction force, while the concave surface produces a restoring force. The resisting force provided by the FPS is:

$$F_{bi} = k_{bi}\ X_{bi} + F_{Xi} \qquad (I = 1 , 2) \qquad (13)$$

where k_{bi} is the bearing stiffness provided by virtue of inward gravity action at the concave surface: F_{Xi} is the frictional force at slide and polished chrome surface junction.

The system is characterized by isolation time period (T_{bi}) that depends upon radius of curvature of concave surface and friction coefficient (μ_i). The isolation stiffness k_{bi} is adjusted and the specified value of the isolation time period evaluated by the Eq. (11) is achieved.

4. Solution of equations of motion

Classical modal superposition technique cannot be employed in the solution of equations because the system is not classically damped due to the difference in damping in the isolation system as compared to the damping in the superstructure of a base-isolated building, as well as the damper links. Therefore, for different earthquakes, the equations of motion are solved numerically using Newmark's method of step-by-step integration, adopting linear variation of acceleration over a small-time interval of Ar. The time interval for solving the equations of motion is taken as 0.02/20 sec (ie Δt 0.001 sec). At each time instant, the responses, namely the accelerations and displacements are obtained at each floor level of the two adjacent buildings.

5. Numerical study

The seismic response of two adjacent multi-storied buildings, connected using viscoelastic dampers, either

Table 1.
Mechanical specifications of isolators used in 3-story and 5-story structures

position	Load applied to the column	Lead core yield strength	Yeld strenght	stiffnes	Effective stiffness	Effective periodicity	Effective damping ratio	Effective damping
	W	Q	Fy	K0	Keff	Teff	xeff	Ceff
	(ton)	(ton)	(kn)	(kn/m)	(kn/m)	(sec)	---	(kn.s/m)
3-storey structure	37.80	1.89	22.27	2227.16	509.42	1.71	0.16	43.81
5-storey structure	63.00	3.15	37.12	3711.94	849.03	1.71	0.16	73.02

both or one of them supported on isolation devices, is investigated here. The multi-degree-of-freedom shear models of the adjacent buildings are used, with linear viscoelastic damping devices at different floor levels in Fig. 1. The earthquake selected for this study (1) Imperial Valley Earthquake occurred on October 15, 1979, equivalent to Mehr 23, 1358, at 23:16:54 UTC in the United States, Southern California region. The depth of this earthquake was 9.3 km, and its magnitude was 6.5 on the Mw scale, and its maximum intensity was declared on the Mercalli scale IX (Violent). Its PGA value is 0.28. (2) The Kobe earthquake or the Great Hanshin earthquake is an earthquake with a magnitude of 6.8 or a magnitude of 7.3 on the Richter scale, which shook and crushed the city of Kobe in Japan on January 17, 1995, at 5:46 a.m. for 20 seconds. Its PGA value is declared as 0.671. (3) The San Fernando earthquake occurred on February 9, 1971, at 06:00:41 AM local time (14:00:41 UTC) in the San Fernando area of the United States. The depth of the earthquake was 8.4 km. Its magnitude was reported as 6.6 on the Mw scale.

5.1. The shape coefficient of the spectrum of the ground plan

According to Standard 2800 of Iran, the shape coefficient of the spectrum of the plan used in this study, type III land, and the acceleration of the plan for the area with a very high-risk area is considered 0.35. In the Figure, the shape factor of the design spectrum for all types of soils in the zone of high risk and high void can be seen.

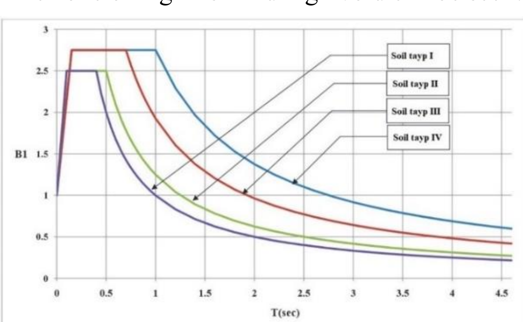

Fig 3. Shape coefficient of the design spectrum for all types of soils

5.2. Technical and mechanical specifications used in dampers and separators

A seismic isolation head and a viscoelastic damper were used to analyze 5-story and 3-story structures and observe the displacement in the structure based on 3 design earthquakes. The mechanical specifications and initial analytical results for use in the SAP2000 program are specified in the tables below. Considering the initial results and placing each of them in 3-story and 5-story structures, they were analyzed according to Figure 1.

Table 2.
Mechanical characteristics of viscoelastic dampers

Periodicity	natural frequency	Elastic stiffness	damping
T	ω	h	c
1.49	4.23	1.2	15%

Table 3.
Viscoelastic damper specifications separately in a 5-story diagonal structure

position	Stiffness of the structure	Damper stiffness	damping	Viscoelastic damper angle
	ki	k\`i	c\`i	q
1st floor	79.41	35.47	10.07	30.25
2st floor	52.83	23.60	6.70	30.25
3st floor	21.36	9.54	2.71	30.25
4st floor	14.10	6.30	1.79	30.25
5st floor	6.73	3.01	0.85	30.25

Table 4.
Viscoelastic damper specifications separately in a 3-story diagonal structure

position	Stiffness of the structure	Damper stiffness	damping	Viscoelastic damper angle
	ki	k\`i	c\`i	q
1st floor	45.38	20.27	5.75	30.25
2st floor	28.07	12.54	3.56	30.25
3st floor	45.82	20.47	5.81	30.25

Table 5.
Viscoelastic damper specifications separately in a 3-story horizontal structure

position	Stiffness of the structure ki	Damper stiffness k\`i	damping damping c\`i	Viscoelastic damper angle q
1st floor	45.38	20.27	5.75	30.25
2st floor	28.07	12.54	3.56	30.25
3st floor	45.82	20.47	5.81	30.25

The following tables show the results of structural analysis in cases where a viscoelastic damper is used to connect two structures on the floor or as a metal member. Also, a seismic isolator is used in the structures at the same time, as shown in Figure 1. The amount of dead and live loads used in structural analysis is also specified in Figure 1.

5.3. Analysis of the amount of floor displacement in case of using viscos-elastic damper in the base

In the Table 6, the amount of displacement of the floors of two buildings can be seen in two cases, one in which the viscoelastic damper was used at the highest level of the shortest floor (3rd floor) and one in the case in which, in addition to the use of the viscoelastic damper at the level of the third floor, it was also used at the level of the first floor (Figure 1-b).

According to the results of Table 6, it can be seen that the effect of the amount of displacement in node 16 is incremental, which is caused by the effects of the displacement of node 18 in the amount of about 20-30% compared to the design earthquake on it. In other nodes, this amount of displacement has been reduced to about 1-7% according to the design earthquake. This is even though both structures have a seismic isolator from the floor, and the closer the viscoelastic damper is to the floor, the lower its displacement.

6. Conclusions

The amount of displacement and seismic response of adjacent buildings connected with viscoelastic dampers when both of the buildings are separated from the foundation was investigated in this study, and the following results were obtained.

- A considerable amount of reduction in earthquake displacement of the design is achieved by introducing viscoelastic damper joints in the floor surfaces of the buildings adjacent to the isolated foundation, which is useful to prevent the consequences of knocking. So that it balances the displacement of two structures.
- The effectiveness of viscoelastic dampers as connecting links is more important in the case of buildings with isolated foundations compared to two isolated buildings with adjacent connected foundations. It is very useful in retrofitting works in structures.

Table 6.
Table of displacement value of structural nodes according to design earthquake

The studied earthquake		**Imperial Valley 1979**	**Kobe 1995**	**San Fernando 1971**
Isolation system 3-story Building 1 5-story Building 2		Bearing displacement (cm)	Bearing displacement (cm)	Bearing displacement (cm)
Unconnected	point 3	5.89	43.39	14.40
	point 20	1.28	23.02	6.40
	point 13	4.80	38.88	12.67
	point 16	2.48	25.51	7.84
	point 9	4.82	38.90	12.68
	point 18	3.66	34.11	10.84
Connected	point 3	5.98	42.77	14.26
	point 20	1.24	21.62	5.95
	point 13	4.87	38.32	12.53
	point 16	3.52	31.96	10.16
	point 9	4.86	38.09	12.46
	point 18	3.55	32.28	10.26
Percentage reduction of node displacement in connection mode from the base	point 3	-1.56%	1.46%	1.02%
	point 20	3.74%	6.46%	7.62%
	point 13	-1.41%	1.47%	1.07%
	point 16	-29.66%	-20.18%	-22.85%
	point 9	-0.81%	2.14%	1.75%
	point 18	3.10%	5.66%	5.61%

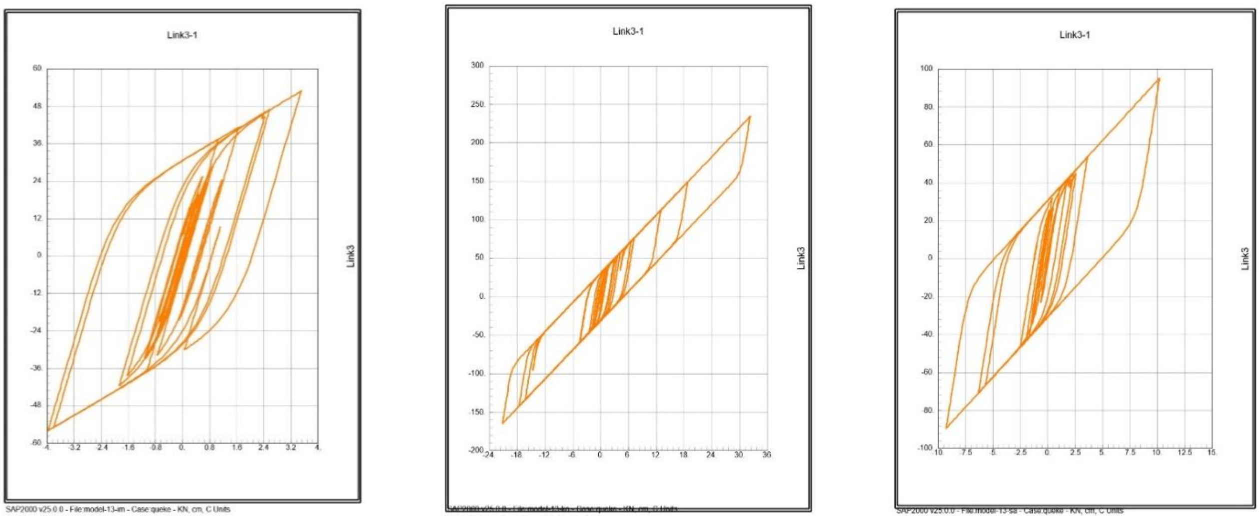

(a) Earthquake Imperial Valley 1979 (b) Earthquake Kobe 1995 (c) Earthquake San Fernando 1971

Fig 4. The amount of displacement in the seismic isolator in the state of connection from the base (joint 18)

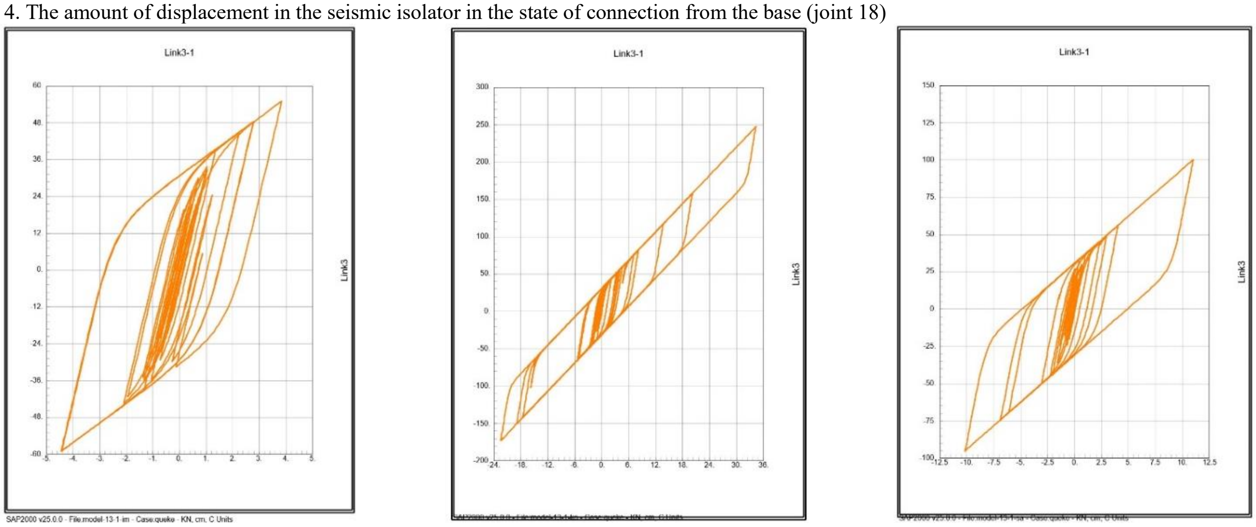

(a) Earthquake Imperial Valley 1979 (b) Earthquake Kobe 1995 (c) Earthquake San Fernando 1971

Fig 5. The amount of displacement in the seismic isolator in the state of disconnection from the base (joint 18)

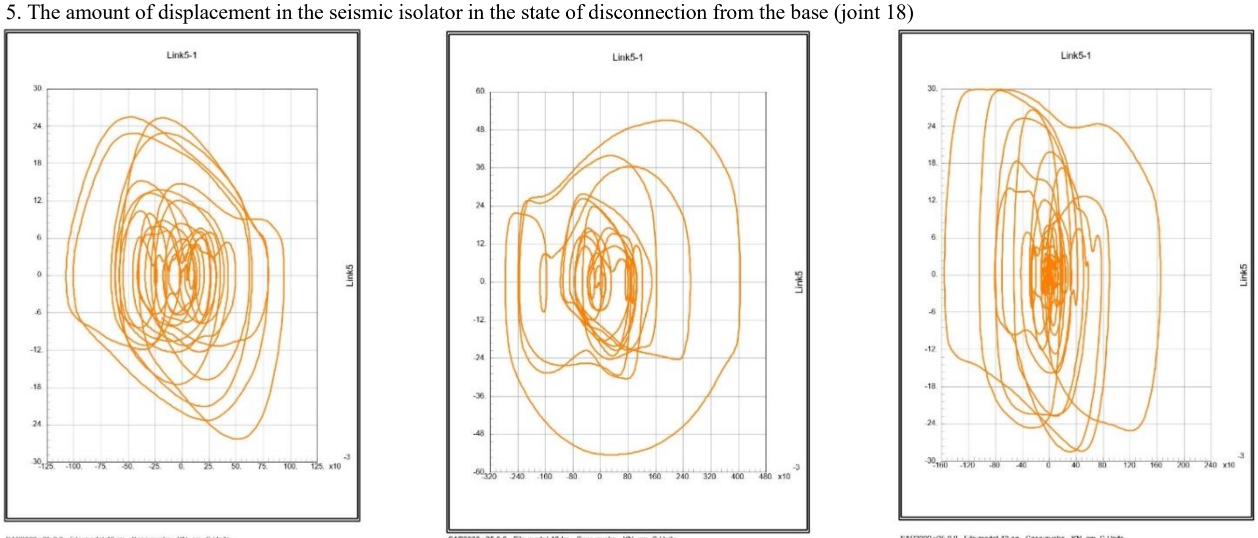

(a) Earthquake Imperial Valley 1979 (b) Earthquake Kobe 1995 (c) Earthquake San Fernando 1971

Fig 6. The amount of force in the viscoelastic damper in the connection state from the base

- The escape position of the viscoelastic damper is very useful and effective for optimizing the design during an earthquake. So that by absorbing high force during vibration, it causes more stability of the structure and also reduces the dimensions of the components of the structure.

References

[1] Kelly, James M. "Aseismic base isolation: review and bibliography." Soil Dynamics and earthquake engineering 5.4 (1986): 202-216. https://doi.org/10.1016/0267-7261(86)90006-0

[2] Jangid, R. S., and T. K. Datta. "SEISMIC BEHAVIOUR OF BASE-ISOLATED BUILDINGS: A STATE-OF-THE ART REVIEW." Proceedings of the Institution of Civil Engineers-Structures and Buildings 110.2 (1995): 186-203. https://doi.org/10.1680/istbu.1995.27599

[3] Noruzi, Faramarz, Ahmad Hasanpour, and Sahand Saeedian. "Seismic Response Assessment of high-rise RC building with Lead Rubber bearing base isolator on different soil types." Journal of Civil Engineering Researchers 0 (2017): 1-9. http://www.journals-researchers.com/ojs/index.php/jcer/article/view/23

[4] Bagherinejad, Kamyar, Shahin Charkhtab, and Seyedhamed Hosseini. "Cost Viability of a Base Isolation System for the Seismic Protection of mid-rise reinforced concrete moment frames." Journal Of Civil Engineering Researchers 1.1 (2017): 1-7. https://www.journals.researchers.com/ojs/index.php/jcer/article/view/2

[5] Housner, GWea, et al. "Structural control: past, present, and future." Journal of engineering mechanics 123.9 (1997): 897-971. https://doi.org/10.1061/(ASCE)0733-9399(1997)123:9(897)

[6] Soong, Tsu-Teh, and B. F. Spencer Jr. "Supplemental energy dissipation: state-of-the-art and state-of-the-practice." Engineering structures 24.3 (2002): 243-259. https://doi.org/10.1016/S0141-0296(01)00092-X

[7] Westermo, Bruce D. "The dynamics of inter structural connection to prevent pounding." earthquake Engineering & Structural Dynamics 18.5 (1989): 687-699. https://doi.org/10.1002/eqe.4290180508

[8] Zhang, W. S., and You Lin Xu. "Vibration analysis of two buildings linked by Maxwell model-defined fluid dampers." Journal of sound and vibration 233.5 (2000): 775-796. https://doi.org/10.1006/jsvi.1999.2735

[9] Zhang, Ri-Hui, and Tsu T. Soong. "Seismic design of viscoelastic dampers for structural applications." Journal of structural engineering 118.5 (1992): 1375-1392. https://doi.org/10.1061/(ASCE)0733-9445(1992)118:5(1375)

[10] Zhang, Ri-Hui, T. T. Soong, and P. Mahmoodi. "Seismic response of steel frame structures with added viscoelastic dampers." Earthquake engineering & structural dynamics 18.3 (1989): 389-396. https://doi.org/10.1002/eqe.4290180307

[11] Kikuchi, Masaru, and Ian D. Aiken. "An analytical hysteresis model for elastomeric seismic isolation bearings." Earthquake engineering & structural dynamics 26.2 (1997): 215-231. https://doi.org/10.1002/(SICI)1096-9845(199702)26:2<215::AID-EQE640>3.0.CO;2-9

[12] Koo, Gyeong-Hoi, et al. "Evaluation of laminated rubber bearings for seismic isolation using modified macro-model with parameter equations of instantaneous apparent shear modulus." Engineering structures 21.7 (1999): 594-602. https://doi.org/10.1016/S0141-0296(98)00006-6

[13] Robinson, William H. "Lead-rubber hysteretic bearings suitable for protecting structures during earthquakes." Earthquake engineering & structural dynamics 10.4 (1982): 593-604. https://doi.org/10.1002/eqe.4290100408

[14] Bagherinejad, Kamyar, Shahin Charkhtab, and Seyedhamed Hosseini. "Cost Viability of a Base Isolation System for the Seismic Protection of mid-rise reinforced concrete moment frames." Journal Of Civil Engineering Researchers 1.1 (2017): 1-7. https://www.journals.researchers.com/ojs/index.php/jcer/article/view/2

[15] Khanloo, Mehdi, Amir Masoud Hosseini, and Mohammed Reza Oliaei. "A study on effects of base isolators and dampers on steel structures design." Journal of Civil Engineering Researchers 1.4 (2017): 17-23. https://www.journals-researchers.com/ojs/index.php/jcer/article/view/19

[16] Wen, Yi-Kwei. "Method for random vibration of hysteretic systems." Journal of the engineering mechanics division 102.2 (1976): 249-263. https://doi.org/10.1061/JMCEA3.0002106

[17] Zayas, Victor A., Stanley S. Low, and Stephen A. Mahin. "A simple pendulum technique for achieving seismic isolation." Earthquake spectra 6.2 (1990): 317-333. https://doi.org/10.1193/1.1585573

Author Guidelines EditEdit Author Guidelines

GENERAL GUIDELINES FOR AUTHORS

Journal of civil engineering researches invites unsolicited contributions of several forms: articles, reviews and discussion articles, translations, and fora. Contributions should fall within the broad scope of the journal, as outlined in the statement of scope and focus. Contributors should present their material in a form that is accessible to a general anthropological readership. We especially invite contributions that engage with debates from previously published articles in the journal.

Submissions are double-blind peer-reviewed in accordance with our policy. Submissions will be immediately acknowledged but due to the review process, acceptance may take up to three months. Submissions should be submitted via our website submission form (see links above for registration and login). Once you login, make sure your user profile has "author" selected, then click "new submission" and follow the instructions carefully to submit your article. If problems arise, first check the FAQ and Troubleshooting guide posted below. If you are still experiencing difficulty, articles can be submitted to the editors as email attachments.

Each article should be accompanied by a title page that includes: all authors' names, institutional affiliations, address, telephone numbers and e-mail address. Papers should be no longer than 10,000 words (inclusive of abstract 100-150 words, footnotes, bibliography and notes on contributors), unless permission for a longer submission has been granted in advance by the Editors. Each article must include a 100 words "note on contributor(s)" together will full institutional address details, including email address. We request that you submit this material (title page and notes on the contributors) as "supplementary files" rather than in the article itself, which will need to be blinded for peer-review.

We are unable to pay for permissions to publish pieces whose copyright is not held by the author. Authors should secure rights before submitting translations, illustrations or long quotes. The views expressed in all articles are those of the authors and not necessarily those of the journal or its editors. After acceptance, authors and Special Issue guest editors whose institutions have an Open Access library fund must commit to apply to assist in article production costs. Proof of application will be requested. Though publication is not usually contingent on the availability of funding, the Journal is generally under no obligation to publish a work if funding which can be destined to support open access is not made available.

Word template and guidelines

Our tailored Word template and guidelines will help you format and structure your article, with useful general advice and Word tips.

(La)TeX template and guidelines

We welcome submissions of (La)TeX files. If you have used any .bib files when creating your article, please include these with your submission so that we can generate the reference list and citations in the journal-specific style

Artwork guidelines

Illustrations, pictures and graphs, should be supplied with the highest quality and in an electronic format that helps us to publish your article in the best way possible. Please follow the guidelines below to enable us to prepare your artwork for the printed issue as well as the online version.

Format: TIFF, JPEG: Common format for pictures (containing no text or graphs).

EPS: Preferred format for graphs and line art (retains quality when enlarging/zooming in).

Placement: Figures/charts and tables created in MS Word should be included in the main text rather than at the end of the document.

Figures and other files created outside Word (i.e. Excel, PowerPoint, JPG, TIFF, EPS, and PDF) should be submitted separately. Please add a placeholder note in the running text (i.e. "[insert Figure 1.]")

Resolution: Rasterized based files (i.e. with .tiff or .jpeg extension) require a resolution of at least 300 dpi (dots per inch). Line art should be supplied with a minimum resolution of 800 dpi.

Colour: Please note that images supplied in colour will be published in colour online and black and white in print (unless otherwise arranged). Therefore, it is important that you supply images that are comprehensible in black and white as well (i.e. by using colour with a distinctive pattern or dotted lines). The captions should reflect this by not using words indicating colour.

Dimension: Check that the artworks supplied match or exceed the dimensions of the journal. Images cannot be scaled up after origination

Fonts: The lettering used in the artwork should not vary too much in size and type (usually sans serif font as a default).

Authors services:

For reformatting your manuscript to fit the requirement of the Journal of Civil Engineering Researchers and/or English language editing please send an email to the following address:

researchers.services@gmail.com

Noted: There is a fixed charge for these mentioned services that is a function of the manuscript length. The amount of this charge will be notified through a reply email.

FAQ AND TROUBLESHOOTING FOR AUTHORS

I cannot log in to the system. How do I acquire a new user name and password?

If you cannot remember your username, please write an email to (journals.researchers@gmail.com), who will locate your username and notify you. If you know your username, but cannot remember your password, please click the "Login" link on the left-hand menu at homepage. Below the fields for entering your username and password, you will notice a link that asks "Forgot your password?"; click that link and then enter your email adddress to reset your password. You will be sent an automated message with a temporary password and instructions for how to create a new password. TIP: If you do not receive the automated email in your inbox, please check your SPAM or Junk Mail folder. For any other issues, please contact our Managing Editor,Kamyar Bagherinejad (admin@journals-researchers.com).

How do I locate the online submission form and fill it out?

First you need to register or login (see above). Once you are logged in, make sure the "roles" section of your profile has "Author" selected. Once you assign yourself the role of "Author," save your profile and then click the "New Submission" link on your user home page.

Once you arrive at the submission form page, please read the instructions carefully filling out all necessary information. Unless specified otherwise by the editors, the journal section to be selected for your submission should be "Artlcles." Proceed to the remaining sections, checking all boxes of the submission preparation checklist, and checking the box in the copyright notice section (thus agreeing to journals-researchers's copyright terms). Once the first page is completed, click "Save and Continue." The next page allows you to upload your submission. Use the form to choose your file from your computer. Make sure you click "Upload." The page will refresh and you may then click "Save and Continue." You will then proceed to a page for entering the metadata for your article. Please fill out all required fields and any further information you can provide. Click "Save and Continue." The next page allows you to upload supplementary files (images, audiovisual materials, etc.). These are not required, but if you wish to provide supplementary materials, please upload them here (do no forget to click "Upload." Then click "Save and Continue." This brings you to the final page of the submission form. Please click "Finish Submission" in order to close the submission process. You wil then be notified by email that your article has been successfully submitted. TIP: If you do not receive the automated email in your inbox, please check your SPAM or Junk Mail folder. For any other issues, please contact our Managing Editor, Kamyar Bagherinejad (admin@journals-researchers.com).

Why am I not receiving any email notifications from HAU?

Unfortunately, some automated messages from Open Journal Systems arrive in users' Spam (or Junk Mail) folders. First, check those folders to see if the message was filtered into there. You may also change the settings of your email by editing your preferences to accept all mail from [jcer] and related journals-researchers.com email accounts.

I am trying to upload a revised article following an initial round of peer-review, but I cannot locate where to upload the article. Where do I submit a revised article?

Follow the login process outlined above and when you successfully login you will see on your user home page a link next to "Author" for "active" articles in our system (usually it is only one article, but if you have mulitple submissions currently in our system, the number could be higher. Click the "Active" link and you will be led to a page that lists your authored articles currently in our system. Click the link under the column labeled "Status" and this will take you to a page showing the current review status of your article. At the very bottom of the screen, you will see an upload form under the heading "Editor decision." Here you may upload your revised article. An automated email will be sent to the editors and you may also notify them directly via email. You may then logout.

I successfully submitted an article; how long will it take for the editors to respond to me with a decision.

For all articles that are recommended for peer-review, the editors of JCER strive to notify authors of a decision within 4-6 weeks. You may contact JCER's Managing Editor, Kamyar Bagherinejad (admin@journals-researchers.com). if you have any questions relating to the review process and its duration.

For all other inquiries, please contact: Kamyar Bagherinejad (Managing Editor)

Privacy Statement

The names and email addresses entered in this journal site will be used exclusively for the stated purposes of this journal and will not be made available for any other purpose or to any other party.

Articles

Section default policy

Make a new submission to the Articles section.

Copyright Notice EditEdit Copyright Notice

Journal of Civil Engineering Researchers follows the regulations of the International Committee on Publication Ethics (COPE) and the ethical principles of publishing articles in this journal are set based on the rules of this committee, and in case of problems, it will be treated according to these rules.

Privacy Statement EditEdit Privacy Statement

The names and email addresses entered in this journal site will be used exclusively for the stated purposes of this journal and will not be made available for any other purpose or to any other party.

Scholars Pavilion

Scholars Pavilion or **Scholars Chartagi** is a monument donated by the Islamic Republic of Iran to the United Nations Office at Vienna. The monument architecture is claimed by the Islamic Republic News Agency of Iran to be a combination of Islamic and Achaemenid architecture, although the latter clearly predominates in the decorative features, with Persian columns and other features from Persepolis and other remains from the Achaemenid dynasty. The Chahartaq pavilion form runs through the architecture of Persia from pre-Islamic times to the present.

Statues of four famous Persian medieval scholars, Omar Khayyam, Al-Biruni, Muhammad ibn Zakariya al-Razi and Ibn-Sina are inside the pavilion. This monument donated in June 2009 in occasion of Iran's peaceful developments in science.

J-Researchers